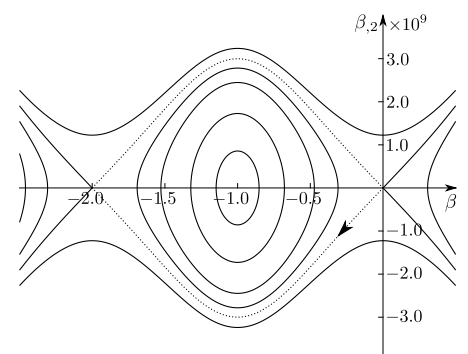
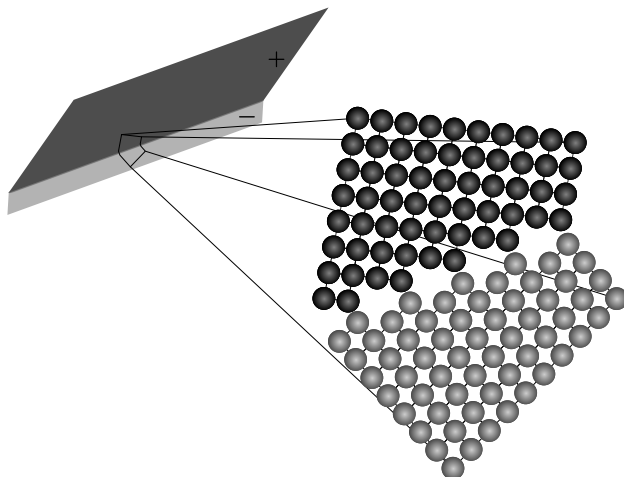
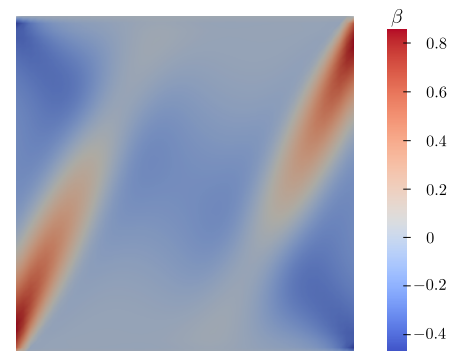
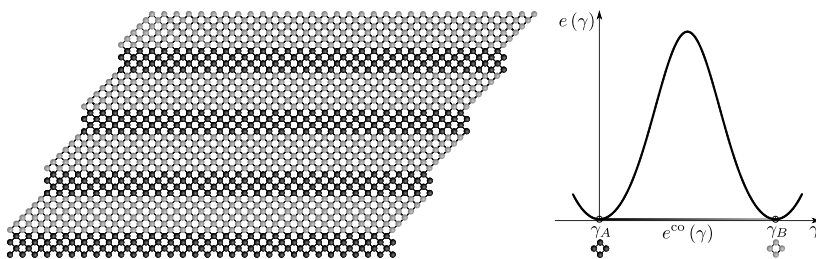


Modeling the Formation of Grain Boundaries using Nonlinear Continuum Dislocation Theory

Michael Koster



RUHR-UNIVERSITÄT BOCHUM

**Modeling the Formation of Grain Boundaries
using Nonlinear Continuum Dislocation Theory**

Dissertation

zur

Erlangung des Grades

Doktor-Ingenieur

der

Fakultät für Maschinenbau
der Ruhr-Universität Bochum

von

Michael Koster
aus Iserlohn

Bochum 2018

Herausgeber (Publisher):

Institut für Mechanik

— Schriftenreihe —

Ruhr-Universität Bochum

D-44780 Bochum

ISBN

This material is presented to ensure timely dissemination of scholarly and technical work. Copyright and all rights therein are retained by the copyright holders. All persons copying this information are expected to adhere to the terms and constraints invoked by the author's copyright. These works or parts of it may not be used to repost reprint/republish or for creating new collective works for resale or redistribution to servers or lists without the explicit permission of the copyright holder.

Dieses Werk ist urheberrechtlich geschützt. Die dadurch begründeten Rechte, insbesondere die der Übersetzung, des Nachdrucks, des Vortrags, der Entnahme von Abbildungen und Tabellen, der Funksendung, der Mikroverfilmung oder der Vervielfältigung auf anderen Wegen und der Speicherung in Datenverarbeitungsanlagen, bleiben, auch bei nur auszugsweiser Verwertung, vorbehalten. Eine Vervielfältigung dieses Werkes oder von Teilen dieses Werkes ist zulässig. Sie ist grundsätzlich vergütungspflichtig. Zuwiderhandlungen unterliegen den Strafbestimmungen des Urheberrechtsgesetzes.

©2018 Michael Koster, Institut für Mechanik, Ruhr-Universität Bochum

Printed in Germany

Einreichung der Dissertation (thesis submission): 12.06.2018

Tag der mündlichen Prüfung (thesis defense): 08.08.2018

Erster Referent (first referee):

Prof. Dr. rer. nat. Khanh Chau Le

Zweiter Referent (second referee):

Prof. Dr. rer. nat. Klaus Hackl

Vorsitzender (committee chair):

Prof. Dr.-Ing. Martin Mönnigmann

Acknowledgements

I would like to extend my sincere thanks to Professor Khanh Chau Le for his guidance as my advisor and as the first referee of the doctoral committee. I am grateful for sharing his extensive knowledge in the fields of mechanics and mathematics. His suggestions were the basis for most of the research pursued and presented in this thesis.

I also wish to thank Professor Klaus Hackl for accepting me as a research associate at the Institute of Mechanics of Materials, for his constructive advice and for being the second referee of the doctoral committee.

Many thanks to Professor Martin Mönnigmann for being the committee chair.

In addition, I very much appreciate the funding by German Research Foundation (DFG) in the framework of GPor-G ‘Kontinuumsversetzungstheorie bei massiver plastischer Umformung von Aluminium-Werkstoffen’ as part of SFB 692 ‘HALS’.

What is more, I enjoyed working at the Institute of Mechanics of Materials and would like to thank all my colleagues for the nice time. Special thanks to Dr.-Ing. Ulrich Hoppe for his support as well as to Dr.-Ing. Mehdi Goodarzi, Stephan Schwarz and Dr.-Ing. Johanna Waimann, whom I had great pleasure working with.

Finally, thanks also to my parents, Monika and Michael Koster, for their unwavering support and, of course, to my sister Dominique for cheering me up with her excellent sense of humor.

Summary

This thesis is concerned with modeling the formation of grain boundaries in ductile single crystals, using the framework of nonlinear continuum dislocation theory (CDT). It is assumed that the crystal sample under investigation is subject to large plastic deformations and contains a single active slip system. Different assumptions and strategies, based on nonconvex energy minimization, are used to mimic the formation of grain boundaries exhibiting various characteristics.

In a first approach grain boundaries are modeled as sharp interfaces via the mathematical concept of the singular surface, resulting in a laminate structure. In an enhanced model it is assumed that grain boundaries are objects of small but finite thickness constituting a transition zone between laminate layers. In addition to that, the formation of boundaries inclined at a prescribed angle is modeled accounting for dissipative effects. It is found that the results from this series of analytical and semi-analytical computations admit a clear physical interpretation.

What is more, a numerical investigation is performed on the basis of the finite element method. It turns out that there exists a relation between the choice of the slip system orientation and the resulting plastic slip.

Kurzfassung

Die vorliegende Arbeit beschäftigt sich mit der Modellierung der Korngrenzenbildung in duktilen Einkristallen im Rahmen der nichtlinearen Kontinuumsversetzungstheorie. Es wird angenommen, dass die zu untersuchende Kristallprobe großen plastischen Deformationen ausgesetzt wird und ein aktives Gleitsystem aufweist. Es werden verschiedene Annahmen und Strategien auf der Basis nichtkonvexer Energieminimierung verwendet, um die unterschiedlichen Charakteristiken der Korngrenzenbildung abzubilden.

In einem ersten Ansatz werden Korngrenzen als scharfe Grenzen mithilfe des mathematischen Konzepts der singulären Fläche als Laminatstruktur modelliert. In einem erweiterten Modell werden Korngrenzen als Übergangszonen endlicher, aber geringer Dicke angenommen. Außerdem werden dissipative Effekte berücksichtigt, die die Korngrenzenbildung unter einer vorgeschriebenen Orientierung ermöglichen. Es wird gezeigt, dass die verschiedenen analytischen und semi-analytischen Verfahren eine klare physikalische Interpretation zulassen.

Darüber hinaus wird eine numerische Untersuchung auf Basis der Finite-Elemente-Methode vorgestellt. Es zeigt sich, dass ein Zusammenhang zwischen der vorgegebenen Orientierung des Gleitsystems und der resultierenden plastischen Gleitung existiert.

Table of Contents

1	Introduction	1
2	Plastic Deformation of Single Crystals	5
2.1	Atomic Slip in Cubic Crystal Structures	5
2.2	Fundamental Dislocation Theory	7
2.3	Hardening of Single Crystals	13
2.4	Bicrystal Grain Boundaries	16
3	Essential Continuum Mechanics	19
3.1	Continuum Bodies and Motion	19
3.2	Measures of Deformation	21
3.3	Traction Forces and Stress	27
3.4	Elastic Material Response and Objectivity	29
3.5	Hyperelasticity and Strain-Energy	33
3.6	Static Equilibrium	34
3.7	Finite Elasto-Plastic Deformations	40
4	Modeling Microstructure using Nonlinear Continuum Dislocation Theory	43
4.1	Grain Boundaries as Sharp Interfaces	43
4.1.1	Foundations of Nonlinear Continuum Dislocation Theory	43
4.1.2	Equilibrium Conditions for Crystals with Grain Boundaries	47
4.1.3	Energy Formulation and Constitutive Equations	53
4.1.4	Plane-Strain Deformation and Laminate Construction	63
4.2	Grain Boundaries of Finite Thickness	73
4.2.1	Regularized Energy Functional	73
4.2.2	Enhanced Laminate Model	74
4.3	Inclined Grain Boundaries	81
4.3.1	Kinematics from Experimental Analysis	82
4.3.2	System Formulation and Solution Strategy	85
4.3.3	Inclined Laminate Structure	89
5	Numerical Investigation	99
5.1	Variational Formulation and Linearization	99
5.2	Finite Element Solution Procedure	101
5.3	Simple Shear Deformation	103
6	Final Remarks and Outlook	107
	References	109
	Curriculum Vitae	116

1 Introduction

It is well known that large macroscopic deformations of metals and alloys induce structural changes, involving various length scales. This gives rise to the structure–properties paradigm of materials science. An important example related to the coupling of a material’s structure and its features is the Hall–Petch relation, see e.g. Hansen (2004); Jiang and Weng (2004). It establishes a proportionality relation between a crystal’s yield strength and the grain size. This coupling makes evident that not only structures at the atomic scale are of relevance but also geometric structures of collections of atoms at the microstructural scale have an impact on the properties of metals. A comprehensive discussion of structure–property relations in crystals can be found in Phillips (2001). For this thesis the case of large plastic deformations of ductile single crystals and the resulting structural changes at the microscale are of particular interest, where the following motivation is based on the introductory part of Koster, Le and Nguyen (2015).

Real-world applications of the structure–properties paradigm can be found in the field of cold working in materials processing. There exists a large variety of cold forming processes involving severe plastic deformation, where examples of the characterization of microstructures resulting from large plastic deformations can be found in experimental studies using equal-channel angular pressing (ECAP), see Segal (1995); Valiev and Langdon (2006); Fukuda et al. (2003, 2006), and high pressure torsion, see Vorhauer and Pipan (2004); Sakai et al. (2005); Valiev et al. (2000). The accompanying changes of geometric structures observed at the microlevel comprise the formation of grain and subgrain boundaries, see Kuhlmann-Wilsdorf and Hansen (1991); Hughes and Hansen (1997), deformation twinning, see Tome et al. (1991); Christian and Mahajan (1995), and the formation of shear bands in polycrystals and single crystals, see Jia et al. (2003); Harren et al. (1988); Uchic et al. (2009), among others.

To describe the microstructure formation in ductile single crystals a vital ingredient is the consideration of dislocations as plastic slip of atomic layers is a key mechanism in the plastic deformation of crystals. Since the amount of dislocations involved is very large, where the typical number is 10^8 to 10^{15} per square meter, this thesis aims at modeling the formation of microstructure in a continuum setting. Specifically, the goal is to mimic the formation of boundaries in single crystals, interpreted as grain boundaries, due to large deformations. The basis is a hyperelastic energy formulation enhanced by a contribution accounting for the dislocation network. A point of departure is the concept of low energy dislocation structures (LEDS), see Hansen and Kuhlmann-Wilsdorf (1986), hypothesizing that the dislocation structures in the final deformation state minimize the crystal’s energy, see also Laird et al. (1986); Kuhlmann-Wilsdorf (1989). It turns out that another critical contribution to the theory is the nonconvexity of the energy function, see Ortiz and Repetto (1999); Ortiz et al. (2000), where the deformation of ductile crystals is analyzed in the framework of finite crystal plasticity, based on nonconvex energy minimization of the pseudoelastic energy densities of crystals exhibiting geometrical softening or latent hardening behavior. It is shown for the single slip case that an energy minimizing sequence can be obtained in the form of a laminate structure with piecewise constant plastic deformation and an elastic deformation corresponding to a pure rotation. An extension

providing a general single slip finite crystal plasticity theory can be found in Carstensen et al. (2002). Due to its phenomenological character crystal plasticity is concerned with plastic slip, but is lacking its source, i.e. it does not account for dislocations. To be able to mimic the behavior of real crystals additional phenomenological concepts like back stress or hardening have to be introduced into the model via internal variables. This leads to additional constitutive equations that can be obtained naturally in a more general CDT, see Berdichevsky and Le (2007); Le and Sembriring (2008a,b); Kochmann and Le (2008a,b, 2009); Kaluza and Le (2011); Le and Nguyen (2012, 2013).

Alternative approaches can be found in Lee et al. (2002); Lim et al. (2011); Engels et al. (2012); Öztö et al. (2013); Mayeur and McDowell (2014). Another concept is discussed in Zhu et al. (2013); Zhu and Xiang (2014), where a continuum representation of the dislocation density and the energy of grain boundaries, including the long-range elastic energy of nonequilibrium grain boundaries, are derived from a discrete dislocation dynamics model. This allows for capturing the details of the formation process of grain boundaries.

In Ortiz and Repetto (1999) the dislocation density is considered to justify heuristic estimates of the spacing of dislocation walls and a way to generalize concepts to the case of a CDT is proposed. An overview of the finite strain CDT literature can be found in Le and Günther (2014), where a nonlinear CDT is proposed, providing definitions of the resultant Burgers vector and the dislocation density tensor. Based on Kröner (1992) the elastic deformation and the dislocation density tensor are identified as the state variables of the theory. This theory forms the basis for the derivation of the full set of equilibrium equations and jump conditions arising in single crystals forming grain boundaries due to large plastic deformations, given in Koster, Le and Nguyen (2015). An extension to the theory can be found in Koster and Le (2015), providing a procedure to determine grain boundaries of small but finite thickness, based on the regularization of the nonconvex energy, introducing a gradient term.

The outline of this thesis is given in what follows. The subsequent Chapter 2 deals with the materials science perspective of the plastic deformation of single crystals. Cubic crystal systems and the fundamentals of dislocation theory are treated first. After that, hardening mechanisms and bicrystal grain boundaries are introduced briefly.

In Chapter 3 fundamentals from continuum mechanics are reviewed. The point of departure is the definition of a continuum body and the associated concept of motion. Next, various measures of deformation are discussed thoroughly as the relations are important to the investigations presented later. Then, some definitions of stress are given. In what follows, a general formulation of elastic material response and the notion of objectivity are presented. The concept of material frame indifference obviously is not immediately applied in the computations that follow, but is still considered important as there is a discussion of notions of convexity at a later point in the thesis, where the topic is of interest. After that, hyperelasticity and strain-energy functions are considered. The next topic treated is static equilibrium, which is introduced via the calculus of variations. This is the first time in this thesis when the reader encounters a special Section, the title of which starts with ‘Extra’ and its end is indicated by a \triangle symbol. Sections of this type can be found several times throughout the thesis and are intended to give some background information on nonstandard topics related to continuum mechanics, of interest for the analyses to follow. Eventually, an interpretation of the kinematics of large elasto-plastic deformations is given.

The following Chapter 4 deals with different approaches to modeling the formation of grain boundaries in ductile single crystals using nonlinear CDT. After an outline of the theory and a derivation of the corresponding set of equilibrium equations and jump conditions grain boundaries are modeled as sharp interfaces via the mathematical concept of the singular surface. Then, an enhanced model is provided, introducing grain boundaries of small but finite thickness. Finally, the theory is extended in another way, where the formation of inclined grain boundaries is discussed, based on experimental observations. The last model makes use of a dissipative term accounting for the hardening of the single crystal sample under investigation. After discussing the assumptions regarding the kinematics of inclined grain boundaries the mathematical formulation of the problem and the solution procedure are presented. Finally, the resulting laminate structure is examined in detail.

In the subsequent Chapter 5 the numerical solution, based on the energetic formulation in Chapter 4, is discussed in the framework of the finite element method. First, the variational statement and the corresponding linearization of the problem are outlined as the starting point for the solution procedure. Next, the discretized version of the problem is stated. Ultimately, the results pertaining to the case of a simple shear deformation are discussed.

The final Chapter 6 provides some concluding remarks. In addition to that, an extension to the investigations performed is proposed.

2 Plastic Deformation of Single Crystals

The framework of nonlinear CDT aims at providing a continuum theory that can capture mechanisms underlying the plastic deformation of single crystals, based on observations from metal physics. Thus, information from both fields has to be combined in order to establish an appropriate theory. To start with, the current Chapter provides some of the fundamental notions from crystallography and materials science needed. What is more, Sections 2.3 and 2.4 serve as a motivation for the analysis of the problems to be discussed in Chapters 4 and 5. It has to be pointed out that this Chapter is not meant to provide a comprehensive treatment of the area of materials science and therefore does not cover all of the details of the topics touched to a full account. Rather, the emphasis is on the presentation of the basics, necessary to be able to grasp the definitions and assumptions of nonlinear CDT, outlined in Subsection 4.1.1.

2.1 Atomic Slip in Cubic Crystal Structures

The basis for studying the processes at the atomic scale giving rise to the plastic deformation of single crystals is the definition of an ideal crystal and the relevant crystallographic structures. What is of interest for the studies to follow is the cubic crystal system.

An ideal crystal is to be understood as an infinite structure, where atoms or collections of atoms, referred to as the basis, are repeated periodically on prescribed lattice sites in space. The lattice is also termed the Bravais lattice and the corresponding points of the lattice are called Bravais sites. This can be expressed as

$$\text{crystal} = \text{lattice} + \text{basis},$$

where the lattice must exhibit translational symmetry, i.e. the relative arrangement and orientation of all points in the lattice must be the same, see e.g. Bulatov and Cai (2006); Tadmor and Miller (2011). The mathematical description of a Bravais lattice is given in terms of linearly independent lattice vectors that define a primitive cell, which is repeated regularly. The position of any lattice site then can be expressed in terms of a linear combination of its lattice vectors, given by

$$\mathbf{R} = n_1 \mathbf{e}_1 + n_2 \mathbf{e}_2 + n_3 \mathbf{e}_3,$$

where the n_i are integer values and the lattice vectors \mathbf{e}_i define a parallelepiped. The smallest associated parallelepiped with its edges defined by the lattice vectors and having a lattice site at its eight vertices is called the primitive cell. In the case of the cubic crystal system the Bravais lattice is given in terms of the orthogonal lattice vectors \mathbf{a} , \mathbf{b} and \mathbf{c} of the same length, specifying the so-called unit cell. There exist three different cubic lattices, denoted the simple-cubic (SC), body-centered-cubic (BCC) and the face-centered-cubic (FCC) lattice, respectively. For the SC lattice the Bravais sites are given as

$$\mathbf{R} = i\mathbf{a} + j\mathbf{b} + k\mathbf{c}, \tag{2.1}$$

with integer valued i, j, k and $|\mathbf{a}| = |\mathbf{b}| = |\mathbf{c}|$. For the BCC lattice the lattice points can be described via

$$\begin{aligned}\mathbf{R} &= i\mathbf{a} + j\mathbf{b} + k\mathbf{c}, \\ \mathbf{R} &= \left(i + \frac{1}{2}\right)\mathbf{a} + \left(j + \frac{1}{2}\right)\mathbf{b} + \left(k + \frac{1}{2}\right)\mathbf{c}\end{aligned}\tag{2.2}$$

and the FCC lattice sites are defined by

$$\begin{aligned}\mathbf{R} &= i\mathbf{a} + j\mathbf{b} + k\mathbf{c}, \\ \mathbf{R} &= \left(i + \frac{1}{2}\right)\mathbf{a} + \left(j + \frac{1}{2}\right)\mathbf{b} + k\mathbf{c}, \\ \mathbf{R} &= \left(i + \frac{1}{2}\right)\mathbf{a} + j\mathbf{b} + \left(k + \frac{1}{2}\right)\mathbf{c}, \\ \mathbf{R} &= i\mathbf{a} + \left(j + \frac{1}{2}\right)\mathbf{b} + \left(k + \frac{1}{2}\right)\mathbf{c}.\end{aligned}\tag{2.3}$$

It can be seen from the below Figure 2.1 that for (2.1) the unit cell coincides with the primitive cell and for (2.2) and (2.3) the unit cells are larger than the corresponding primitive cells, where the black dots indicate the Bravais sites of the respective lattice. To eventually obtain the crystal

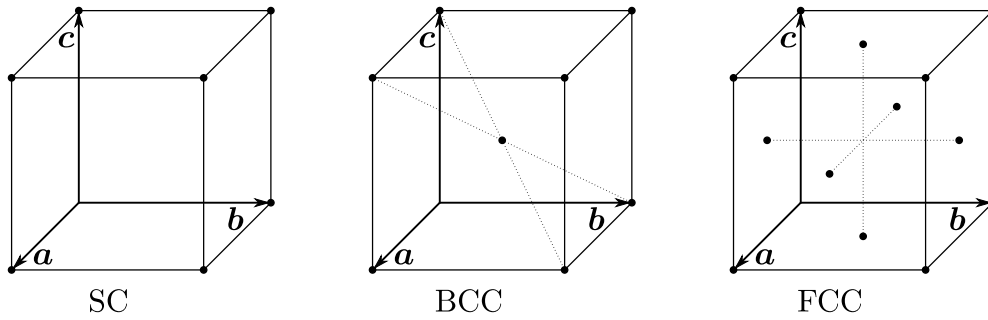


Figure 2.1: Unit cells of the three cubic crystal systems, adapted from Bulatov and Cai (2006).

structures associated with the aforementioned lattices, an appropriate basis has to be introduced, attaching atoms to the Bravais sites.

To identify the direction of lines and the orientation of planes in terms of a unit cell, the so-called Miller index notation is employed, frequently, see e.g. Bulatov and Cai (2006); Hull and Bacon (2011); Phillips (2001); Tadmor and Miller (2011). Here, the discussion is limited to the case of cubic crystals. Any direction

$$\mathbf{k} = i\mathbf{a} + j\mathbf{b} + k\mathbf{c},$$

with arbitrary integers i, j and k can be described by a vector parallel to \mathbf{k} and passing through the origin of the unit cell. It is given by the three smallest integer values obtained from the ratios of the components of the vector to the lengths of the respective edges of the unit cell. Thus, using Miller index notation, the direction given by vector $\mathbf{l} = a\mathbf{a} + a\mathbf{b} + a\mathbf{c}$ can be expressed as

$$\left[\begin{smallmatrix} a & a & a \\ a & a & a \end{smallmatrix}\right] = [1\ 1\ 1],\tag{2.4}$$

where square brackets are used to designate a single direction. The use of an overline denotes a negative value, as in

$$\left[\begin{array}{ccc} a & a & -a \\ a & a & a \end{array} \right] = [1 \ 1 \ \bar{1}], \quad (2.5)$$

representing the vector $\mathbf{m} = a\mathbf{a} + a\mathbf{b} - a\mathbf{c}$. An illustration of (2.4) and (2.5) in terms of an SC unit cell is given in the below Figure 2.2. What is more, there exists a notation for families of

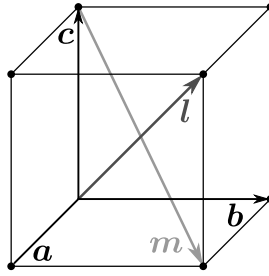


Figure 2.2: Definition of crystal directions \mathbf{l} and \mathbf{m} with respect to an SC unit cell, adapted from Hull and Bacon (2011).

directions, where $\langle 1 \ 1 \ 1 \rangle$ denotes the collection

$$[1 \ 1 \ \bar{1}], \quad [\bar{1} \ 1 \ 1], \quad [\bar{1} \ \bar{1} \ 1], \quad [\bar{1} \ \bar{1} \ \bar{1}].$$

To describe the orientation of planes, the Miller indices are defined as the reciprocals of the ratios of the plane's intercepts with the principal axes of the unit cell to the lengths of the unit cell's edges. The resulting values are typically reduced to the three smallest integers. If there is no intercept with one or two of the axes, the corresponding ratio is of the form $\frac{a}{\infty}$, which is interpreted as the limit value of 0. For example, the plane having intercepts of $2a$, $3a$ and $3a$ with the x , y and z -axis, respectively, shown in Figure 2.3, can be described by

$$\left(\frac{a}{2a} \ \frac{a}{3a} \ \frac{a}{3a} \right) = (3 \ 2 \ 2),$$

where parentheses are used to identify single planes. Again, the overline notation is applied for negative values and curly brackets are introduced to denote a collection of planes of the same crystallographic type, as in $\{1 \ 1 \ 1\}$.

Having defined the model of the ideal crystal along with the Miller index notation, the tools needed to describe the geometry of cubic crystals are at hand for subsequent use.

2.2 Fundamental Dislocation Theory

Another important ingredient for the study of the plastic deformation of single crystals is the concept of the dislocation, to be introduced in this Section. The notion of the dislocation arose from attempts to determine the strength of single crystals, where it turned out that the theoretical estimations were several orders of magnitude larger than the magnitude of the strength determined in experiments, see e.g. Phillips (2001); Khan and Huang (1995); Weertman and Weertman (1992). The reason for this discrepancy was found in crystallographic defects, i.e.

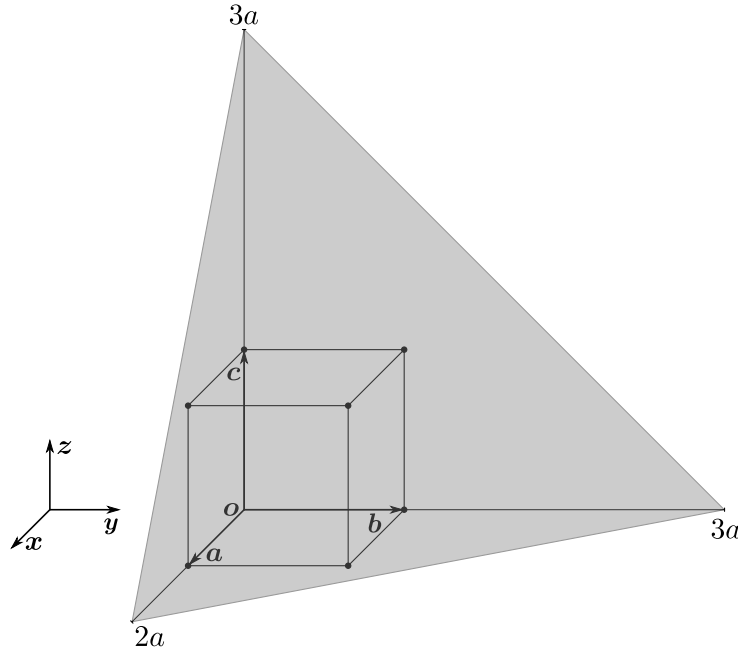


Figure 2.3: Definition of the plane (3 2 2) with respect to an SC unit cell, adapted from Hull and Bacon (2011).

deviations from the model of the ideal crystal, observed in real crystals. It was in 1934, when findings of paramount importance for the explanation of the mechanisms of plastic deformation of single crystals were published, see Taylor (1934); Orowan (1934); Polanyi (1934). The three independent studies suggested that there existed objects, denoted dislocations, assisting plastic deformation in real crystals. Actually, it was not before the late 1950s, when there was experimental evidence of dislocations, observed using transmission electron microscopy (TEM), see e.g. Bulatov and Cai (2006). A more detailed account of the historical events can be found in Hirth (1985) and the references therein. It was found that dislocations are the key to a large variety of material properties of interest for engineering applications, where this thesis is exclusively concerned with the mechanical features. What is at the focus of the investigations to follow is the dislocations' role in the plastic deformation of crystals, i.e. the investigation of plastic slip of atomic layers in single crystals due to the presence of dislocations.

There exist various types of defects in real crystals, which can be interpreted as interruptions of the regular pattern defined by the ideal crystal model. These defects are categorized in groups, specifying their spatial range, see e.g. Phillips (2001). If only single atoms at discrete lattice sites are affected, the defect is termed a point defect. This comprises empty lattice sites, where atoms are missing and positions in the crystal lattice, where atoms have been replaced by atoms of a different species than those typically present in the crystal. If arrays of neighboring atoms are affected, as in the case of dislocations, this is called a line defect. It is shown below, in which way the lattice is affected by dislocations, where the presentation is based on the ideas in Bulatov and Cai (2006). In addition to that, there exist so-called wall defects, where the notion of the bicrystal grain boundary is of interest, briefly discussed in Subsection 2.4.

To get an idea of how dislocations can be identified in a crystal lattice, there exist thought experiments illuminating the creation of dislocations. The typical procedure starts with an ideal SC crystal structure, as shown in Figure 2.4, where the lines connecting atoms indicate bonds

of some physical kind, the nature of which is not specified any further. Assuming there exists a

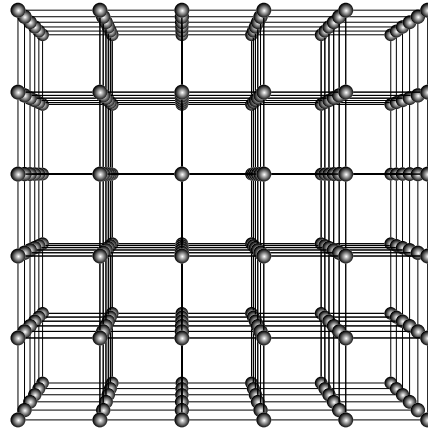


Figure 2.4: Arrangement of atoms in an ideal SC crystal, adapted from Bulatov and Cai (2006).

way to remove some of these bonds, a cut plane is introduced. Then, a cut operation is applied to remove the connections at the centers of the three columns of atoms on the left side of the crystal in Figure 2.4. The edge of the plane residing inside the crystal, defining the end of the cut is called the dislocation line. After that, the arrays of atoms above the plane are shifted via atomic slip by one atomic position to the right, corresponding to the lattice vector \mathbf{b} . Next, the two leftmost columns of atoms of the crystal's top part are rejoined to the columns below them, creating an edge on the lower left portion of the crystal and distorting the lattice. The resulting structure, shown in Figure 2.5, is the outcome of creating a so-called edge dislocation in the crystal. Inspection of the altered crystal structure reveals that the procedure outlined

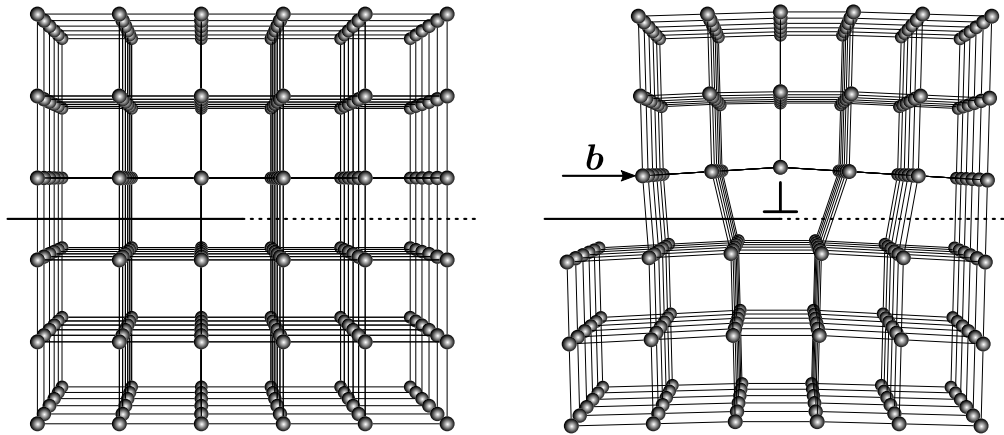


Figure 2.5: Creation of an edge dislocation from an initially perfect SC crystal applying a cut-and-slip operation, adapted from Bulatov and Cai (2006).

before has a similar effect as inserting an additional half-plane of atoms in the top part of the crystal, which is usually indicated by the symbol \perp , as depicted in Figure 2.5, marking the dislocation line, running perpendicular to the plane of the sketch. The orientation of the vertical bar of the tag \perp represents the sign of the associated dislocation, where insertion of the extra array of atoms from above corresponds to a positive orientation and insertion from below implies a negative sign. Actually, there exist many different ways to figure the creation

of a dislocation in theoretical experiments. The same is true for real dislocations, where in what follows large plastic deformations, leading to shearing of atomic layers, is assumed the main driver for producing dislocations. The only thing that can be identified inside a crystal is the existence of a dislocation, the way it was created cannot be traced.

Apart from edge dislocations, which are at the heart of the analyses to follow in subsequent Chapters, there exists another basic type of dislocations, termed screw dislocations. Its creation follows the same cut procedure as explained above, which is followed by a different way of displacing the upper part of the crystal with respect to its lower portion. Here, the slip of atom layers is assumed in the direction parallel to the dislocation line, again by one atomic distance, illustrated by vector \mathbf{b} in Figure 2.6.

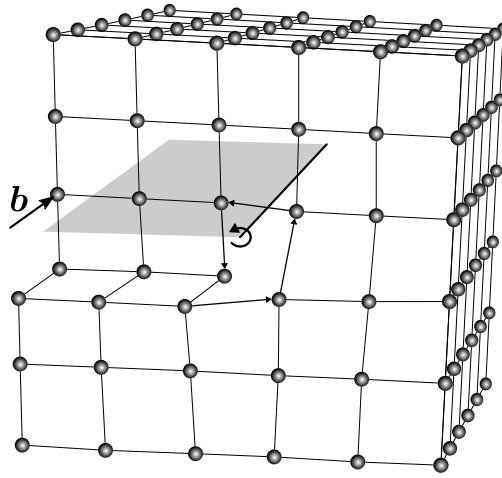


Figure 2.6: Creation of a screw dislocation from an initially perfect SC crystal applying a cut-and-slip operation, adapted from Bulatov and Cai (2006).

In the examples presented above dislocation lines are assumed to be straight, which is presumed throughout this thesis. Actually, the two types of dislocations introduced before form the basis of what is called mixed dislocations, where dislocation lines are curved, depicted in Figure 2.7, combining features of both kinds of dislocations. The character angle, defined as the angle between the dislocation line and the slip vector \mathbf{b} , characterizes the dislocation. An angle of 90° indicates a pure edge dislocation, whereas a 0° angle corresponds to a pure screw dislocation. Hence, angles between 0° and 90° are associated with mixed dislocations.

In real crystals dislocations may form complex structures comprised of a large number of single curved and irregularly shaped dislocation lines. These dislocations produce some distortion of the crystal lattice and can be observed and quantified using various experimental techniques, such as TEM and electron backscatter diffraction (EBSD). From a theoretical point of view, a means to measure the impact of a dislocation on the crystal lattice is the Burgers circuit test. To get a grasp of the procedure, assume an SC crystal lattice in the plane, containing an edge dislocation, as depicted in Figure 2.8. The method goes as follows: define a starting atom in the lattice and an orientation ξ of the dislocation line, indicating the sense of the circuit to draw. Then, starting at the atom chosen before, sketch a closed contour, consisting of single primitive vector steps, enclosing the dislocation. Choosing the same number of discrete steps in the northbound and southbound directions, as well as the identical number of steps in the horizontal orientations, it turns out that the starting position in the lattice does not coincide with the end

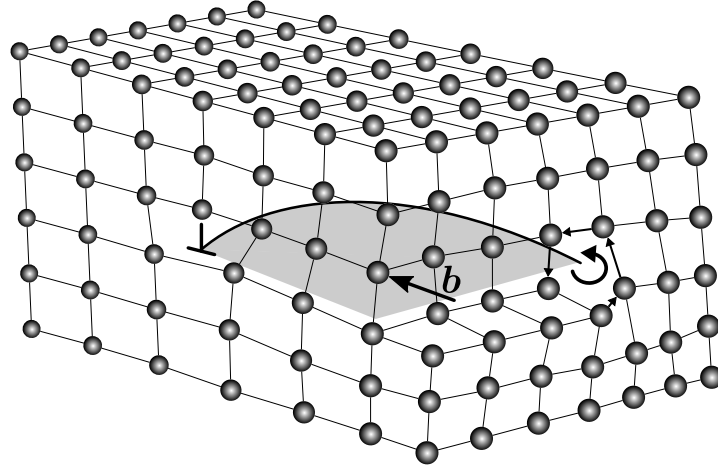


Figure 2.7: Mixed dislocation with a curved dislocation line arising from edge and screw contributions, adapted from Bulatov and Cai (2006).

point of the circuit, see e.g. Phillips (2001). There will be one horizontal primitive vector step left. This vector, pointing from the starting atom to the final atom in the circuit, is the so-called Burgers vector, measuring the topological misfit in the lattice. Choosing the opposite direction for the Burgers circuit yields a Burgers vector of the same magnitude with opposite sign. It can

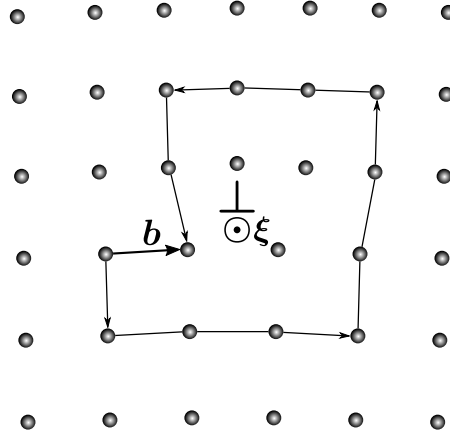


Figure 2.8: Burgers circuit applied to a single edge dislocation, adapted from Bulatov and Cai (2006).

be found that the procedure outlined before also works for circuits containing more than one dislocation. In addition to that, the Burgers vector is independent of the Burgers circuit chosen, as long as the path does not cut the dislocation line. Hence, the Burgers vector is conserved for a translation of the circuit along a dislocation line. Therefore, a dislocation cannot end at some point inside an otherwise ideal crystal structure, as this would cause a sudden drop in magnitude of the Burgers vector to zero. The principle of the conservation of the Burgers vector still holds in situations where several curved dislocation lines meet at some node and are merged into a single line. Then, the Burgers circuits enclosing the original lines and the single dislocation line, respectively, yield the same Burgers vector. By definition, it is assumed that all dislocation

lines flow out of the node of intersection, justifying the conservation condition

$$\sum_{i=1}^n \mathbf{b}_i = \mathbf{0}.$$

The classical continuum representation of the Burgers vector of a Volterra dislocation in the small deformation setting is given by

$$\mathbf{b} = \oint_{\mathcal{C}} \frac{\partial \mathbf{u}}{\partial l} dl,$$

i.e. the integration of the elastic displacement gradient $\partial \mathbf{u} / \partial l$ is performed around the curve \mathcal{C} , enclosing the dislocation line, giving the jump in the displacement, see e.g. Bulatov and Cai (2006); Phillips (2001). There exist different continuum interpretations of the Burgers vector. An appropriate definition, to be used in the framework of nonlinear CDT, is introduced in Subsection 4.1.1.

Another point of interest to be discussed next is the motion of dislocations, as it gives rise to the plastic deformation of crystals. A basic model of dislocation motion may be obtained from exposing the top surface of an ideal SC crystal sample of dimensions $L_x \times L_y \times L_z$ to a traction force T_y , while fixing the crystal's bottom surface. As illustrated in Figure 2.9, this external loading, corresponding to the shear stress

$$\sigma_{yz} = \frac{T_y}{L_x L_y}, \quad (2.6)$$

creates an edge dislocation with positive orientation ξ in the direction of the positive x -axis, moving through the crystal and eventually leaving the specimen at its right surface. The resulting structure is a crystal with its upper half displaced by one atomic distance, given as the magnitude of the Burgers vector $|\mathbf{b}| = | [0 \ b_y \ 0] |$, with respect to its lower half. Then, the work done by the traction force T_y is given by

$$W = b_y T_y. \quad (2.7)$$

Introducing a driving force per unit length f_y , acting on the dislocation, a reinterpretation of (2.7) can be given as

$$W = L_y f_y L_x,$$

where L_x is the length of the dislocation line and L_y is the distance by what the dislocation is moved through the crystal. Then, using (2.6), the driving force may be expressed as

$$f_y = \frac{W}{L_x L_y} = b_y \sigma_{yz}. \quad (2.8)$$

In the general case the product in (2.8) can be formulated using the so-called Peach-Koehler (PK) formula

$$\mathbf{f} = (\boldsymbol{\sigma} \mathbf{b}) \times \boldsymbol{\xi}, \quad (2.9)$$

related to the local stress field around an arbitrary dislocation, where the driving force is independent of the source of the stress. From (2.9) it can be seen immediately that the driving force is always perpendicular to the dislocation line. What is more, the local nature of the associated

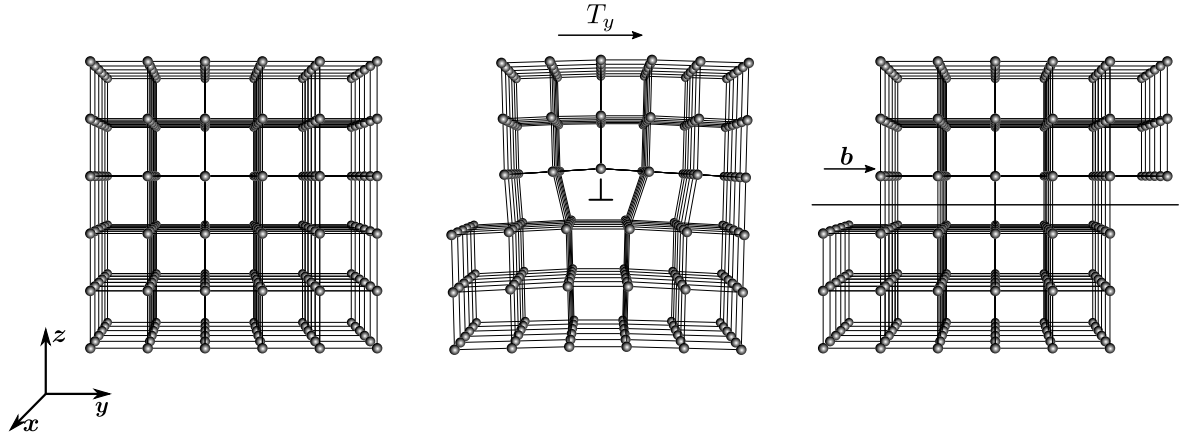


Figure 2.9: Net result of an edge dislocation induced by external shear, traversing an SC crystal from left to right, adapted from Bulatov and Cai (2006).

stress gives insight of vital importance into the plastic deformation of crystals. It turns out that significantly less rearrangement of atoms is involved in the motion of a dislocation compared with the relative displacement of two adjacent atomic layers, as was assumed in the computations of the theoretical strength of crystals, discussed at the beginning of this Subsection, see e.g. Bulatov and Cai (2006); Phillips (2001).

In addition to the above findings it has to be noted that there exist different modes of dislocation motion. What has been considered so far, is the motion of an edge dislocation, where the dislocation line successively occupies adjacent lattice sites along its glide plane in the direction of its Burgers vector. Since this kind of dislocation glide does not alter the amount of atoms in the crystal, it is termed conservative. Another situation is the motion of an edge dislocation perpendicular to its glide plane. This type of motion is called dislocation climb. In contrast to the first case it requires the insertion of additional rows of atoms and therefore is nonconservative.

The motion of screw dislocations is special, as they do not exhibit a unique glide plane. Screw dislocations always move in glide and the motion is conservative. For mixed dislocations the edge contribution of the Burgers vector governs the climb behavior. The motion of dislocations in real crystals usually is a combination of glide and climb. In certain situations one type of motion may be dominant, where at low temperatures mainly edge dislocations move on certain glide planes.

As mentioned before, the choice of topics discussed here is just a brief summary of subjects of importance in this thesis. For a more comprehensive discussion, including stress fields associated with dislocations and interactions of dislocations with other types of lattice defects see e.g. Hirth and Lothe (1982); Hull and Bacon (2011); Phillips (2001); Weertman and Weertman (1992) and the references therein.

2.3 Hardening of Single Crystals

Next, the focus is on the identification of specific planes and directions related to the hardening behavior of single crystals. It was found in experiments that plastic deformation of crystals is

assisted by slip of atomic layers that occurs on certain planes and in certain directions, denoted slip planes and slip directions, respectively, see e.g. Khan and Huang (1995); Phillips (2001). There is experimental evidence that slip always happens on closest-packed atomic planes and in directions, where atoms have the shortest distance. In FCC crystals this is true for the family of $\{111\}$ planes and in the $\langle 110 \rangle$ directions. In contrast, atomic slip in BCC crystals can be found on planes of $\{110\}$, $\{112\}$ or $\{123\}$ type and in directions of the family $\langle 111 \rangle$.

So far, the basics of crystallography related to the simplest cubic crystal systems and elementary models of edge and screw dislocations have been presented in the preceding Subsections 2.1 and 2.2. This provides the basis for the introduction of single crystal plasticity to be discussed in what follows. As outlined before, there exist simple models of dislocation motion in certain directions on particular slip planes. Such combinations of directions and planes are called slip systems, given by a unit normal to the slip plane, denoted \mathbf{n} , and the direction of slip, defined in terms of the Burgers vector as $\mathbf{s} = \mathbf{b}/b$. Depending on the type of crystal system under investigation different slip systems are available for a material to accommodate plastic deformation. The current discussion is restricted to the FCC crystal structure, which can be found in aluminum, of interest in the analyses to follow. A means to illustrate the slip systems of relevance in FCC crystals is the so-called Thompson tetrahedron, see e.g. Argon (2008); Hirth and Lothe (1982); Hull and Bacon (2011); Kubin (2013), where all of the four faces of the tetrahedron correspond to a slip plane of the $\{111\}$ family and the edges of the planes indicate the possible slip directions of type $\langle 110 \rangle$, shown in Figure 2.10. The associated Burgers vectors are given by $\mathbf{b} = a/2 \langle 110 \rangle$. Thus, the FCC crystal structure exhibits twelve distinct slip systems, where the planes and directions are those of closest packing. An important concept revealing the na-

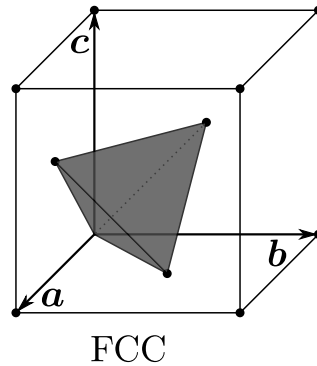


Figure 2.10: Thompson tetrahedron comprising one eighth of an FCC unit cell, adapted from Argon (2008).

ture of the plastic deformation of real crystals is the so-called resolved shear stress, based on tension and compression experiments on single crystal samples. The schematic setup of a tension experiment is shown in Figure 2.11, assuming a single active slip system. The slip system is indicated by vectors \mathbf{s} and \mathbf{n} . What is of particular importance is the orientation of the slip system with respect to the loading axis, given by the angles between vectors \mathbf{s} and \mathbf{n} and the vertical axis, denoted λ and ϕ , respectively. It has been found that plastic slip occurs when the resolved shear stress

$$\tau_r = \mathbf{s} \cdot \boldsymbol{\sigma} \mathbf{n} = \sigma_0 \cos \phi \cos \lambda \quad (2.10)$$

exceeds a certain threshold value, referred to as the critical shear stress τ_c , hence corresponding to the activation of the associated slip system. The resolved shear stress given in (2.10) can

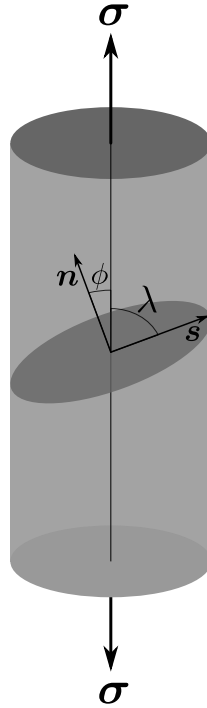


Figure 2.11: Setting of a tension experiment on a single crystal sample with slip system definition, adapted from Khan and Huang (1995).

be interpreted as the projection of the traction vector to the slip plane onto the slip direction s , with σ_0 the magnitude of the load. The product of the cosine functions $\cos \phi \cos \lambda$ is termed the Schmid factor. It is used in experimental studies to predict the activation of slip systems, see e.g. Fukuda et al. (2003).

The hardening of single crystals due to plastic deformation is closely related to the Schmid law (2.10), see e.g. Khan and Huang (1995); Kubin (2013); Phillips (2001). It has been found in experiments that there exist different stages of deformation, exhibiting some characteristic features associated with an increase of dislocations and rotations of the crystal lattice. These rotations can be explained best in a setting of tension or compression experiments, see e.g. Khan and Huang (1995); Kubin (2013). Assuming a single active slip system in a single crystal sample in tension it can be found that plastic slip must be accompanied by a rotation of the crystal lattice to maintain the vertical orientation of the loading axis, passing through the center of the slip plane at all times. The same is true for the case of compression. In addition to that, there is evidence that hardening is the result of self-hardening on active slip systems due to an elevation in the dislocation density, which in turn triggers latent hardening on nonactive slip systems. The interaction of these mechanisms results in the activation of additional slip systems and an orientation-dependent evolution of the shear stress as a function of shear strain.

Experimental studies revealed that distinct deformation stages can be identified in copper single crystals subject to tensile loading at room temperature, see Diehl (1956); Takeuchi (1975). It has been observed that there exist up to three separate regions in the shear stress–shear strain diagram of the samples, depending on the initial orientation of the loading axis. A plot of a generic stress–strain curve, exhibiting all three deformation stages found in FCC crystals, is shown in Figure 2.12. The following interpretation of the deformation behavior in the three portions of the stress–strain curve can be found in Argon (2008). Here, the first portion of the

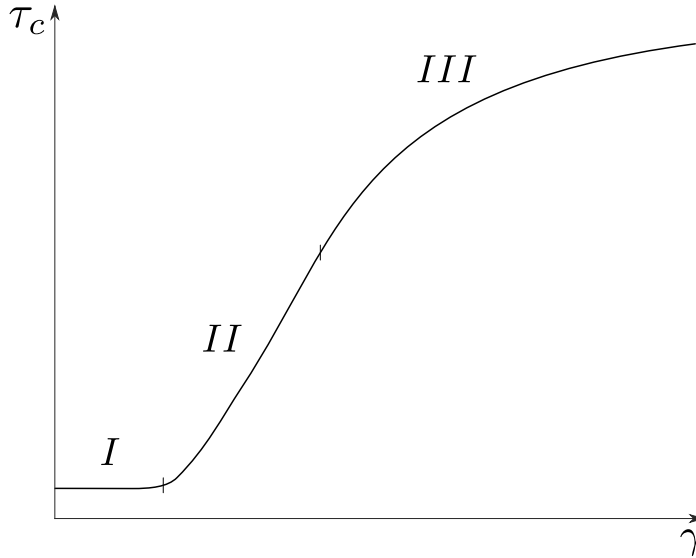


Figure 2.12: Critical shear stress–shear strain plot indicating the three-stage deformation found in FCC single crystals, adapted from Khan and Huang (1995).

curve, termed Stage *I*, easy glide or laminar slip region corresponds to a deformation mode involving just a single slip system with typical reduced strain-hardening rates $(d\tau/d\gamma)/\mu$ of 2×10^{-4} to 5×10^{-4} , where μ denotes the second Lamé parameter. After this low-stress deformation with very small hardening, the Stage *II* region clearly exhibits linear hardening behavior with reduced strain-hardening rates of the order of 10^{-2} . These deformation features arise from the formation of obstacles due to the activation of intersecting slip systems. Eventually, the reduced strain-hardening rate decreases and the resolved shear stress corresponds to a parabolic function of the shear strain when entering the Stage *III* deformation part of the plot. This kind of deformation behavior turns out to be temperature-dependent and can be observed at higher strains and lower temperatures.

It must be noted that the features outlined above just represent the very basics of the nature of plastic deformation and hardening of single crystals. The behavior of real crystals is very complex and depends on many different conditions. What is more, the three stages discussed before may be more or less pronounced or can be extended by additional ones, depending on the material and situation. A detailed discussion of the topic is beyond the scope of this thesis. For a comprehensive account of strengthening in crystals due to plastic deformation see e.g. Argon (2008); Kubin (2013) and the references therein.

2.4 Bicrystal Grain Boundaries

As the investigations of Chapter 4 are concerned with the construction of laminate structures, the last topic to be discussed in the current Chapter is the formation of grain boundaries. Here, a natural way to think of a boundary between adjacent layers of a 1st-order laminate is as a grain boundary forming between two portions of the crystal lattice that have undergone different deformations and thus may be identified as distinct grains. Such a boundary is termed a bicrystal grain boundary, the most important properties of which are discussed below.

In the current discussion, the simplest geometry of a bicrystal grain boundary forming in an SC crystal structure is considered, where the two grains are assumed to differ only by a lattice rotation and the boundary corresponds to a plane of a certain orientation, see Phillips (2001). Thus, the perfect Bravais lattice structure given by (2.1) is assumed for both crystals. Then, the three lattice vectors of one grain are denoted $e_i^{(1)}$ and the lattice vectors of the other grain are labeled $e_i^{(2)}$, as defined in Subsection 2.1. By definition, there must exist a relation of the form

$$e_i^{(2)} = Q e_i^{(1)},$$

where Q is a rotation matrix, the mathematical properties of which are discussed in detail in Section 3.2. What is important here is that the second grain is rotated with respect to the first one. Also, there may be situations, where a shift of the origin of coordinates has to be taken into account, introducing a rigid-body translation vector. Another vital ingredient to define a bicrystal grain boundary in geometrical terms is the orientation of the actual boundary between the two grains. The idea is to find a plane that separates the atoms of the two crystals. Depending on the orientation of the rotation axis related to matrix Q , there exist two types of grain boundaries. If the rotation axis is contained in the boundary plane, this is called a tilt boundary, illustrated in Figure 2.13 for two general grains. The boundary plane with the associated rotation vector is shown on the right. A rotation about an axis perpendicular to the

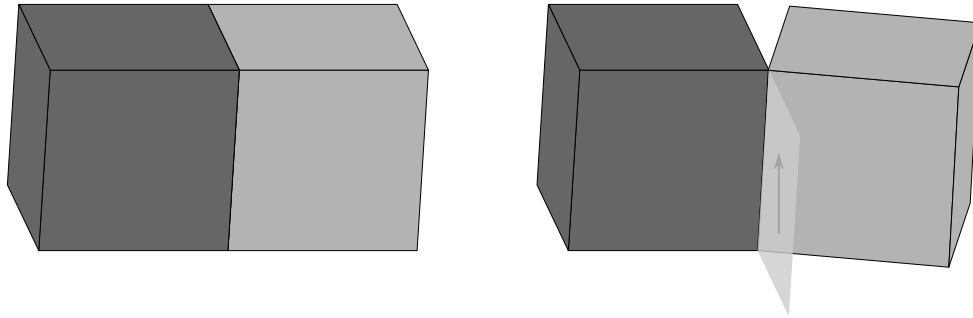


Figure 2.13: Geometry of a generic tilt grain boundary.

plane creates a twist boundary, shown in Figure 2.14. What is more, the magnitude of the

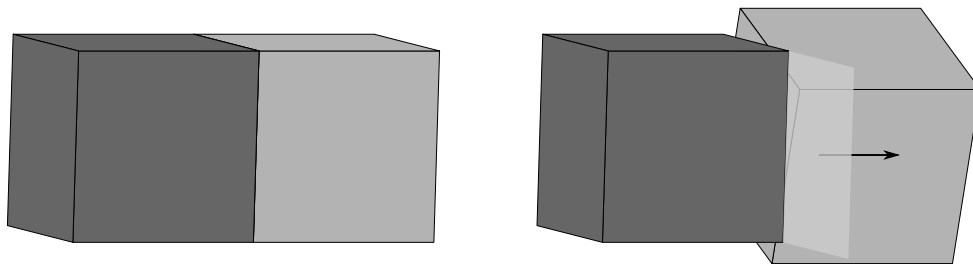


Figure 2.14: Geometry of a generic twist grain boundary.

relative rotation is an additional criterion in the characterization of grain boundaries. The angle defining this rotation is termed the angle of misorientation. For misorientation angles of up to 5° one speaks of a low-angle grain boundary, boundaries with a misorientation exceeding 10° are termed large-angle grain boundaries, see e.g. Hull and Bacon (2011). As in the case of dislocations, in real crystal mixed boundaries are encountered, having contributions of both types.

In some situations bicrystal grain boundaries exhibit a high degree of symmetry and it may be found that in the resulting structure there exist Bravais sites that are shared by both lattices. This is called a coincident site lattice (CSL) and can be quantified using the so-called Σ number, computed as the reciprocal value of the fraction of sites of a given lattice overlapping with the other lattice's positions.

3 Essential Continuum Mechanics

This Chapter deals with the second corner stone of nonlinear CDT, i.e. the basics of continuum mechanics and mathematics. The focus is on providing the concepts and definitions in as much detail as needed to follow the derivations and computations that are presented in the following Chapters of this thesis. Many parts of the theory of continuum mechanics are omitted in what follows. The same is true for the discussion of the calculus of variations and any other mathematical field that is touched. Thus, the presentation is not meant to be comprehensive. For details on rigorous mathematical proofs of the formulas given, the references provided in the course of the Chapter may be consulted, among others. Specific notation and conventions used are introduced when applied for the first time in this text.

3.1 Continuum Bodies and Motion

The topics covered in this Section are mainly based on the ideas as presented in Oden (2011). Continuum mechanics deals with the description of deformable bodies, where the setting is three-dimensional Euclidean space \mathcal{E} . The space \mathcal{E} corresponds to space \mathbb{R}^3 equipped with the Euclidean norm $\|\mathbf{X}\| = \sqrt{\mathbf{X} \cdot \mathbf{X}}$ and thus with an inner product. For details on the definition and properties of Euclidean space see e.g. Flanagan and Kazdan (1990); Fleming (1977). A body \mathcal{B} resides at different regions of space as time passes, where these subsets of \mathcal{E} are denoted the configurations of \mathcal{B} . It is useful to define a certain configuration of the body with known physical state and geometry, termed its reference configuration Ω_0 , which is an open, bounded, connected subset of \mathbb{R}^3 with smooth boundary $\partial\Omega_0$. All other configurations after deformation can then be related to this unique configuration. The fundamental principle of continuum mechanics is that bodies are assumed to be comprised of an infinitely large number of particles, called material points. These are identified using labels \mathbf{X} representing their coordinates in the reference configuration with respect to a fixed Cartesian coordinate frame. Thus, a generic body \mathcal{B} can be defined as

$$\mathcal{B} = \{\mathbf{X} | \mathbf{X} = X_i \mathbf{e}_i \in \overline{\Omega}_0\}$$

for a suitable orthonormal basis $\{\mathbf{e}_1, \mathbf{e}_2, \mathbf{e}_3\}$ and origin \mathbf{o} . Here and in what follows repeated indices imply the use of Einstein's summation convention, unless stated otherwise, see e.g. Gurtin et al. (2010); Holzapfel (2000); Tadmor et al. (2012). The notation $\overline{\Omega}_0$ denotes the closure of Ω_0 , i.e. $\Omega_0 \cup \partial\Omega_0$.

When a body resides at its reference configuration Ω_0 at time $t = 0$, a material point's position in space is located by the vector $\mathbf{X} = X_i \mathbf{e}_i$, where X_i are called material coordinates. Actually, any time t that is convenient for the problem at hand may be chosen to define the reference configuration. Tracing the body \mathcal{B} as it changes configurations over time, its current configuration $\Omega_t \subset \mathbb{R}^3$ can be associated with a particular instant of time t . Material points are brought to new positions via a smooth vector-valued mapping

$$\mathbf{x} = \boldsymbol{\varphi}(\mathbf{X}, t), \tag{3.1}$$

shown in Figure 3.1, where x_i are termed the spatial coordinates. In this thesis the coordinate

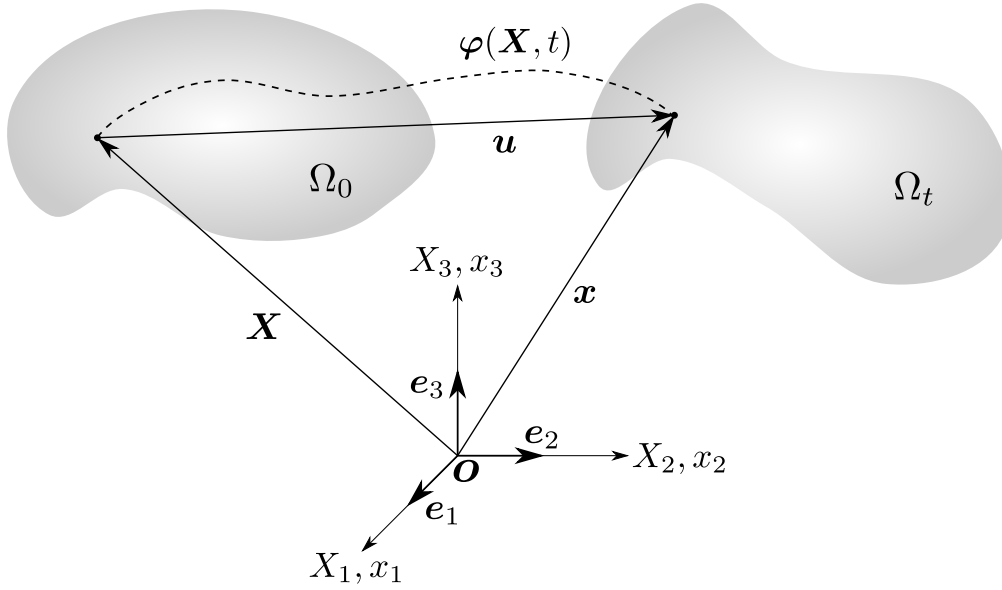


Figure 3.1: Motion of a continuum body, adapted from Oden (2011).

axes of the material and spatial coordinates are assumed to coincide and the basis vectors are taken to be the standard definition used in Cartesian coordinate frames.

The formulation used in (3.1) is called material description or Lagrangian description of motion. A motion that is independent of time t is denoted a deformation, according to Holzapfel (2000); Truesdell and Noll (2004). The material description defines motion, or any other quantity of interest, in terms of the material coordinates (X_1, X_2, X_3) and time t , in general. It is used in situations, when the focus is on tracing particles as the configuration of a body changes. An alternative choice of definition is referred to as the Eulerian description, where \mathbf{x} and time t are taken as the independent variables of the problem. In this formulation attention is paid to spatial points, rather than material points. It is especially popular in fluid mechanics, but can also be found in solid mechanics, depending on the nature of the problem under investigation, see e.g. Bonet and Wood (2008). In this thesis the Lagrangian description is an appropriate means to express the relevant quantities and is used exclusively in the following.

The trajectory of \mathbf{X} , given as the one-parameter family $\{\varphi(\mathbf{X}, t)\}$, allows to track the positions occupied by a material point and is shown as the dashed line in Figure 3.1. There are certain criteria that have to be met in order for φ to represent the motion of a continuum body. It has to be differentiable and injective, except possibly at boundary points. In addition to that, it must be orientation preserving. In mathematical terms this may be expressed as

$$\det \nabla \varphi(\mathbf{X}, t) > 0. \quad (3.2)$$

Inequality (3.2) means that the body must not penetrate itself or alter the material coordinates' orientation. The displacement of material point \mathbf{X} is given by

$$\mathbf{u} = \varphi(\mathbf{X}) - \mathbf{X}, \quad (3.3)$$

as illustrated in Figure 3.1.

3.2 Measures of Deformation

To study geometrical changes of a body different measures of strain have to be introduced. A fundamental quantity is the deformation gradient. It is the basic means describing the structural changes that a body undergoes when it is subject to a motion from its reference state to some new configuration. The geometrical interpretation of the deformation gradient as well as the corresponding derivations presented next can be found in Holzapfel (2000).

It is already known from Section 3.1 that a point \mathbf{X} in the reference configuration is mapped to a new position \mathbf{x} by relation (3.1). Next, the deformation properties of curves and tangent vectors are discussed. Let $\mathbf{X} = \Gamma(\xi) \subset \Omega_0$ be a parametrized material curve related to the reference configuration, depicted in Figure 3.2. As a result of the motion φ the curve is deformed

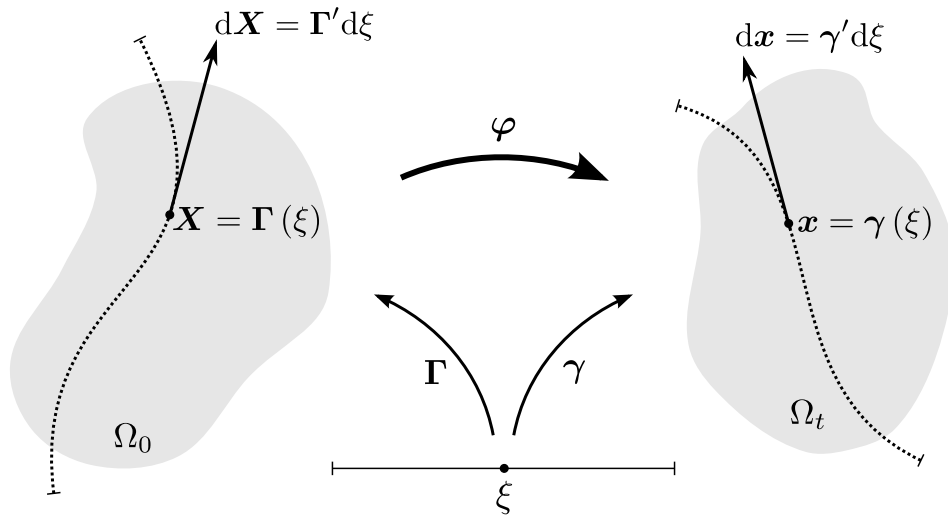


Figure 3.2: Deformation transforming a material curve into its spatial analogue, adapted from Holzapfel (2000).

to become the spatial curve $\mathbf{x} = \gamma(\xi, t) \subset \Omega_t$ at time t . For a fixed time t the deformed curve may be represented as

$$\mathbf{x} = \gamma(\xi, t) = \varphi(\Gamma(\xi), t). \quad (3.4)$$

The tangent vectors to the spatial and the material curves, named the spatial and the material line element, respectively, are expressed as

$$d\mathbf{x} = \gamma'(\xi, t) d\xi \quad \text{and} \quad d\mathbf{X} = \Gamma'(\xi) d\xi, \quad (3.5)$$

where the prime denotes the partial derivative $(\bullet)' = \partial(\bullet)/\partial\xi$. Differentiating (3.4) with respect to ξ , applying the chain rule, yields $\gamma'(\xi, t) = (\partial\varphi(\mathbf{X}, t)/\partial\mathbf{X}) \Gamma'(\xi)$. Then, from (3.5) it can be inferred that

$$d\mathbf{x} = \mathbf{F}(\mathbf{X}, t) d\mathbf{X}, \quad (3.6)$$

where \mathbf{F} is referred to as the deformation gradient, defined by

$$\mathbf{F}(\mathbf{X}, t) = \frac{\partial\varphi(\mathbf{X}, t)}{\partial\mathbf{X}}. \quad (3.7)$$

For an alternative derivation based on calculus, applying Taylor's theorem, see Gonzalez and Stuart (2008). It is supposed that the function of motion $\varphi(\mathbf{X}, t)$ is uniquely invertible and that the inverse relation

$$\mathbf{X} = \varphi^{-1}(\mathbf{x}, t)$$

defines a pull-back operation, which maps points from their spatial position to the reference state, see e.g. Holzapfel (2000); Bonet and Wood (2008). In addition to that, it is assumed that the partial derivative of the inverse motion $\varphi^{-1}(\mathbf{x}, t)$ with respect to \mathbf{x} exists such that

$$\mathbf{F}^{-1}(\mathbf{x}, t) = \frac{\partial \varphi^{-1}(\mathbf{x}, t)}{\partial \mathbf{x}}.$$

Then, the inverse deformation gradient $\mathbf{F}^{-1}(\mathbf{x}, t)$ transforms spatial line elements $d\mathbf{x}$ to material line elements $d\mathbf{X}$ via relation $d\mathbf{X} = \mathbf{F}^{-1}(\mathbf{x}, t) d\mathbf{x}$. In what follows, \mathbf{F} is printed without its arguments unless there is an explicit dependence on one or both of the independent variables. The same holds for the inverse deformation gradient \mathbf{F}^{-1} . The deformation gradient is a second-order tensor, which in general is not symmetric and nonsingular, implying $\det \mathbf{F} \neq 0$. It is the critical quantity in the investigation of the deformation of continuum bodies describing the local deformation in the neighborhood of a point. From (3.6) it can be seen that \mathbf{F} linearly maps a referential line element to a spatial line element; it acts in two different configurations. Therefore, the deformation gradient is called a two-point tensor. If \mathbf{F} depends on \mathbf{X} the deformation is said to be inhomogeneous. On the other hand, if \mathbf{F} does not depend on \mathbf{X} it describes a homogeneous deformation. For $\mathbf{F} = \mathbf{I}$ there is no motion and accordingly $\mathbf{x} = \mathbf{X}$. Differentiating (3.3) with respect to \mathbf{X} and applying (3.7) it can be deduced that an alternative definition of the deformation gradient is

$$\mathbf{F} = \frac{\partial \mathbf{u}}{\partial \mathbf{X}} + \mathbf{I},$$

where the second-order tensor $\partial \mathbf{u} / \partial \mathbf{X} = \nabla \mathbf{u}$ is called the displacement gradient tensor.

To see how unit normals to infinitesimal material surface elements are transformed to their spatial counterparts the mapping of volume elements is discussed next, see Bonet and Wood (2008). Let dV be an infinitesimal volume element in the body's reference configuration, given as

$$dV = dX_1 dX_2 dX_3.$$

Applying the push-forward operation (3.6) to the corresponding material vectors $d\mathbf{X}_i = dX_i \mathbf{e}_i$, where $i = 1, 2, 3$ (no summation), gives

$$\begin{aligned} d\mathbf{x}_1 &= \mathbf{F} d\mathbf{X}_1 = \frac{\partial \varphi(\mathbf{X})}{\partial X_1} dX_1, \\ d\mathbf{x}_2 &= \mathbf{F} d\mathbf{X}_2 = \frac{\partial \varphi(\mathbf{X})}{\partial X_2} dX_2, \\ d\mathbf{x}_3 &= \mathbf{F} d\mathbf{X}_3 = \frac{\partial \varphi(\mathbf{X})}{\partial X_3} dX_3. \end{aligned} \tag{3.8}$$

Using relations (3.8) the deformed volume can be computed as

$$dv = d\mathbf{x}_1 \cdot (d\mathbf{x}_2 \times d\mathbf{x}_3) = \underbrace{\frac{\partial \varphi(\mathbf{X})}{\partial X_1} \cdot \left(\frac{\partial \varphi(\mathbf{X})}{\partial X_2} \times \frac{\partial \varphi(\mathbf{X})}{\partial X_3} \right)}_{\det \mathbf{F}} dX_1 dX_2 dX_3, \tag{3.9}$$

where the mixed product on the right hand side of (3.9)₂ is equivalent to the determinant of the deformation gradient, called the Jacobian J . Here and in what follows, the dot represents the scalar product between two vectors. Thus, the relation between an infinitesimal volume element in its reference state and its current configuration reads

$$dv = JdV. \quad (3.10)$$

The transformation (3.10) is illustrated in the below Figure 3.3. Now, the relation between

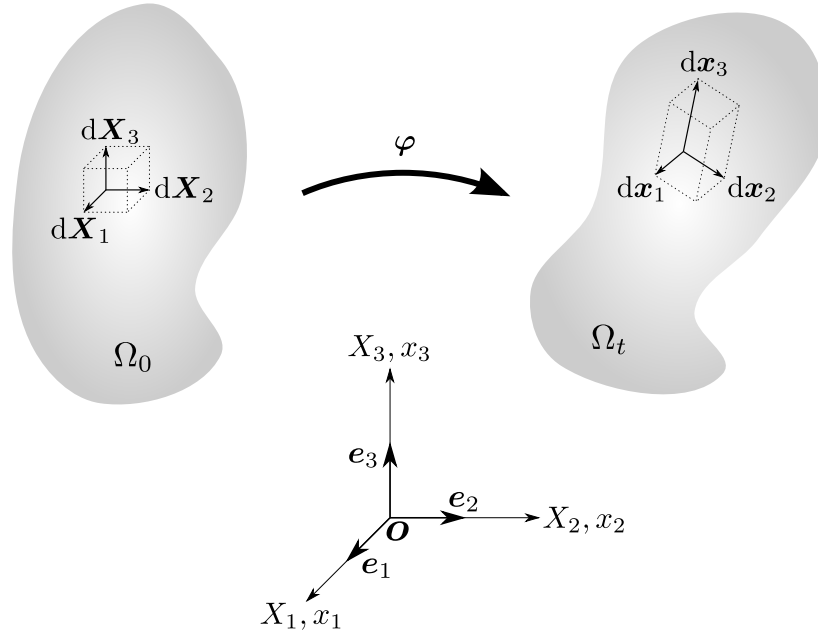


Figure 3.3: Volume change, adapted from Bonet and Wood (2008).

reference and spatial surface elements can be established, following the derivations in Holzapfel (2000). Let $d\mathbf{S} = dS\mathbf{N}$ be an infinitesimal material surface element. Then, $ds = ds\mathbf{n}$ denotes the element at its current configuration. Using these definitions with (3.10) an infinitesimal volume element at its spatial position may be expressed as

$$dv = ds \cdot d\mathbf{x} = Jd\mathbf{S} \cdot d\mathbf{X}, \quad (3.11)$$

where $d\mathbf{X}$ is considered an arbitrary material line element. In virtue of (3.6) relation (3.11) can be rewritten to give

$$\underbrace{(\mathbf{F}^T ds - Jd\mathbf{S})}_{\mathbf{0}} \cdot d\mathbf{X} = 0,$$

leading to the below expression

$$ds = \underbrace{J\mathbf{F}^{-T}}_{\text{Cof } \mathbf{F}} d\mathbf{S}. \quad (3.12)$$

Equation (3.12) provides a connection between infinitesimal surface elements in the reference and current configuration and is referred to as Nanson's formula.

Next, another measure of deformation is introduced. Based on the ideas in Bonet and Wood (2008) let $d\mathbf{X}_1$ and $d\mathbf{X}_2$ be two material line elements in the neighborhood of a point \mathbf{X} that

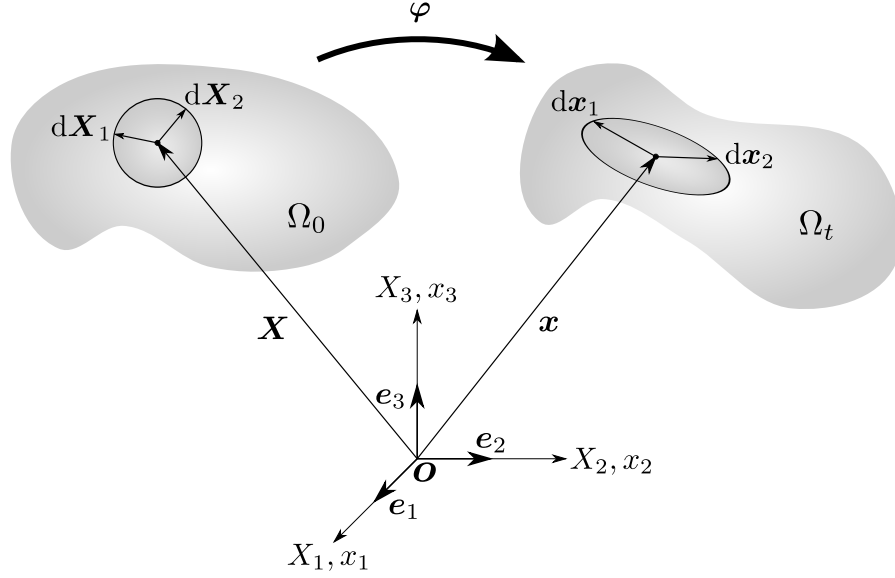


Figure 3.4: Deformation taking material line elements $d\mathbf{X}_1$ and $d\mathbf{X}_2$ to their spatial configurations $d\mathbf{x}_1$ and $d\mathbf{x}_2$, adapted from Bonet and Wood (2008).

are transformed during a certain motion to become the spatial line elements $d\mathbf{x}_1$ and $d\mathbf{x}_2$, as shown in Figure 3.4. The deformation involves stretching as well as a change in the angle between the line elements. To investigate this the scalar product $d\mathbf{x}_1 \cdot d\mathbf{x}_2$ is expressed in terms of the material line elements using (3.6)

$$d\mathbf{x}_1 \cdot d\mathbf{x}_2 = \mathbf{F}d\mathbf{X}_1 \cdot \mathbf{F}d\mathbf{X}_2. \quad (3.13)$$

Switching from direct tensor to matrix notation the product on the right hand side of (3.13) can be written as

$$(\mathbf{F}d\mathbf{X}_1)^T (\mathbf{F}d\mathbf{X}_2) = d\mathbf{X}_1^T \mathbf{F}^T \mathbf{F}d\mathbf{X}_2 = d\mathbf{X}_1^T \mathbf{C}d\mathbf{X}_2. \quad (3.14)$$

For an overview of common notation used in continuum mechanics see e.g. Spencer (1980). The quantity $\mathbf{C} = \mathbf{F}^T \mathbf{F}$ in (3.14) is a second-order tensor called the right Cauchy-Green deformation tensor, which also goes by the name of Green deformation tensor. The first name comes from the fact that it is defined in terms of the product $\mathbf{F}^T \mathbf{F}$, where \mathbf{F} is multiplied from the right. Changing back to tensor notation yields

$$d\mathbf{X}_1^T \mathbf{C}d\mathbf{X}_2 = d\mathbf{X}_1 \cdot \mathbf{C}d\mathbf{X}_2.$$

From (3.14) it can be seen that \mathbf{C} acts on material line elements. Thus, it is denoted a material tensor. The discussion of the following mathematical properties can be found in Holzapfel (2000). The right Cauchy-Green deformation tensor is symmetric and positive definite at each $\mathbf{X} \in \Omega_0$. Therefore,

$$\mathbf{C} = \mathbf{F}^T \mathbf{F} = (\mathbf{F}^T \mathbf{F})^T = \mathbf{C}^T \quad (3.15)$$

with $\mathbf{u} \cdot \mathbf{C}\mathbf{u} > 0$ for all $\mathbf{u} \neq 0$. The spatial analogue to (3.15) is the left Cauchy-Green deformation tensor \mathbf{b}

$$\mathbf{b} = \mathbf{F}\mathbf{F}^T = (\mathbf{F}\mathbf{F}^T)^T = \mathbf{b}^T, \quad (3.16)$$

which is symmetric and positive definite at every $\mathbf{x} \in \Omega_t$, thus satisfying $\mathbf{u} \cdot \mathbf{b}\mathbf{u} > 0$ for all $\mathbf{u} \neq \mathbf{0}$. The notion of positive definiteness implies that the symmetric tensors \mathbf{C} and \mathbf{b} have positive eigenvalues, see e.g. Strang (2009, 2007). Even though spatial quantities do not play a major role in this thesis the left Cauchy-Green tensor \mathbf{b} is introduced here, as it is relevant to the formulation of the following theorem.

Before actually defining a measure of strain in a large-deformation setting an important property of the deformation gradient \mathbf{F} , going by the name of polar decomposition theorem, is discussed. The following derivations are mainly based on the texts by Oden (2011) and Holzapfel (2000). The polar decomposition theorem postulates that the deformation gradient tensor \mathbf{F} can be factored to give

$$\mathbf{F} = \mathbf{R}\mathbf{U} = \mathbf{v}\mathbf{R}, \quad (3.17)$$

where \mathbf{R} is assumed proper orthogonal and \mathbf{U} and \mathbf{v} are supposed unique symmetric and positive definite tensors. For a tensor to be proper orthogonal properties

$$\mathbf{R}^T \mathbf{R} = \mathbf{I}, \quad \det \mathbf{R} = 1 \quad (3.18)$$

must hold. In addition to that, there exists a relation of the form

$$\mathbf{U}^2 = \mathbf{F}^T \mathbf{F} = \mathbf{C}. \quad (3.19)$$

To see that (3.18)₁ is satisfied use $\mathbf{R} = \mathbf{F}\mathbf{U}^{-1}$, according to (3.17)₁, with (3.19) in (3.18)₁ and keep in mind that \mathbf{U} is symmetric. Thus,

$$\begin{aligned} \mathbf{R}^T \mathbf{R} &= (\mathbf{F}\mathbf{U}^{-1})^T \mathbf{F}\mathbf{U}^{-1} = \mathbf{U}^{-T} \mathbf{F}^T \mathbf{F} \mathbf{U}^{-1} = \mathbf{U}^{-T} \mathbf{U}^2 \mathbf{U}^{-1} \\ &= (\mathbf{U}\mathbf{U}^{-1})^T \mathbf{U}\mathbf{U}^{-1} = \mathbf{I}. \end{aligned}$$

For the determinants of the right Cauchy-Green tensor \mathbf{C} and tensor \mathbf{U} it may be found from (3.19) that

$$\begin{aligned} \det \mathbf{C} &= \det (\mathbf{F}^T \mathbf{F}) = \det (\mathbf{F}^T) \det \mathbf{F} = (\det \mathbf{F})^2, \\ \det \mathbf{U} &= \det \sqrt{\mathbf{C}} = \det \mathbf{F} \end{aligned} \quad (3.20)$$

hold, see Tadmor et al. (2012). Then, combining (3.17)₁ and (3.20) confirms (3.18)₂, yielding

$$\det \mathbf{R} = \det (\mathbf{F}\mathbf{U}^{-1}) = \det \mathbf{F} \frac{1}{\det \mathbf{U}} = 1.$$

Thus, it can be seen that tensor \mathbf{R} is proper orthogonal, which in geometrical terms defines a rotation. Using (3.17)₂, \mathbf{v} may be expressed as

$$\mathbf{v} = \mathbf{R}\mathbf{U}\mathbf{R}^T. \quad (3.21)$$

Multiplying (3.21) by \mathbf{R} from the right gives

$$\mathbf{v}\mathbf{R} = \mathbf{R}\mathbf{U}\mathbf{R}^T \mathbf{R} = \mathbf{R}\mathbf{U} = \mathbf{F},$$

as hypothesized before. From definitions (3.15) and (3.16), using (3.17)₁ and (3.17)₂, respectively, one finds that

$$\mathbf{C} = \mathbf{U}^T \mathbf{R}^T \mathbf{R} \mathbf{U} = \mathbf{U}^T \mathbf{U} = \mathbf{U}^2, \quad (3.22)$$

$$\mathbf{b} = \mathbf{v}\mathbf{R}\mathbf{R}^T \mathbf{v} = \mathbf{v}\mathbf{v}^T = \mathbf{v}^2, \quad (3.23)$$

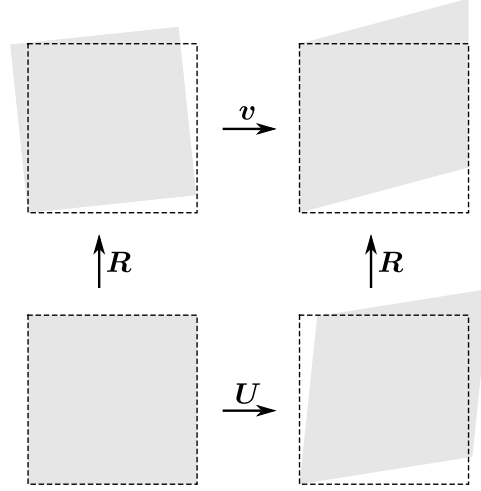


Figure 3.5: Rotational and stretch contributions of the deformation gradient applied to a square geometry, adapted from Oden (2011).

where the unique tensors \mathbf{U} and \mathbf{v} , as introduced in (3.17), are called the right and left stretch tensors, respectively. Thus, the polar decomposition theorem states that the deformation imposed by a motion can be split into a pure rotation \mathbf{R} followed by a distortion or vice versa, as illustrated in Figure 3.5. From (3.22) it can be seen immediately that the right Cauchy-Green deformation tensor is rotation free and just exhibits stretching properties. Therefore, applying \mathbf{C} in general is more meaningful than using \mathbf{F} directly, see e.g. Gonzalez and Stuart (2008).

To use the polar decomposition theorem (3.17) in practical computations one has to determine \mathbf{U} or \mathbf{v} , which by (3.22) and (3.23) are defined as the matrix square roots of \mathbf{C} and \mathbf{b} , respectively. To get these it is useful to apply the spectral decomposition of \mathbf{C} or \mathbf{b} . For the left Cauchy-Green tensor this reads

$$\mathbf{C} = \sum_{\alpha=1}^3 \lambda_{\alpha}^{\mathbf{C}} \mathbf{\Lambda}_{\alpha}^{\mathbf{C}} \otimes \mathbf{\Lambda}_{\alpha}^{\mathbf{C}},$$

where $\lambda_{\alpha}^{\mathbf{C}}$ and $\mathbf{\Lambda}_{\alpha}^{\mathbf{C}}$ are the eigenvalues and eigenvectors of \mathbf{C} , respectively, see e.g. Tadmor et al. (2012). The eigenvalues and eigenvectors can be obtained from the characteristic equation, see e.g. Holzapfel (2000). From that the right stretch tensor may be expressed in terms of $\lambda_{\alpha}^{\mathbf{C}}$ and $\mathbf{\Lambda}_{\alpha}^{\mathbf{C}}$, given by

$$\mathbf{U} = \sum_{\alpha=1}^3 \sqrt{\lambda_{\alpha}^{\mathbf{C}}} \mathbf{\Lambda}_{\alpha}^{\mathbf{C}} \otimes \mathbf{\Lambda}_{\alpha}^{\mathbf{C}}.$$

To determine \mathbf{v} the same procedure as outlined before can be applied to \mathbf{b} . Now, everything is at hand to decompose the deformation gradient \mathbf{F} into a pure rotation and a pure stretch contribution.

In order to introduce a measure of strain that is of interest in the formulation of nonlinear CDT in the succeeding Chapter, the change in the scalar product of elemental vectors $d\mathbf{X}$ and $d\mathbf{x}$ due to a certain motion

$$d\mathbf{x}_1 \cdot d\mathbf{x}_2 - d\mathbf{X}_1 \cdot d\mathbf{X}_2 = d\mathbf{X}_1 \cdot \mathbf{C} d\mathbf{X}_2 - d\mathbf{X}_1 \cdot d\mathbf{X}_2 \quad (3.24)$$

is investigated now. Switching to matrix notation the right-hand side of (3.24) can be expressed as

$$d\mathbf{X}_1^T \mathbf{C} d\mathbf{X}_2 - d\mathbf{X}_1^T d\mathbf{X}_2 = d\mathbf{X}_1^T (\mathbf{C} - \mathbf{I}) d\mathbf{X}_2.$$

This provides a measure of strain that is of importance in Chapter 4, defined by

$$\mathbf{C} - \mathbf{I} = 2\mathbf{E},$$

i.e.

$$\mathbf{E} = \frac{1}{2} (\mathbf{C} - \mathbf{I}), \quad (3.25)$$

called the Green-Lagrange strain tensor \mathbf{E} , where the normalization factor of $1/2$ is introduced in (3.25) to agree with the definition of strain in small deformation theory, see e.g. Tadmor et al. (2012); Holzapfel (2000). Since tensors \mathbf{C} and \mathbf{I} are symmetric it can be deduced that \mathbf{E} is symmetric, too.

3.3 Traction Forces and Stress

So far, some basic relations from the kinematics of deformable solids have been introduced. The motion causing deformation and strain inside a body leads to interactions between neighboring material points. This is where the notion of stress arises. Following Holzapfel (2000) some of the elementary concepts of stress are introduced in this Section.

Consider a continuum body \mathcal{B} at its current configuration Ω_t with boundary $\partial\Omega_t$, as introduced in Section 3.1. It is assumed that arbitrary distributed forces may act on a certain portion of its outer surface as well as inside the body on an imaginary cutting plane, referred to as external and internal forces, respectively. Let the cutting plane contain a given point $\mathbf{x} \in \Omega_t$. As shown in Figure 3.6, \mathbf{x} is enclosed by an infinitesimal spatial surface element $ds \in \partial\Omega_t$ and attached to it is a surface normal vector pointing outside, denoted \mathbf{n} . As this portion of the surface formerly was located in the interior of \mathcal{B} , created by a cutting operation, an interaction of distributed forces between the two parts of the body is presumed. The resultant force acting on ds is denoted $d\mathbf{f}$ and can be associated with the reference configuration via

$$d\mathbf{f} = \tilde{\mathbf{t}} ds = \tilde{\mathbf{T}} dS \quad (3.26)$$

with

$$\tilde{\mathbf{t}} = \tilde{\mathbf{t}}(\mathbf{x}, t, \mathbf{n}), \quad \tilde{\mathbf{T}} = \tilde{\mathbf{T}}(\mathbf{X}, t, \mathbf{N}). \quad (3.27)$$

Relation (3.27) is referred to as Cauchy's postulate, where $\tilde{\mathbf{t}}$ is the Cauchy traction vector, representing a measure of force per unit current surface area, which acts on the surface element ds with normal \mathbf{n} . The quantity $\tilde{\mathbf{T}}$ is called the first Piola-Kirchhoff traction vector. It has to be noted that this vector corresponds to a resultant force acting on the current configuration, but it is measured with respect to an element of surface area in the undeformed configuration. Hence, it is represented as the dashed traction vector acting on dS in Figure 3.6. Vectors $\tilde{\mathbf{t}}$ and $\tilde{\mathbf{T}}$ have common orientation.

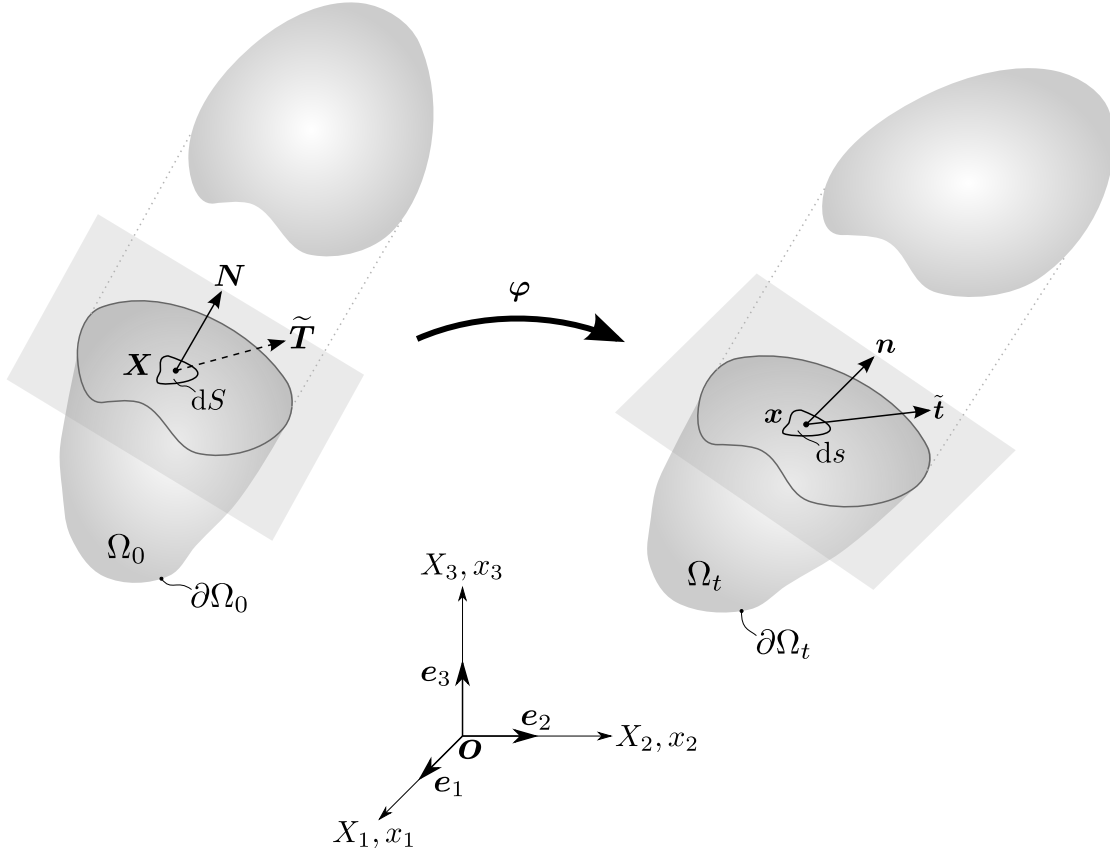


Figure 3.6: Traction vectors associated with infinitesimal surface elements in the referential and current configuration, adapted from Holzapfel (2000).

A fundamental axiom of continuum mechanics is Cauchy's stress theorem, stating that there are two unique second-order tensors $\boldsymbol{\sigma}$ and \boldsymbol{P} such that

$$\tilde{\boldsymbol{t}}(\boldsymbol{x}, t, \boldsymbol{n}) = \boldsymbol{\sigma}(\boldsymbol{x}, t) \boldsymbol{n} \quad (3.28)$$

and

$$\tilde{\boldsymbol{T}}(\boldsymbol{X}, t, \boldsymbol{N}) = \boldsymbol{P}(\boldsymbol{X}, t) \boldsymbol{N}, \quad (3.29)$$

where $\boldsymbol{\sigma}$ is the symmetric spatial Cauchy stress tensor, familiar from small deformation theory. The symmetry property of $\boldsymbol{\sigma}$ is not derived here. It can be established using the balance of angular momentum, see e.g. Gonzalez and Stuart (2008); Holzapfel (2000) or any of the other texts on continuum mechanics cited in this thesis. The quantity \boldsymbol{P} is a two-point tensor called the first Piola-Kirchhoff stress tensor. Thus, Cauchy's stress theorem postulates that traction vectors $\tilde{\boldsymbol{t}}(\boldsymbol{x}, t, \boldsymbol{n})$ and $\tilde{\boldsymbol{T}}(\boldsymbol{X}, t, \boldsymbol{N})$ are linear in \boldsymbol{n} and \boldsymbol{N} , respectively. From (3.28) and (3.29) it can be deduced that

$$\tilde{\boldsymbol{t}}(\boldsymbol{x}, t, \boldsymbol{n}) = -\tilde{\boldsymbol{t}}(\boldsymbol{x}, t, -\boldsymbol{n}), \quad \tilde{\boldsymbol{T}}(\boldsymbol{X}, t, \boldsymbol{N}) = -\tilde{\boldsymbol{T}}(\boldsymbol{X}, t, -\boldsymbol{N}),$$

going by the name of Newton's law of action and reaction.

The last thing to be discussed in this Section is a connection between tensors $\boldsymbol{\sigma}$ and \boldsymbol{P} . From (3.26) and (3.27) it can be found that

$$\tilde{\boldsymbol{t}}(\boldsymbol{x}, t, \boldsymbol{n}) ds = \tilde{\boldsymbol{T}}(\boldsymbol{X}, t, \boldsymbol{N}) dS. \quad (3.30)$$

Plugging (3.28) and (3.29) in (3.30) gives

$$\boldsymbol{\sigma}(\mathbf{x}, t) \mathbf{n} \, ds = \mathbf{P}(\mathbf{X}, t) \mathbf{N} \, dS. \quad (3.31)$$

Applying Nanson's formula (3.12) to (3.31) and rearranging yields

$$\mathbf{P} = J \boldsymbol{\sigma} \mathbf{F}^{-T}, \quad (3.32)$$

called the Piola transformation. The Cauchy stress in terms of the first Piola-Kirchhoff stress reads

$$\boldsymbol{\sigma} = J^{-1} \mathbf{P} \mathbf{F}^T = \boldsymbol{\sigma}^T, \quad (3.33)$$

where (3.33) implies that

$$\mathbf{P} \mathbf{F}^T = \mathbf{F} \mathbf{P}^T.$$

Thus, in general \mathbf{P} is not symmetric. Depending on the problem of interest alternative definitions of stress may be used. The first Piola-Kirchhoff stress tensor can be defined as the product of the deformation gradient \mathbf{F} and a symmetric second-order tensor of the form

$$\mathbf{P} = \mathbf{F} \mathbf{S}, \quad (3.34)$$

where \mathbf{S} is called the second Piola-Kirchhoff stress tensor. In contrast to the first Piola-Kirchhoff stress it is symmetric, but does not admit any physical interpretation. However it has relevance in computational applications, where it appears as a result of the linearization process.

3.4 Elastic Material Response and Objectivity

Having introduced quantities to measure strain and stress before, in what follows another type of equations, called constitutive equations, relating these items is introduced for elastic materials. The outline given in this Section is based on the ideas in Holzapfel (2000).

Materials are called Cauchy-elastic or elastic if stress at a certain time t can be fully described by the deformation state at this instant, not taking into account deformation history. This means that the stresses associated with a Cauchy-elastic material do not depend on the path of deformation, whereas the work done by stresses in general is path-dependent. To describe a body's inherent features constitutive equations, also called equations of state, are introduced. These equations prescribe the stress at all points of a body \mathcal{B} undergoing a motion at a fixed time t . Constitutive equations may be axiomatic, based on a mathematical model or empirical, i.e. related to experimental observations.

The purpose of elastic constitutive equations is to express the Cauchy stress tensor $\boldsymbol{\sigma}(\mathbf{x}, t)$ at every point $\mathbf{x} = \boldsymbol{\varphi}(\mathbf{X}, t)$ in terms of the deformation gradient $\mathbf{F} = \mathbf{F}(\mathbf{X}, t)$. A generic equation of state may be defined as

$$\boldsymbol{\sigma}(\mathbf{x}, t) = \mathbf{g}(\mathbf{F}(\mathbf{X}, t), \mathbf{X}). \quad (3.35)$$

The tensor-valued function \mathbf{g} is called the response function. For homogeneous materials there is no \mathbf{X} -dependence and (3.35) can be written as

$$\boldsymbol{\sigma} = \mathbf{g}(\mathbf{F}), \quad (3.36)$$

defining stress as the tensor function \mathbf{g} with tensor argument \mathbf{F} .

A crucial feature of constitutive equations is objectivity, stated in the form of the principle of material frame-indifference, of importance in Subsection 4.1.3. It postulates that material response must not depend on changes of observer and is a vital ingredient to modeling elastic and plastic material behavior. Simply spoken, this means that constitutive equations must not be influenced by rigid-body motions. To discuss material objectivity the notions of observer and Euclidean transformation have to be introduced first. An observer O is able to measure relative positions and record time. Using the aforementioned abilities the observer captures position \mathbf{x} and time t associated with a physical process, denoted an event. Assume there are two arbitrary events in the setting of Euclidean space defined by (\mathbf{x}_0, t_0) and (\mathbf{x}, t) . Let (\mathbf{x}_0, t_0) be fixed during event (\mathbf{x}, t) . Then, an observer can quantify the distance $|\mathbf{x} - \mathbf{x}_0|$ and the time interval $t - t_0$. A transformation is applied that maps (\mathbf{x}_0, t_0) and (\mathbf{x}, t) to (\mathbf{x}_0^+, t_0^+) and (\mathbf{x}^+, t^+) in a way that does not change the length $|\mathbf{x} - \mathbf{x}_0|$ and difference $t - t_0$. An appropriate spatial mapping can be defined as

$$\mathbf{x}^+ - \mathbf{x}_0^+ = \mathbf{Q}(t)(\mathbf{x} - \mathbf{x}_0),$$

where the proper orthogonal tensor $\mathbf{Q}(t)$ maps vector $\mathbf{x} - \mathbf{x}_0$ to $\mathbf{x}^+ - \mathbf{x}_0^+$. This kind of choice of \mathbf{Q} guarantees that orientations are preserved. Thus, relations

$$\mathbf{x}^+ = \mathbf{c}(t) + \mathbf{Q}(t)\mathbf{x}, \quad t^+ = t + \alpha \quad (3.37)$$

may be introduced, with vector-valued rigid-body translation $\mathbf{c}(t)$ and scalar time-shift α being defined as

$$\mathbf{c}(t) = \mathbf{x}_0^+ - \mathbf{Q}(t)\mathbf{x}_0, \quad \alpha = t_0^+ - t_0.$$

The injective mapping $(3.37)_1$ goes by the name of Euclidean transformation. It defines a change of observer from O to O^+ , which corresponds to a change of the frame of reference.

Next, frame-indifference of various quantities is analyzed, beginning with spatial vector fields and ending with objectivity of response functions, being used as a starting point of the discussion of hyperelasticity and strain-energy functions in the following Section 3.5. To find the transformation of a spatial vector field under a change of observer consider the example shown in Figure 3.7, where the displacement \mathbf{u} is exposed to some rigid-body motion. Applying (3.37) to $\mathbf{u}^+ = \mathbf{y}^+ - \mathbf{x}^+$ gives

$$\mathbf{u}^+ = \mathbf{Q}(t)\mathbf{u}, \quad (3.38)$$

which provides a transformation rule for objective vector fields from configuration Ω_t to state Ω_{t^+} .

To get a mapping relating the functions of motion shown in Figure 3.7, let $\mathbf{x} = \boldsymbol{\varphi}(\mathbf{X}, t)$ be a motion that defines the position of a material point \mathbf{X} at its spatial position at time t , traced by an arbitrary observer O . The same motion, as seen by another observer denoted O^+ , is identified by the mapping $\mathbf{x}^+ = \boldsymbol{\varphi}^+(\mathbf{X}, t^+)$. As the reference position is a fixed state, it is independent of any changes of observer. Therefore, \mathbf{x} and \mathbf{x}^+ are connected via (3.37) to give the transformation of motion functions

$$\boldsymbol{\varphi}^+(\mathbf{X}, t^+) = \mathbf{c}(t) + \mathbf{Q}(t)\boldsymbol{\varphi}(\mathbf{X}, t), \quad t^+ = t + \alpha. \quad (3.39)$$

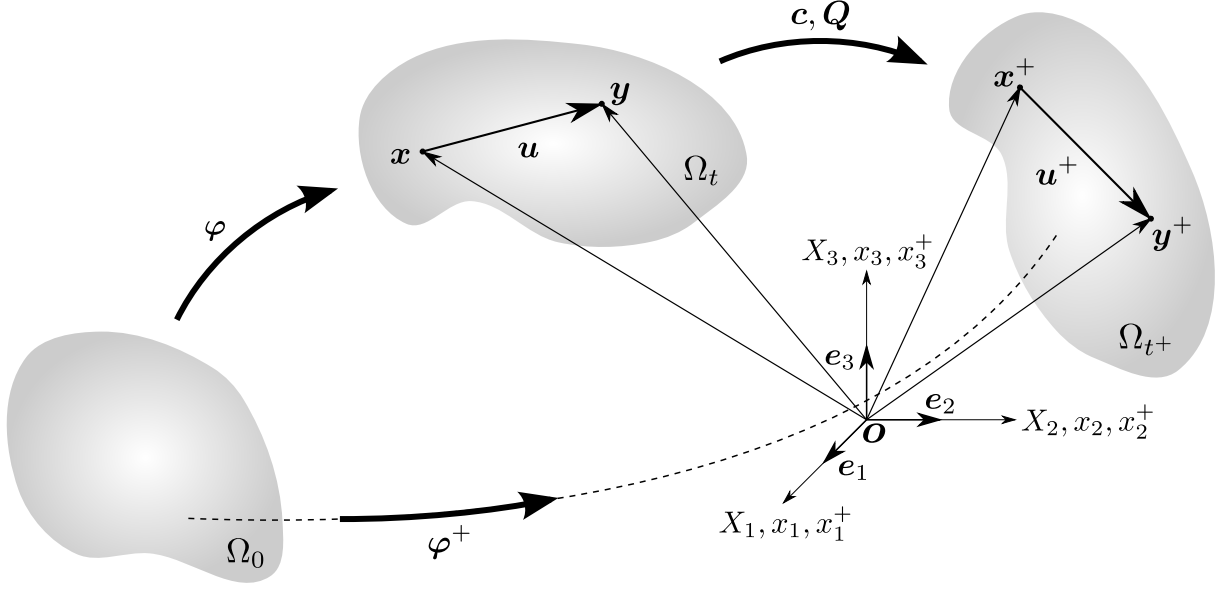


Figure 3.7: The concept of objectivity applied to the spatial displacement field u , where $u^+ = Qu$ and $|u^+| = |u|$, adapted from Holzapfel (2000).

Combining (3.1) with (3.7) and (3.37) it can be found that the deformation gradient associated with configuration Ω_{t+} , as seen by observer O^+ , is given by

$$F^+ = \frac{\partial x^+}{\partial X} = Q \frac{\partial x}{\partial X} = QF. \quad (3.40)$$

Another point of interest is the frame-indifference of stress tensors. Assume dynamical processes defined by tuples (σ^+, φ^+) and (σ, φ) . As the connection between φ^+ and φ has already been established in (3.39), the next goal is to reveal how σ transforms under rigid-body motions. The point of departure is the Cauchy traction vector as defined by (3.28), illustrated in Figure 3.6. In analogy with Figure 3.7 region Ω_t maps to Ω_{t+} and the traction vector becomes $\tilde{t}^+ = \sigma^+ n^+$. As spatial vectors \tilde{t} and n are objective they obey relation (3.38) and thus $Q\tilde{t} = \sigma^+ Qn$, which upon comparison with (3.28) gives

$$\sigma^+ = Q\sigma Q^T. \quad (3.41)$$

The above transformation law (3.41) constitutes a relation for the objectivity of second-order tensors and therefore indicates that σ is frame-indifferent. Discussing stress tensors, what is left now is to check how the first Piola-Kirchhoff stress tensor behaves under superimposed rigid-body motions. Multiplying the Piola transformation (3.32) related to configuration Ω_{t+} by $(F^+)^T$ from the right gives $P^+ (F^+)^T = J^+ \sigma^+$. Using relation $J^+ = J$, valid for any scalar quantity, (3.32), (3.40) and (3.41) it can be found that

$$\begin{aligned} P^+ (QF)^T &= JQ\sigma Q^T \\ P^+ F^T Q^T &= QJ\sigma Q^T = QPF^T Q^T \\ P^+ &= QP. \end{aligned} \quad (3.42)$$

It has to be noted that the two-point tensor P , as F in (3.40), obeys the same transformation law that holds for spatial vector fields and therefore the first Piola-Kirchhoff stress tensor is objective.

To discuss material frame-indifference of constitutive equations some restrictions on response functions have to be established. Let φ^+ be the motion defined in (3.39). Then, as depicted in Figure 3.7, the rigid-body motion takes region Ω_t , occupied by body \mathcal{B} in its current configuration, to region Ω_{t+} and (3.36) becomes $\sigma^+ = \mathbf{g}(\mathbf{F}^+)$. As it is assumed that regions Ω_t and Ω_{t+} have the same material properties function \mathbf{g} applies to both domains. Using (3.40), (3.41) and (3.36) gives relations

$$\sigma^+ = \mathbf{g}(\mathbf{F}^+) = \mathbf{g}(\mathbf{QF}), \quad \sigma^+ = \mathbf{Q}\sigma\mathbf{Q}^T = \mathbf{Q}\mathbf{g}(\mathbf{F})\mathbf{Q}^T. \quad (3.43)$$

From (3.43) it can be deduced that

$$\mathbf{Q}\mathbf{g}(\mathbf{F})\mathbf{Q}^T = \mathbf{g}(\mathbf{QF}). \quad (3.44)$$

Equation (3.44) is a condition that must be satisfied by \mathbf{g} to be objective. It holds for all invertible \mathbf{F} and orthogonal tensors \mathbf{Q} . Applying (3.17)₁ to the right-hand side of (3.44) gives $\mathbf{Q}\mathbf{g}(\mathbf{F})\mathbf{Q}^T = \mathbf{g}(\mathbf{QRU})$. The admissible special case $\mathbf{Q} = \mathbf{R}^T$ leads to the reduced form

$$\mathbf{g}(\mathbf{F}) = \mathbf{R}\mathbf{g}(\mathbf{U})\mathbf{R}^T \quad (3.45)$$

of restriction (3.44), valid for all tensors \mathbf{F} and \mathbf{R} . Recalling relation (3.36) yields the constitutive equation

$$\sigma = \mathbf{R}\mathbf{g}(\mathbf{U})\mathbf{R}^T. \quad (3.46)$$

To check, if the above stress relation obeys frame-indifference it has to be noted that $\sigma^+ = \mathbf{R}^+ \mathbf{g}(\mathbf{U}^+) (\mathbf{R}^+)^T$ holds. In virtue of transformation $\mathbf{R}^+ = \mathbf{QR}$, noting that \mathbf{R} is a two-point tensor, this expression can be rewritten as $\sigma^+ = \mathbf{QR}\mathbf{g}(\mathbf{U})\mathbf{R}^T\mathbf{Q}^T$. Then, using (3.46) transformation rule (3.41) may be recovered, which is the objectivity relation for the second-order stress tensor σ .

A variant of (3.36) can be found from (3.32) using the definition of the volume ratio in terms of the deformation gradient

$$\mathbf{P} = J\sigma\mathbf{F}^{-T} = \det \mathbf{F} \mathbf{g}(\mathbf{F}) \mathbf{F}^{-T} = \mathfrak{G}(\mathbf{F}). \quad (3.47)$$

Thus, (3.47) constitutes a stress relation for the first Piola-Kirchhoff stress tensor. Referring to the procedure outlined before, associated with the frame-indifference of the Cauchy stress, objectivity of (3.47)₃ is discussed in what follows. Assuming a rigid-body motion imposed on the first Piola-Kirchhoff stress, using (3.40) and (3.42), gives

$$\mathbf{P}^+ = \mathfrak{G}(\mathbf{F}^+) = \mathfrak{G}(\mathbf{QF}), \quad \mathbf{P}^+ = \mathbf{QP} = \mathbf{Q}\mathfrak{G}(\mathbf{F}). \quad (3.48)$$

Merging the relations given in (3.48) yields

$$\mathbf{Q}\mathfrak{G}(\mathbf{F}) = \mathfrak{G}(\mathbf{QF}), \quad (3.49)$$

which establishes a necessary and sufficient condition to be satisfied in order for \mathfrak{G} to be objective. Restriction (3.49) must be valid for each invertible deformation gradient tensor \mathbf{F} and all \mathbf{Q} . Again, a reduced form of the stress relation (3.47)₃ may be found from (3.49) in combination with presumption $\mathbf{Q} = \mathbf{R}^T$ and (3.17)₁ to give

$$\mathfrak{G}(\mathbf{F}) = \mathbf{R}\mathfrak{G}(\mathbf{U}). \quad (3.50)$$

The constraint defined by (3.49) and (3.50) corresponds to the reduced form (3.45) based on (3.44).

Yet another form of the stress relation may be found involving the second Piola-Kirchhoff stress tensor. Based on (3.32) and (3.34), using (3.17)₁ with (3.18) and (3.46), it can be found that

$$\mathbf{S} = J \mathbf{F}^{-1} \boldsymbol{\sigma} \mathbf{F}^{-T} = \det \mathbf{U} \mathbf{U}^{-1} \mathfrak{g}(\mathbf{U}) \mathbf{U}^{-1}.$$

Then, taking (3.19) into account a general relation for the computation of the second Piola-Kirchhoff stress may be expressed as

$$\mathbf{S} = \mathfrak{H}(\mathbf{C}). \quad (3.51)$$

Frame-indifference of (3.51) can be deduced from the fact that rigid-body motions do not have an impact on the reference state of a body and thus $\mathbf{S}^+ = \mathbf{S}$ and $\mathbf{C}^+ = \mathbf{C}$.

3.5 Hyperelasticity and Strain-Energy

In Section 3.4 the notion of the constitutive equation has been introduced and discussed with regard to material frame-indifference. So far, general response functions have been discussed, related to elasticity. Next, a specific category of elastic materials is addressed. The associated theory, called hyperelasticity, is of particular interest in this thesis. Its focus is on describing elastic material behavior due to finite deformations of continuum bodies. Hyperelasticity is based on the existence of a Helmholtz free-energy function, denoted Ψ and defined per unit volume of the undeformed body, see e.g. Holzapfel (2000); Bonet and Wood (2008). If Ψ is a function of the single tensor variable \mathbf{F} or any of the other deformation measures presented in Section 3.2 it is denoted the strain-energy function. Hyperelasticity is limited to a special type of perfectly elastic materials, for which holds

$$\mathbf{P} = \mathfrak{G}(\mathbf{F}) = \frac{\partial \Psi(\mathbf{F})}{\partial \mathbf{F}} \quad (3.52)$$

and

$$\boldsymbol{\sigma} = \mathfrak{g}(\mathbf{F}) = J^{-1} \frac{\partial \Psi(\mathbf{F})}{\partial \mathbf{F}} \mathbf{F}^T = J^{-1} \mathbf{F} \left(\frac{\partial \Psi(\mathbf{F})}{\partial \mathbf{F}} \right)^T, \quad (3.53)$$

defining axiomatic material models, making use of the response function notation introduced in (3.47) and (3.36) in the previous Section 3.4. Relation (3.53) can be obtained plugging the right-hand side of (3.52) in (3.32) and taking the symmetry of the Cauchy stress tensor into account. From equations (3.52) and (3.53) it can be seen that stresses can be computed as the partial derivative of strain-energy functions with respect to \mathbf{F} in hyperelasticity.

To define the strain-energy of a perfectly elastic material certain assumptions must hold. It is presumed that the energy at the reference configuration of the body, given as the state of the undeformed material with $\mathbf{F} = \mathbf{I}$ is equal to zero. This is stated via the normalization condition

$$\Psi = \Psi(\mathbf{I}) = 0. \quad (3.54)$$

Plus, the energy of an elastic body increases when it deforms, expressed as

$$\Psi = \Psi(\mathbf{F}) \geq 0. \quad (3.55)$$

In addition to that it is required that Ψ has a global minimum at $\mathbf{F} = \mathbf{I}$, corresponding to the state of thermodynamic equilibrium, and strain space does not contain any further stationary points. Thus, conditions (3.54) and (3.55) guarantee that there are no residual stresses in the reference state of a body.

From the physical point of view it makes sense to prevent cases of infinite expansion of a body or compression to an infinitesimal small volume of the material. This can be stated in the form of the growth conditions

$$\begin{aligned} \Psi(\mathbf{F}) &\rightarrow +\infty & \text{if} & \det \mathbf{F} \rightarrow +\infty, \\ \Psi(\mathbf{F}) &\rightarrow +\infty & \text{if} & \det \mathbf{F} \rightarrow 0^+. \end{aligned} \quad (3.56)$$

A crucial property of Ψ is objectivity. It is clear that the strain-energy must not change when a deformation is superimposed by some rigid-body motion φ^+ , given in (3.39). Using (3.40) the energy must comply with relation

$$\Psi(\mathbf{F}) = \Psi(\mathbf{F}^+) = \Psi(\mathbf{QF}) \quad (3.57)$$

and be valid for any nonsingular deformation and all transformations imposed via orthogonal tensor \mathbf{Q} . Choosing the special case $\mathbf{Q} = \mathbf{R}^T$, following the derivations in Section 3.4, and applying (3.17)₁ gives the equivalent form

$$\Psi(\mathbf{F}) = \Psi(\mathbf{R}^T \mathbf{F}) = \Psi(\mathbf{R}^T \mathbf{R} \mathbf{U}) = \Psi(\mathbf{U}) \quad (3.58)$$

of (3.57), defined for all \mathbf{F} . Hyperelastic material models must be objective with respect to rigid-body motions in order to be meaningful. Relation (3.58) provides a necessary and sufficient condition for frame-indifference indicating that Ψ is just sensitive to the stretching component of the deformation gradient. Alternative forms of (3.58) can be found in terms of (3.15) and (3.25) to give

$$\Psi(\mathbf{F}) = \Psi(\mathbf{C}) = \Psi(\mathbf{E}). \quad (3.59)$$

3.6 Static Equilibrium

In Sections 3.1 to 3.4 selected fields of continuum mechanics have been introduced and essentially been treated independently. The derivation of equilibrium equations, needed to actually define continuum mechanics problems, is discussed next in a variational setting. As the procedure outlined in what follows is based on the choice of an appropriate energy formulation, there is a link to the discussion given in the previous Section 3.5. It is understood that the general strain energy function used later in this Section is equipped with all the features discussed before. In general, there are different ways to derive the set of equilibrium equations, where one option is the use of balance principles, see e.g. Gonzalez and Stuart (2008); Oden (2011); Spencer (1980). In this thesis the derivation of basically all of the equations used is based on variational methods. The calculus of variations provides universal methods to formulate equilibrium equations and in the context of numerical procedures, e.g. the finite element method, the

concept of the variation offers an appealing way to obtain the weak form and its linearization, see e.g. Holzapfel (2000); Bonet and Wood (2008). Therefore, a brief introduction to the theory of variational calculus, purely based on mathematical considerations, is given in the below ‘Extra’ Section.

Extra: The Calculus of Variations. The calculus of variations is the branch of mathematics that deals with the investigation of extrema of certain integral expressions. To define the important notions of the first variation and the Euler-Lagrange equation, needed in this context, the derivations outlined in van Brunt (2004) are taken as a roadmap for the subsequent paragraphs. In particular, integral formulations $J: X \rightarrow \mathbb{R}$, defined on a normed function space $(X, \|\bullet\|)$, are of interest. To illustrate the mathematical procedure, first the simplest case involving a scalar function y and its first derivative y' , both depending on a single scalar variable x , is discussed. This leads to expressions of the type

$$J(y) = \int_{x_0}^{x_1} f(x, y, y') dx, \quad (3.60)$$

termed functionals. Here, a suitable function space X is $C^2[x_0, x_1]$, which consists of functions having continuous second derivatives on the interval $[x_0, x_1]$ and $\|\bullet\|$ corresponds to the usual definition of the Euclidean norm, see e.g. Flanigan and Kazdan (1990); Fleming (1977). Depending on the type of problem under investigation different spaces and norms have to be considered. Let

$$S = \{y \in C^2[x_0, x_1] : y(x_0) = y_0 \text{ and } y(x_1) = y_1\},$$

then (3.60) has a local maximum at $y \in S$ if there exists a scalar $\epsilon > 0$ that makes $J(\hat{y}) - J(y) \leq 0$ for all $\hat{y} \in S$ in a way that $\|\hat{y} - y\| < \epsilon$. According to this definition it can be deduced that (3.60) attains a local minimum at $y \in S$ if y constitutes a local maximum in space S for $-J$. The functions denoted \hat{y} , introduced before, can be interpreted as perturbations of y in its ϵ -neighborhood, illustrated in Figure 3.8. Provided conditions $\hat{y} \in S$ and $\|\hat{y} - y\| < \epsilon$ hold, then there lives an η in space $C^2[x_0, x_1]$ such that

$$\hat{y} = y + \epsilon \eta.$$

All perturbations \hat{y} can be constructed defining an appropriate set of functions

$$H = \{\eta \in C^2[x_0, x_1] : \eta(x_0) = \eta(x_1) = 0\}, \quad (3.61)$$

where ϵ may be arbitrarily small.

Now, the variational problem can be stated as follows: given values $y_0, y_1 \in \mathbb{R}$, find function $y \in C^2[x_0, x_1]$ with $y(x_0) = y_0$ and $y(x_1) = y_1$ which renders J a local extremum at $y \in S$. This special type of formulation is referred to as a fixed endpoint variational problem. To find the answer, assume that there exists a local extremum $y \in S$. Further, suppose here that y defines a local maximum of J . Hence, there must be an $\epsilon > 0$ implying $J(\hat{y}) - J(y) \leq 0$ for all $\hat{y} \in S$ satisfying $\|\hat{y} - y\| < \epsilon$. What is more, for any $\hat{y} \in S$ there exists an $\eta \in H$ allowing for the construction of a perturbation \hat{y} . Under the assumption that ϵ is small Taylor’s theorem may be employed to give

$$\begin{aligned} f(x, \hat{y}, \hat{y}') &= f(x, y + \epsilon \eta, y' + \epsilon \eta') \\ &= f(x, y, y') + \epsilon \left\{ \frac{\partial f}{\partial y} \eta + \frac{\partial f}{\partial y'} \eta' \right\} + O(\epsilon^2), \end{aligned} \quad (3.62)$$

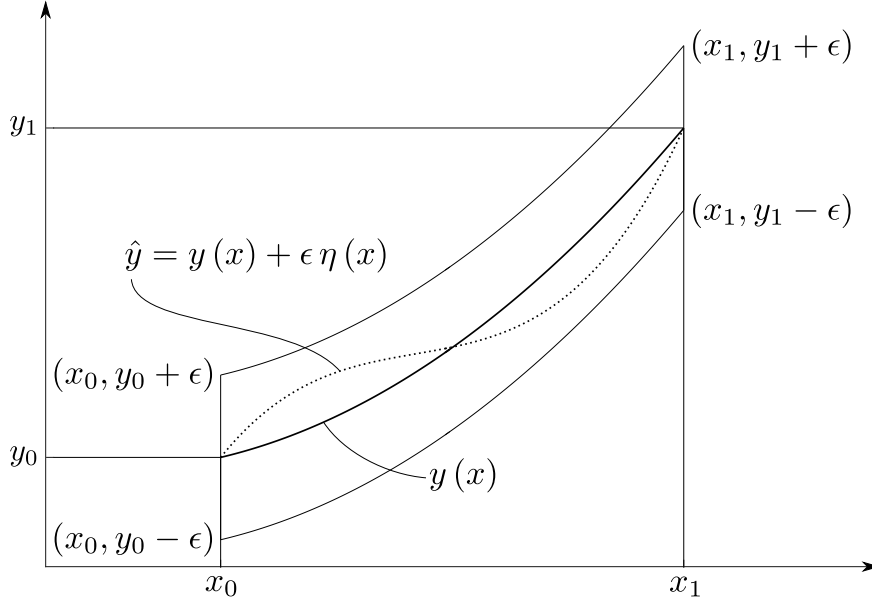


Figure 3.8: Function $y(x)$ and its ϵ -neighborhood with perturbation $\hat{y}(x)$, adapted from van Brunt (2004).

where ‘big Oh’ O refers to the Landau order symbol. Its use implies that the magnitude of the error

$$f(x, \hat{y}, \hat{y}') - f(x, y, y') - \epsilon \left\{ \frac{\partial f}{\partial y} \eta + \frac{\partial f}{\partial y'} \eta' \right\}$$

in the approximation of $f(x, \hat{y}, \hat{y}')$ tends to zero at least as quick as ϵ^2 for $\epsilon \rightarrow 0$, see e.g. Gonzalez and Stuart (2008); Shima and Nakayama (2010). Suppose f is a function of the arguments x , y and y' . Assume further that $\partial f / \partial y$ and $\partial f / \partial y'$ in (3.62) are evaluated at (x, y, y') . Then,

$$\begin{aligned} J(\hat{y}) - J(y) &= \int_{x_0}^{x_1} f(x, \hat{y}, \hat{y}') dx - \int_{x_0}^{x_1} f(x, y, y') dx \\ &= \int_{x_0}^{x_1} \left\{ \left(f(x, y, y') + \epsilon \left\{ \frac{\partial f}{\partial y} \eta + \frac{\partial f}{\partial y'} \eta' \right\} + O(\epsilon^2) \right) - f(x, y, y') \right\} dx \\ &= \epsilon \int_{x_0}^{x_1} \left(\frac{\partial f}{\partial y} \eta + \frac{\partial f}{\partial y'} \eta' \right) dx + O(\epsilon^2) \\ &= \epsilon \delta J(\eta, y) + O(\epsilon^2). \end{aligned} \tag{3.63}$$

Here, $\delta J(\eta, y)$ denotes the first variation of (3.60) and η and η' are the variations of y and y' , respectively, often labeled δy and $\delta y'$, see e.g. Holzapfel (2000); Lanczos (1970); Reddy (2002). Thus, from (3.63)₃ and (3.63)₄ it can be deduced that

$$\delta J(\delta y, y) = \int_{x_0}^{x_1} \left(\frac{\partial f}{\partial y} \delta y + \frac{\partial f}{\partial y'} \delta y' \right) dx, \tag{3.64}$$

which provides a rule for the computation of the first variation of functional (3.60). Similar ideas for the derivation of the first variation can be found in Gelfand and Fomin (1963) and Fox (1963). For alternative approaches see e.g. MacCluer (2005); Weinstock (1974). It has to be

kept in mind that the variational process is performed at fixed x , therefore a variation of the independent variable does not exist, see e.g. Lanczos (1970).

Further inspection of result (3.64) reveals that $\delta J(\delta y, y) = -\delta J(-\delta y, y)$, taking into account that in case $\delta y \in H$, then also $-\delta y \in H$. If ϵ is small, the sign of the difference $J(\hat{y}) - J(y)$ is defined by the sign of the first variation, except for the case $\delta J(\delta y, y) = 0$ for all variations $\delta y \in H$. In case $J(y)$ is a local maximum $J(\hat{y}) - J(y)$ must not switch sign for any \hat{y} with $\|\hat{y} - y\| < \epsilon$. Thus, for $J(y)$ to be a local maximum, condition

$$\delta J(\delta y, y) = \int_{x_0}^{x_1} \left(\frac{\partial f}{\partial y} \delta y + \frac{\partial f}{\partial y'} \delta y' \right) dx = 0 \quad \text{for all } \delta y \in H \quad (3.65)$$

must hold. In an analogous manner it can be shown that (3.65) must be valid if J exhibits a local minimum at $y \in S$. It has to be pointed out that (3.65) is a condition for the stationarity of J , but it actually does not immediately imply that an extremum exists. To remove the dependence on $\delta y'$ in (3.65) integration by parts is applied, yielding

$$\begin{aligned} \int_{x_0}^{x_1} \frac{\partial f}{\partial y'} \delta y' dx &= \left. \frac{\partial f}{\partial y'} \delta y \right|_{x_0}^{x_1} - \int_{x_0}^{x_1} \frac{d}{dx} \left(\frac{\partial f}{\partial y'} \right) \delta y dx \\ &= - \int_{x_0}^{x_1} \frac{d}{dx} \left(\frac{\partial f}{\partial y'} \right) \delta y dx. \end{aligned} \quad (3.66)$$

To get result (3.66) it has to be noted that $\delta y(x_0) = \delta y(x_1) = 0$, as defined in (3.61). Plugging (3.66) into (3.65) one obtains

$$\int_{x_0}^{x_1} \left\{ \frac{\partial f}{\partial y} - \frac{d}{dx} \left(\frac{\partial f}{\partial y'} \right) \right\} \delta y dx = 0,$$

where δy is an arbitrary function in H . Then, from

$$\frac{\partial f}{\partial y} - \frac{d}{dx} \left(\frac{\partial f}{\partial y'} \right) = \frac{\partial f}{\partial y} - \frac{\partial^2 f}{\partial x \partial y'} - \frac{\partial^2 f}{\partial y \partial y'} y' - \frac{\partial^2 f}{\partial y' \partial y'} y''$$

it can be seen that for any fixed $y \in C^2[x_0, x_1]$ the mapping $E: [x_0, x_1] \rightarrow \mathbb{R}$ given as

$$E(x) = \frac{\partial f}{\partial y} - \frac{d}{dx} \left(\frac{\partial f}{\partial y'} \right)$$

is continuous on $[x_0, x_1]$, provided f is twice continuously differentiable. It can be shown that if y is an extremal, then $E = 0$ for all $x \in [x_0, x_1]$. Thus,

$$\frac{\partial f}{\partial y} - \frac{d}{dx} \left(\frac{\partial f}{\partial y'} \right) = 0 \quad (3.67)$$

is a condition that must be satisfied for J to have an extremum at $y \in S$. Relation (3.67) is a fundamental result of the calculus of variations, termed the Euler-Lagrange equation. It constitutes a second-order ordinary differential equation, which in general is nonlinear. \triangle

So far, the definitions of the first variation and the Euler-Lagrange equation have been established in a general mathematical context dealing with scalar extremals y of a single scalar argument x . As this thesis is concerned with modeling materials the connection of results (3.64) and (3.67) with continuum mechanics is discussed next, adopting the physical interpretation given in Holzapfel (2000). The principle of stationary potential energy is an important

concept of continuum mechanics that is associated with the calculus of variations. In elastic problems a system is exposed to an infinitely small and virtual displacement that allows for the determination of equilibrium states of the deformed body. This can be figured as a mathematical experiment that actually does not alter the system's configuration, see e.g. Lanczos (1970). In continuum mechanics, when dealing with purely elastic deformations, the analogue to the variation δy in (3.64) is named the first variation of the displacement field or a virtual displacement. To define the virtual displacement, consider a displacement \mathbf{u} that connects a material point \mathbf{X} in the reference configuration and its spatial counterpart \mathbf{x} . Then, assume another arbitrary displacement field \mathbf{w} relating the current configuration and a close by virtual state, which is in the neighborhood of \mathbf{u} . The corresponding total displacement is defined as

$$\bar{\mathbf{u}} = \mathbf{u} + \varepsilon \mathbf{w},$$

with ε a scalar parameter, depicted in Figure 3.9. The first variation of the displacement field is defined as the difference between the two positions of the body in the current configuration

$$\delta \mathbf{u} = \bar{\mathbf{u}} - \mathbf{u} = \varepsilon \mathbf{w},$$

also denoted the virtual displacement. As the name suggests this displacement is not an actual

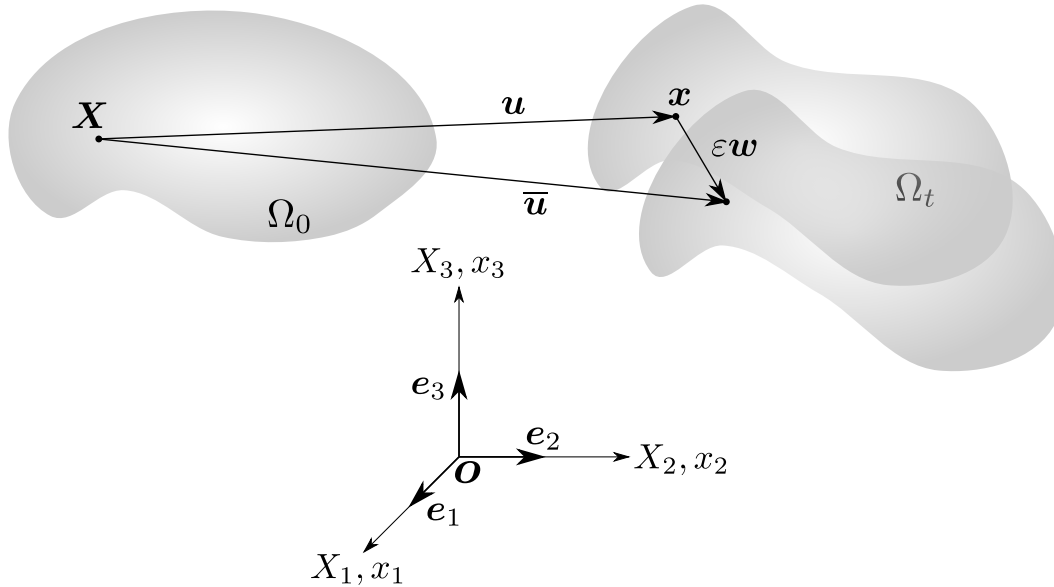


Figure 3.9: Virtual displacement of a continuum body, adapted from Holzapfel (2000).

one, but a fictitious one that is assumed to be infinitesimally small.

To obtain the first variation of a function in its material description the concept of the directional derivative, i.e. Gâteaux derivative, can be applied, see e.g. Bonet and Wood (2008); Flanagan and Kazdan (1990); Tadmor et al. (2012). Let $\mathcal{F} = \mathcal{F}(\mathbf{u})$ be a smooth scalar, vector or tensor function of the single vector argument \mathbf{u} and possibly time t that describes any physical quantity of interest. Then the first variation of \mathcal{F} is defined as

$$\delta \mathcal{F}(\mathbf{u}, \delta \mathbf{u}) = D_{\delta \mathbf{u}} \mathcal{F}(\mathbf{u}) = \frac{d}{d\varepsilon} \mathcal{F}(\mathbf{u} + \varepsilon \delta \mathbf{u})|_{\varepsilon=0}, \quad (3.68)$$

with $D_{\delta \mathbf{u}} \mathcal{F}(\mathbf{u})$ denoting the directional derivative of \mathcal{F} in the direction of $\delta \mathbf{u}$, which may also be expressed as

$$\delta \mathcal{F}(\mathbf{u}, \delta \mathbf{u}) = \frac{\partial \mathcal{F}}{\partial \mathbf{u}} \cdot \delta \mathbf{u}. \quad (3.69)$$

The above rule (3.69) is useful in practical calculations, see also Flanigan and Kazdan (1990); Tadmor et al. (2012), where in a more general setting the (\cdot) represents an appropriate inner product, depending on the type of function \mathbf{u} . Even though the notion of the first variation is not discussed in the context of integral expressions here, it obeys the same principles as introduced before. Note that (3.69) is the analogue of (3.64). Another important result from the theory of the calculus of variations is the commutative property

$$\delta(\nabla \mathbf{u}) = \nabla(\delta \mathbf{u}), \quad (3.70)$$

which comes in handy in applications, see e.g. Holzapfel (2000); Lanczos (1970); Reddy (2002).

Up to now, the notion of the first variation and a rule for its calculation have been established in the context of continuum mechanics. What is left is to find a condition analogous to (3.67). This involves the definitions of hyperelastic materials and the strain-energy function given in Section 3.5. Here and in what follows, it is assumed that loads do not depend on a body's motion. Loads whose orientations do not adapt according to the deformation of the body are referred to as 'dead' loads. In addition to that, it is supposed that the body is in static or quasi-static equilibrium and is exposed to displacement and traction boundary conditions, denoted Ω_{0u} and $\Omega_{0\sigma}$, respectively. The corresponding potential energy Π is given as the sum of the internal and external potential energies

$$\Pi(\mathbf{u}) = \Pi_{\text{int}}(\mathbf{u}) + \Pi_{\text{ext}}(\mathbf{u}) \quad (3.71)$$

with

$$\Pi_{\text{int}}(\mathbf{u}) = \int_{\Omega_0} \Psi(\mathbf{F}(\mathbf{u})) \, dV, \quad \Pi_{\text{ext}}(\mathbf{u}) = - \int_{\Omega_0} \mathbf{B} \cdot \mathbf{u} \, dV - \int_{\partial\Omega_{0\sigma}} \bar{\mathbf{T}} \cdot \mathbf{u} \, dS,$$

where $\Psi = \Psi(\mathbf{F})$ is the strain-energy function per unit reference volume and \mathbf{F} corresponds to the deformation gradient as defined in (3.7). The external potential energy is defined in terms of the body forces \mathbf{B} and the tractions $\bar{\mathbf{T}}$ acting on the surface of the body. Given (3.71) the goal is to find the stationary potential energy, corresponding to a state of equilibrium in the deformed configuration. This is accomplished by applying the definition of the first variation (3.68) to the total potential energy function and setting the result equal to zero to give

$$\delta\Pi(\mathbf{u}, \delta\mathbf{u}) = D_{\delta\mathbf{u}}\Pi(\mathbf{u}) = \frac{d}{d\varepsilon}\Pi(\mathbf{u} + \varepsilon\delta\mathbf{u})|_{\varepsilon=0} = 0 \quad (3.72)$$

or, using (3.69),

$$\delta\Pi(\mathbf{u}, \delta\mathbf{u}) = \frac{\partial\Pi}{\partial\mathbf{u}} \cdot \delta\mathbf{u} = 0. \quad (3.73)$$

This is exactly what corresponds to the Euler-Lagrange equation (3.67) and is known as the principle of stationary potential energy. This means the first variation of the total potential energy must vanish for arbitrary variations $\delta\mathbf{u}$ satisfying the boundary conditions $\delta\mathbf{u} = \mathbf{0}$ on $\partial\Omega_{0u}$, as required in (3.61) in the general mathematical context. Keeping in mind the requirements on strain-energy functions presented in Section 3.5, now the basic tools for finding minima in continuum mechanics problems based on energy formulations are at hand. Extending these to more complicated scenarios involving several independent variables is straightforward and is shown in the following Chapters dealing with the derivations and computations based on nonlinear CDT.

3.7 Finite Elasto-Plastic Deformations

The kinematics underlying nonlinear CDT are based on the geometrical concepts of large elasto-plastic deformations. Therefore, this Section discusses the impact of permanent deformations on the deformation gradient in finite inelasticity and provides an expression for the decomposition of the overall deformation in elastic and plastic parts, based on the derivations in Bonet and Wood (2008).

To understand the nature of strain and its implication on the formulation of kinematics in finite deformation elasto-plasticity the behavior of a volume V , comprised of the neighborhood of a particle P located inside a generic body \mathcal{B} , is investigated as \mathcal{B} is exposed to a motion φ . The neighborhood of P is characterized by the material vector $d\mathbf{X}$. Applying the mapping φ gives the current volume v with its associated vector $d\mathbf{x}$, the spatial counterpart of $d\mathbf{X}$, depicted in Figure 3.10. To get some insight into the local material behavior the following thought

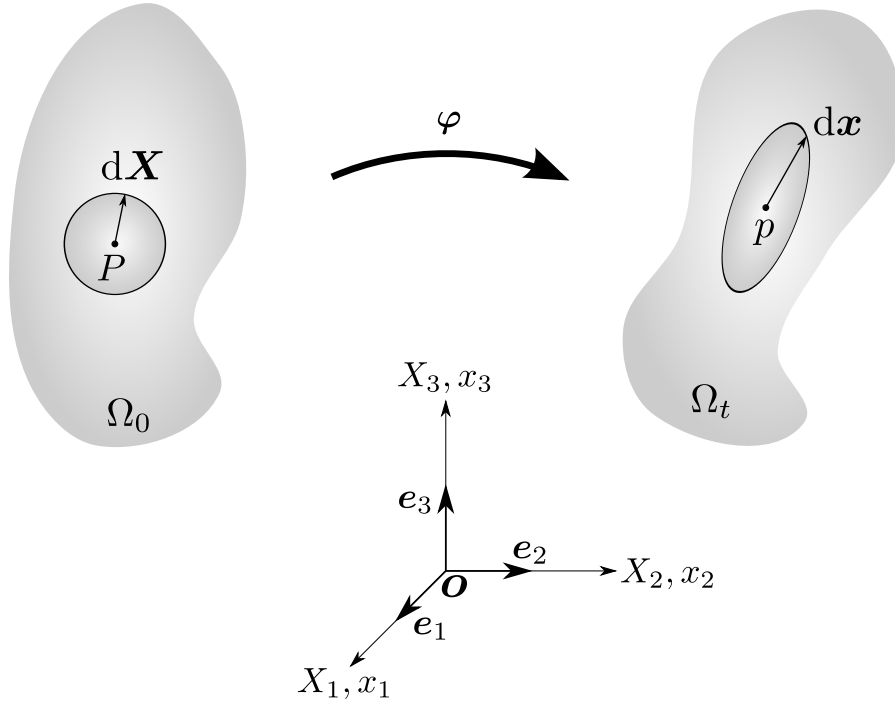


Figure 3.10: Deformation of referential volume V , adapted from Bonet and Wood (2008).

experiment is performed: isolate the volume v from the bulk of \mathcal{B} and assume purely elastic unloading of this portion of the body. Then, the deformation of this portion of material is not changed by imposing any rigid body motions. This state may be thought of as an intermediate unloaded configuration related to the spatial vector $d\tilde{\mathbf{x}}$, see also Borja (2013); Khan and Huang (1995); Lubliner (2008); de Souza Neto et al. (2008). The configurations of the neighborhood of a material point resulting from the unloading procedure are illustrated in Figure 3.11. Since the material under investigation is considered inelastic, the neighborhood in the intermediate state is assumed to exhibit plastic deformation.

As defined in Section 3.2 the push-forward operation (3.6) provides the relation between $d\mathbf{X}$ and $d\mathbf{x}$ in terms of the total deformation \mathbf{F} . Because the local unloading is presumed to be elastic it is natural to attribute it to the elastic contribution \mathbf{F}^e of the overall deformation

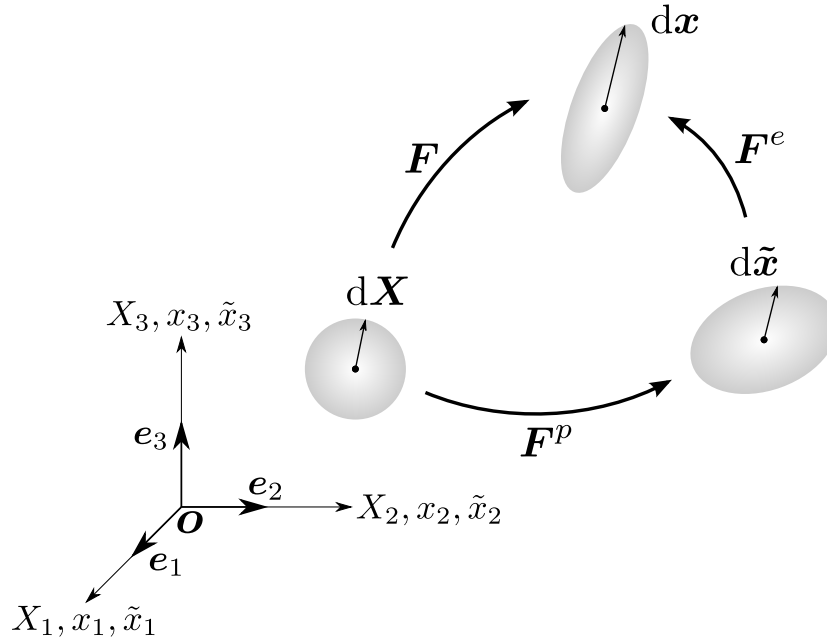


Figure 3.11: Multiplicative decomposition of the deformation gradient, adapted from Bonet and Wood (2008).

that relates vector $d\tilde{x}$ to $d\mathbf{x}$. As pointed out before, the transformation of $d\mathbf{X}$ to $d\tilde{x}$ involves permanent deformation and thus is performed via the plastic contribution of \mathbf{F} , denoted \mathbf{F}^p . For an arbitrarily chosen $d\mathbf{X}$ the relations between the three elemental vectors introduced before are defined by

$$\begin{aligned} d\mathbf{x} &= \mathbf{F}d\mathbf{X}, \\ d\mathbf{x} &= \mathbf{F}^e d\tilde{x}, \\ d\tilde{x} &= \mathbf{F}^p d\mathbf{X}, \end{aligned} \tag{3.74}$$

as illustrated in Figure 3.11. Plugging (3.74)₃ into the right-hand side of (3.74)₂ and comparing with (3.74)₁ yields the multiplicative decomposition

$$\mathbf{F} = \mathbf{F}^e \mathbf{F}^p, \tag{3.75}$$

providing a split of the deformation gradient into elastic and plastic parts, see Lee and Liu (1967) and Lee (1969). A detailed physical interpretation of resolution (3.75), as used in non-linear CDT and founded on the ideas in Bilby et al. (1957), is given in Chapter 4.

It has to be pointed out that even though the deformation gradient can be obtained as the gradient of a smooth mapping, as stated in (3.7), the same does not hold for the elastic and plastic deformations. This is due to the hypothesis of a local stress-free neighborhood v , which in general is not geometrically compatible with the overall spatial configuration of the body. Thus, the setting in Figure 3.11 does not give rise to a globally defined smooth vector field \tilde{x} , and hence \mathbf{F}^e and \mathbf{F}^p cannot be defined as gradients of global mappings.

4 Modeling Microstructure using Nonlinear Continuum Dislocation Theory

All of the quantities introduced in Chapter 3 were related to some generic body, denoted \mathcal{B} . In what follows, using the framework of nonlinear CDT, based on Berdichevsky (2006b); Le and Günther (2014), it is natural to think of \mathcal{B} as a single crystal made of some ductile metal. Specifically, the current Chapter deals with the formation of grain boundaries in single crystals exposed to large plastic deformations. The next Section 4.1 is concerned with modeling grain boundaries as sharp interfaces of a 1st-order laminate structure obtained from nonconvex energy minimization. After that, the model is extended in two directions. In Section 4.2 an enhanced laminate model is derived, where grain boundaries are assumed to have small but finite thickness. Finally, in Section 4.3 it is shown that taking into account resistance to dislocation motion, introducing a dissipation term, affects the nature of nonconvexity of the energy function and in turn has an influence on the orientation of laminate layers.

4.1 Grain Boundaries as Sharp Interfaces

The first model to be discussed is capable to mimic the formation of grain boundaries in single crystals based on the construction of 1st-order laminate structures resulting from nonconvex energy minimization. The presentation is based on Koster, Le and Nguyen (2015), where the present discussion involves more details on the mathematical background of some of the concepts used and the investigation captures an additional energy formulation. The point of departure is an outline of nonlinear CDT. Next, the derivation of equilibrium and jump conditions arising from the theory is given. Then, details of the energy functions employed and the corresponding constitutive equations are presented. Eventually, the construction of a laminate structure, representing the formation of grain boundaries, is illustrated for the case of a plane-strain simple shear deformation.

4.1.1 Foundations of Nonlinear Continuum Dislocation Theory

The basic assumption of nonlinear CDT is that there exists a multiplicative decomposition of the deformation gradient $\mathbf{F} = \partial \mathbf{x} / \partial \mathbf{X}$ in elastic and plastic contributions, according to Bilby et al. (1957), given by

$$\mathbf{F} = \mathbf{F}^e \mathbf{F}^p. \quad (4.1)$$

The plastic deformation can be thought of as a mechanism creating dislocations in the bulk or at the boundary of the crystal or changing the dislocations' positions, not affecting the parallelism of the lattice. The elastic deformation may involve lattice distortions and rotations, while keeping dislocations at fixed positions, see Le and Günther (2014). The interpretation of the decomposition of the deformation gradient is illustrated in Figure 4.1, where the dislocations

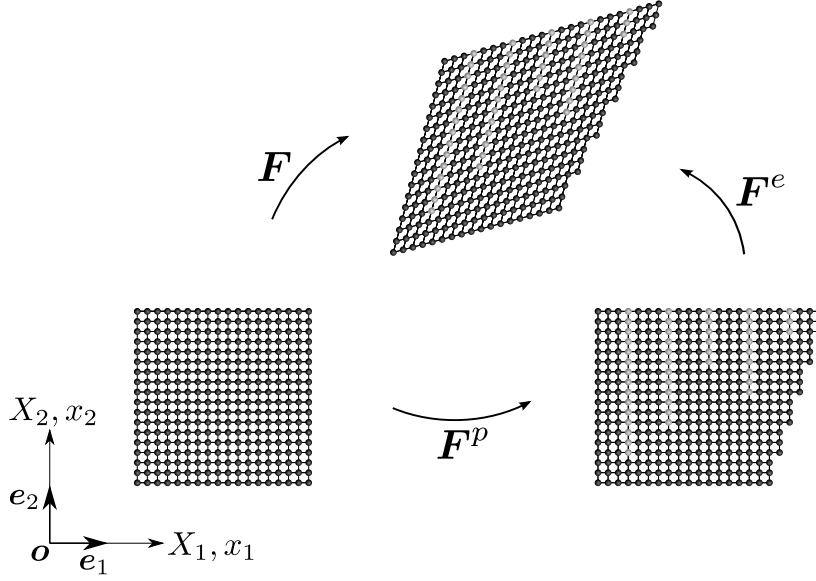


Figure 4.1: Multiplicative decomposition $F = F^e F^p$ in nonlinear CDT.

created by the plastic deformation are indicated by additional half-planes of atoms, represented in light gray color. As required by the theory, lattice vectors do not change when exposed to plastic deformation but adapt with shape vectors when the crystal deforms elastically.

Assuming a single active slip system, the resultant Burgers vector of excess dislocations with dislocation lines crossing an area \mathcal{A} , defined in the reference configuration of the single crystal, was introduced by Ortiz and Repetto (1999) as

$$\mathbf{b}_r = \oint_{\mathcal{C}} \mathbf{F}^p d\mathbf{X}. \quad (4.2)$$

The integration in (4.2) is performed along contour \mathcal{C} , enclosing \mathcal{A} . It was shown by Le and Günther (2014) that the above integral provides a measure of the total closure failure caused by \mathbf{F}^p in the continuum limit, i.e. when the atomic distance approaches zero in a representative volume element having fixed size and exhibiting a fixed dislocation density per area of unit cell. It is assumed that \mathbf{F}^p is continuously differentiable in this continuum limit. Thus, applying Stokes' theorem to (4.2) gives

$$\mathbf{b}_r = - \int_{\mathcal{A}} (\mathbf{F}^p \times \nabla) \mathbf{N} dA,$$

where ∇ is taken with respect to coordinates \mathbf{X} , related to the reference configuration, \mathbf{N} denotes the unit normal to \mathcal{A} and dA corresponds to the surface element. Therefore, the dislocation density tensor may be defined by

$$\mathbf{T} = -\mathbf{F}^p \times \nabla, \quad (4.3)$$

suitable in single slip deformation with known reference state of the crystal. The resultant Burgers vector of excess dislocations, whose dislocation lines cross the infinitesimal area element dA , can be computed as follows

$$\mathbf{b}_r = \mathbf{T} \mathbf{N} dA,$$

revealing similarity to (3.29), where the traction vector is associated with an element of area in the undeformed configuration, as discussed in detail in Section 3.3. Since (4.3) provides a measure of dislocation density related to the reference configuration it is not meaningful in practical situations, where all that can be measured is the current state of a plastically deformed crystal lattice, e.g. using high resolution EBSD, see Kysar et al. (2010) and the references therein. According to Section 3.7 the total deformation is defined as a global map and thus (3.6) can be used with (4.1) in (4.2) to give

$$\mathbf{b}_r = \oint_c \mathbf{F}^{e-1} d\mathbf{x}, \quad (4.4)$$

where c denotes the contour in the current configuration. Thus, the associated spatial dislocation density tensor may be expressed as

$$\mathbf{t} = -\mathbf{F}^{e-1} \times \nabla_{\mathbf{x}}, \quad (4.5)$$

with $\nabla_{\mathbf{x}}$ indicating differentiation with respect to coordinates \mathbf{x} in the current configuration. Relations (4.4) and (4.5) might be more appropriate in situations, where the undeformed configuration of a specimen is not known. It has to be noted that both of the aforementioned definitions are invariant to any superimposed homogeneous plastic deformations, not altering the amount of dislocations in the crystal.

According to Kröner (1992) the elastic deformation \mathbf{F}^e and the dislocation density tensor \mathbf{T} may be regarded as the state variables of nonlinear CDT, as these quantities completely determine the state of the crystal. Since the plastic deformation \mathbf{F}^p depends on cut surfaces and thus on the complete history of the generation of dislocations, involving different mechanisms for dislocation climb or glide, it is not applicable as a state variable. For the same reason the plastic right Cauchy-Green tensor \mathbf{C}^p may not be used as a state variable, either. The dislocation density tensor is not history-dependent, as it is just defined in terms of the Burgers vector and the positions of dislocation lines in the current state. It does not depend on the way dislocations were actually created. Therefore, assuming isothermal processes only, the free energy per unit volume of the crystal is formulated as a function of \mathbf{F}^e and \mathbf{T}

$$\Psi = \Psi(\mathbf{F}^e, \mathbf{T}).$$

As outlined in Section 3.5, an important feature of hyperelastic strain-energy functions is objectivity. To see the impact of rigid-body motions on the deformation in the framework of nonlinear CDT, using (4.1), let \mathbf{R} be a proper orthogonal tensor acting on \mathbf{F} and \mathbf{F}^e to give

$$\mathbf{F}^* = \mathbf{R}\mathbf{F}, \quad \mathbf{F}^{e*} = \mathbf{R}\mathbf{F}^e.$$

Since \mathbf{F}^p represents a linear map that acts on the reference configuration, there is no impact of superimposed rigid-body rotations on the plastic contribution of the deformation, as may be deduced from the discussion in Section 3.4. In addition to that, the starred quantities do neither alter the elastic strain nor the dislocation density and therefore it is expected that rigid-body rotations do not influence the energy. In virtue of (3.59) it may be found that

$$\Psi = \Psi(\mathbf{C}^e, \mathbf{T}), \quad (4.6)$$

see also Gurtin (1981). The elastic right Cauchy-Green tensor in (4.6) is defined by

$$\mathbf{C}^e = \mathbf{F}^{eT} \mathbf{F}^e. \quad (4.7)$$

For a single crystal having only one active slip system the plastic deformation can be expressed as

$$\mathbf{F}^p(\mathbf{X}) = \mathbf{I} + \beta(\mathbf{X}) \mathbf{s} \otimes \mathbf{m}, \quad (4.8)$$

where $\beta(\mathbf{X})$ is the plastic slip and unit vectors \mathbf{s} and \mathbf{m} define the slip system. The vector \mathbf{s} points in the direction of slip, \mathbf{m} is oriented normal to it. From (4.3) the dislocation density tensor can be found in the following form

$$\mathbf{T} = -\mathbf{F}^p \times \nabla = \mathbf{s} \otimes (\nabla \beta \times \mathbf{m}). \quad (4.9)$$

Let all dislocation lines be straight lines pointing in the direction of vector \mathbf{l} , normal to dA , then the resultant Burgers vector of all excess dislocations, whose dislocation lines pierce dA at an angle of 90° , is given by

$$\mathbf{b}_r = \mathbf{s} [(\nabla \beta \times \mathbf{m}) \cdot \mathbf{l}] dA.$$

Thus, \mathbf{b}_r points in the slip direction \mathbf{s} . The scalar dislocation density, representing the number of excess dislocations per unit area, can then be calculated as

$$\rho = \frac{1}{b} |(\nabla \beta \times \mathbf{m}) \cdot \mathbf{l}|, \quad (4.10)$$

where b is the magnitude of the Burgers vector. Using (4.10) the free energy (4.6) may be expressed in the alternative form

$$\Psi = \Psi(\mathbf{C}^e, \rho).$$

Now, assume that the undeformed single crystal is defined as the set of material points $\mathcal{B} = \{\mathbf{X} | \mathbf{X} \in \bar{\mathcal{V}}\}$ in three-dimensional Euclidean space \mathcal{E} , using the notation introduced in Section 3.1. The boundary is comprised of material points forming the union $\partial \mathcal{V} = \partial_k \cup \partial_\tau$ of two nonintersecting portions of the surface. Prescribing a smooth displacement vector field $\mathbf{u}(\mathbf{X})$ at ∂_k leads to the boundary conditions

$$\mathbf{x}(\mathbf{X}) = \mathbf{X} + \mathbf{u}(\mathbf{X}), \quad \beta(\mathbf{X}) = 0 \quad \text{for } \mathbf{X} \in \partial_k, \quad (4.11)$$

i.e. the plastic slip $\beta(\mathbf{X})$ vanishes at this part of the crystal's surface. The displacement is defined according to (3.3) using (3.1). At ∂_τ there acts some 'dead' load $\boldsymbol{\tau}$, defined in Section 3.6. Neglecting body forces, the energy functional of the crystal specified above is defined by

$$I[\mathbf{x}(\mathbf{X}), \beta(\mathbf{X})] = \int_{\mathcal{V}} w(\mathbf{F}, \beta, \nabla \beta) dV - \int_{\partial_\tau} \boldsymbol{\tau} \cdot \mathbf{x} dA, \quad (4.12)$$

where

$$w(\mathbf{F}, \beta, \nabla \beta) = \Psi(\mathbf{C}^e, \rho).$$

Assume the resistance to dislocation motion is negligible and there are no surfaces of discontinuity inside the crystal. Then, for a single crystal with a single active slip system the following variational principle holds: among all admissible continuously differentiable functions $\mathbf{x}(\mathbf{X})$ and $\beta(\mathbf{X})$, subject to (4.11), the true deformation $\check{\mathbf{x}}(\mathbf{X})$ and the true plastic slip $\check{\beta}(\mathbf{X})$ in the

final equilibrium state of deformation minimize the energy functional (4.12). Provided the resistance to dislocation motion cannot be ignored, energy minimization must be performed using the below variational equation

$$\delta I + \int_{\mathcal{V}} \frac{\partial D}{\partial \dot{\beta}} \delta \beta \, dv = 0, \quad (4.13)$$

see Sedov (1965). The second term on the left-hand side of (4.13) accounts for the energy dissipation resulting from the motion of dislocations, where the rate of plastic slip is the only independent variable of the dissipation function $D = D(\dot{\beta})$, which for the simplest rate-independent model reads

$$D(\dot{\beta}) = K|\dot{\beta}|. \quad (4.14)$$

The parameter K in (4.14) may be interpreted as the critical resolved shear stress. Unless the sign of $\dot{\beta}$ changes, performing the variation in (4.13) corresponds to minimizing the below ‘relaxed’ energy functional

$$I_d[\mathbf{x}(\mathbf{X}), \beta(\mathbf{X})] = \int_{\mathcal{V}} \left[w(\mathbf{F}, \beta, \nabla \beta) + K \operatorname{sgn} \dot{\beta} \dot{\beta} \right] dV - \int_{\partial \tau} \boldsymbol{\tau} \cdot \mathbf{x} \, dA. \quad (4.15)$$

Thus, if there are no singular surfaces inside the crystal, (4.15) is the appropriate energy functional to be used to determine minimizers $\tilde{\mathbf{x}}(\mathbf{X})$ and $\tilde{\beta}(\mathbf{X})$, obeying boundary conditions (4.11). In case $\dot{\beta} = 0$, corresponding to a state of ‘frozen’ plastic slip, functional (4.12) is a suitable choice to find the minimizing displacements. In the limit of small displacements and plastic slip nonlinear CDT reduces to its linear counterpart, as developed in Berdichevsky (2006a) and references Berdichevsky and Le (2007); Le and Sembriring (2008a,b, 2009); Kochmann and Le (2008a,b, 2009); Kaluza and Le (2011); Le and Nguyen (2012, 2013).

4.1.2 Equilibrium Conditions for Crystals with Grain Boundaries

As discussed in Section 2.4, a bicrystal grain boundary in an SC crystal is defined as the interface between two grains of different orientation. The goal of the current Section is to provide a mathematical description of grain boundaries, consistent with the interpretation of kinematics peculiar to nonlinear CDT, as outlined in Subsection 4.1.1.

At first glance, it might be assumed that a grain boundary inside a single crystal causes a jump in the elastic deformation since the plastic deformation does not affect the crystal lattice. But, from physical reasoning the multiplicative decomposition of the deformation gradient must be taken into account, leading to possible jumps in the deformation gradient \mathbf{F} as well as the plastic slip $\beta(\mathbf{X})$. It is presumed that grain boundaries do not weaken the crystal at low temperatures so that there exists a continuous deformation function $\mathbf{x}(\mathbf{X})$ everywhere. Hence, some means comprising such characteristics is needed. This leads to the notion of the singular surface and the feature of compatibility, to be discussed in the following interlude in more detail, before moving on to the actual application.

Extra: Singular Surfaces and Rank-1 Connections. According to Romano et al. (2006) a singular surface inside some generic body may be defined as outlined next. Let the body \mathcal{V} in

its reference configuration be constituted by a compact domain with regular boundary $\partial\mathcal{V}$ in \mathcal{E} that contains a regular oriented surface \mathcal{S} with unit normal \mathbf{N} . The surface \mathcal{S} is such that it divides \mathcal{V} in two parts, denoted \mathcal{V}^+ and \mathcal{V}^- , and \mathbf{N} points in the \mathcal{V}^+ portion, as illustrated in Figure 4.2. Now, assume a function $\psi(P)$ of class $C^1(\mathcal{V} \setminus \mathcal{S})$. If the limits

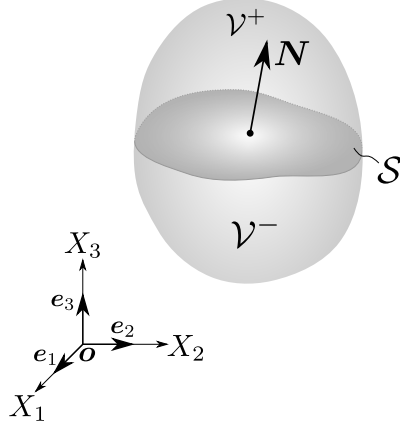


Figure 4.2: Singular surface \mathcal{S} deviding a generic body \mathcal{V} in portions \mathcal{V}^+ and \mathcal{V}^- .

$$\lim_{P \rightarrow \mathbf{r}, P \in \mathcal{V}^+} \psi(P) = \psi^+(\mathbf{r}), \quad \lim_{P \rightarrow \mathbf{r}, P \in \mathcal{V}^-} \psi(P) = \psi^-(\mathbf{r})$$

exist for all $\mathbf{r} \in \mathcal{S}$ and continuous functions $\psi^\pm(\mathbf{r})$ and the jump across the singular surface satisfies

$$[\![\psi(\mathbf{r})]\!] = \psi^+(\mathbf{r}) - \psi^-(\mathbf{r}) \neq 0$$

for some $\mathbf{r} \in \mathcal{S}$, then \mathcal{S} is referred to as a 0th-order singular surface for $\psi(P)$. Going one step further, presume

$$[\![\psi(\mathbf{r})]\!] = \psi^+(\mathbf{r}) - \psi^-(\mathbf{r}) = 0 \quad \text{on } \mathcal{S}.$$

If, in addition to that, there exist the limits

$$\lim_{P \rightarrow \mathbf{r}, P \in \mathcal{V}^+} \frac{\partial \psi}{\partial x_i}(P) = \left(\frac{\partial \psi}{\partial x_i} \right)^+(\mathbf{r}), \quad \lim_{P \rightarrow \mathbf{r}, P \in \mathcal{V}^-} \frac{\partial \psi}{\partial x_i}(P) = \left(\frac{\partial \psi}{\partial x_i} \right)^-(\mathbf{r}),$$

for $\left(\frac{\partial \psi}{\partial x_i} \right)^\pm(\mathbf{r})$ continuous at $\mathbf{r} \in \mathcal{S}$, then \mathcal{S} is a 1st-order singular surface for ψ , if

$$\left[\left[\frac{\partial \psi}{\partial x_i}(\mathbf{r}) \right] \right] = \left(\frac{\partial \psi}{\partial x_i} \right)^+(\mathbf{r}) - \left(\frac{\partial \psi}{\partial x_i} \right)^-(\mathbf{r}) \neq 0 \quad (4.16)$$

at some $\mathbf{r} \in \mathcal{S}$. Extending the above concept in the same spirit gives rise to the notion of the k th-order singular surface. It has to be noted that ψ is some generic scalar function here that may be interpreted as a component of some tensor field.

The following specifications of the surface of discontinuity and some notions closely related to it can be found in Šilhavý (1997). First, an important proposition, going by the name of the

Hadamard lemma, is introduced, making the above condition (4.16) for the jump of the gradient of ψ more precise by specifying that

$$\left[\left[\frac{\partial \psi}{\partial x_i} \right] \right] = C \mathbf{N} \quad (4.17)$$

holds. According to the Hadamard lemma relation (4.17) constitutes a kinematical compatibility condition, where the quantity C is a continuous scalar function on the singular surface, denoting the amplitude of the jump in the derivatives of function ψ .

To see the impact of the Hadamard lemma on the formulation of the problem at hand, the behavior of some generic deformation field across a surface of discontinuity is investigated in a finite-deformation setting. Thus, a suitable form of a singular surface associated with the deformation has to be identified. From physical reasoning it can be assumed that $\mathbf{x}(\mathbf{X})$ must be weakly discontinuous across \mathcal{S} , where the deformation itself is continuous everywhere inside the body, but its derivatives may exhibit discontinuities across some surface inside the body. Thus, the order of the surface of discontinuity must be 1 and can be defined as follows: for the deformation in the neighborhood of the singular surface there exist the limits

$$\lim_{\mathbf{X} \rightarrow \mathbf{r}, \mathbf{X} \in \mathcal{V}^+} \mathbf{x}(\mathbf{X}) = \mathbf{x}^+(\mathbf{r}), \quad \lim_{\mathbf{X} \rightarrow \mathbf{r}, \mathbf{X} \in \mathcal{V}^-} \mathbf{x}(\mathbf{X}) = \mathbf{x}^-(\mathbf{r})$$

for all $\mathbf{r} \in \mathcal{S}$. For the jump of $\mathbf{x}(\mathbf{X})$ the relation

$$[\![\mathbf{x}(\mathbf{r})]\!] = \mathbf{x}^+(\mathbf{r}) - \mathbf{x}^-(\mathbf{r}) = \mathbf{0}$$

holds and in addition to that the following limits

$$\lim_{\mathbf{X} \rightarrow \mathbf{r}, \mathbf{X} \in \mathcal{V}^+} \frac{\partial \mathbf{x}}{\partial \mathbf{X}}(\mathbf{X}) = \underbrace{\left(\frac{\partial \mathbf{x}}{\partial \mathbf{X}} \right)^+}_{\equiv \mathbf{F}^+(\mathbf{r})}(\mathbf{r}), \quad \lim_{\mathbf{X} \rightarrow \mathbf{r}, \mathbf{X} \in \mathcal{V}^-} \frac{\partial \mathbf{x}}{\partial \mathbf{X}}(\mathbf{X}) = \underbrace{\left(\frac{\partial \mathbf{x}}{\partial \mathbf{X}} \right)^-}_{\equiv \mathbf{F}^-(\mathbf{r})}(\mathbf{r}) \quad (4.18)$$

exist and

$$[\![\mathbf{F}(\mathbf{r})]\!] = \mathbf{F}^+(\mathbf{r}) - \mathbf{F}^-(\mathbf{r}) \neq \mathbf{0} \quad (4.19)$$

at some points $\mathbf{r} \in \mathcal{S}$. Then, applying (4.17) to the deformation and keeping in mind (4.18) and (4.19) gives the below form of the Hadamard lemma

$$[\![\mathbf{F}]\!] = \mathbf{q} \otimes \mathbf{N}, \quad (4.20)$$

where now the continuous vector-valued function \mathbf{q} denotes the amplitude of the jump, resulting from the fact that (4.19) takes into account the derivative of every single component of $\mathbf{x}(\mathbf{X})$. The compatibility condition (4.20) gives rise to the notion of rank-1 connections, to be treated next.

According to (4.20) the difference of the limit values of the deformation gradient, approaching the singular surface from the $+$ and $-$ sides, can be expressed as the dyadic product $\mathbf{q} \otimes \mathbf{N}$. Considering two tensors $\mathbf{F}, \mathbf{G} \in \mathbb{M}^n$, where \mathbb{M}^n denotes the linear space of all real square matrices of order n , are called rank-1 connected if $\mathbf{G} - \mathbf{F} = \mathbf{q} \otimes \mathbf{N}$ for $\mathbf{q}, \mathbf{N} \in V$, with V an n -dimensional real vector space with inner product. This may be formulated in an alternative way, where \mathbf{G} and \mathbf{F} are termed compatible and \mathbf{G} is called a rank-1 perturbation of \mathbf{F} .

A deformation of the generic body \mathcal{V} is called homogeneous if for the singular surface $\mathcal{S} = \emptyset$ holds and if the deformation gradient $\partial \mathbf{x} / \partial \mathbf{X}$ is constant over \mathcal{V} . What is more, if \mathcal{V} is connected there exists a $\mathbf{c} \in V$ such that $\mathbf{x}(\mathbf{p}) = \mathbf{F}\mathbf{p} + \mathbf{c}$ for all $\mathbf{p} \in \mathcal{V}$. For a body \mathcal{V} containing a singular surface \mathcal{S} the associated deformation field is termed pairwise homogeneous if the set $\{\mathbf{F}(\mathbf{p}) : \mathbf{p} \in \mathcal{V} \setminus \mathcal{S}\}$ is comprised of two elements \mathbf{F}^\pm . Considering a pairwise homogeneous deformation with $\llbracket \mathbf{F}(\mathbf{r}) \rrbracket \neq \mathbf{0}$ for all $\mathbf{r} \in \mathcal{S}$, the following relations hold. First,

$$\mathbf{F}^+ = \mathbf{F}^- + \mathbf{q} \otimes \mathbf{N},$$

where $\mathbf{q}, \mathbf{N} \in V$, $\mathbf{q} \neq \mathbf{0}$ and \mathbf{N} a unit vector. In addition to that, there is a countable family of parallel hyperplanes $H_i, i = 1, \dots$ such that

$$\mathcal{S} \subset \mathcal{V} \cap \bigcup_{i=1}^{\infty} H_i, \quad (4.21)$$

which is finite for \mathcal{V} bounded. Furthermore, if \mathcal{V} is convex, then

$$\mathbf{x}(\mathbf{p}) = \mathbf{F}^- \mathbf{p} + \mathbf{q} \theta(\mathbf{p} \cdot \mathbf{N}) + \mathbf{c}, \quad \mathbf{F}(\mathbf{p}) = \mathbf{F}^- + \mathbf{q} \otimes \mathbf{N} \theta'(\mathbf{p} \cdot \mathbf{N})$$

for a continuous and piecewise continuously differentiable map $\theta: \mathbb{R} \rightarrow \mathbb{R}$ and $\theta' \in \{0, 1\}$. If H_i are the surfaces of discontinuity of the map $\mathbf{p} \mapsto \theta'(\mathbf{p} \cdot \mathbf{N})$, equality holds in (4.21). This defines a deformation of parallel layers with associated constant deformation gradients, separated by planar surfaces. \triangle

The derivation of the features of the singular surface for the deformation and the resulting definition of rank-1 connections, as outlined before, hold in general and can be employed immediately in the computations to follow. What is still missing, but can be found quickly with the help of the definitions in the above interlude, is the appropriate formulation for $\beta(\mathbf{X})$ exhibiting strong discontinuity across the singular surface. Applying the definition of the 0th-order singular surface to the function of plastic slip, it follows that its behavior in the vicinity of \mathcal{S} is governed by

$$\lim_{\mathbf{X} \rightarrow \mathbf{r}, \mathbf{X} \in \mathcal{V}^+} \beta(\mathbf{X}) = \beta^+(\mathbf{r}), \quad \lim_{\mathbf{X} \rightarrow \mathbf{r}, \mathbf{X} \in \mathcal{V}^-} \beta(\mathbf{X}) = \beta^-(\mathbf{r})$$

for all $\mathbf{r} \in \mathcal{S}$, where $\beta(\mathbf{r})$ is continuous. Also, the jump across the singular surface satisfies

$$\llbracket \beta(\mathbf{r}) \rrbracket = \beta^+(\mathbf{r}) - \beta^-(\mathbf{r}) \neq 0$$

for some points $\mathbf{r} \in \mathcal{S}$.

To model the formation of grain boundaries in the framework of nonlinear CDT the variational principles stated in the previous Subsection 4.1.1 need to be enhanced by an energy contribution due to the existence of such boundaries in the crystal. According to the above definition of a grain boundary the minimizers of the modified energy functional must be from a set of functions admitting weak discontinuity in $\mathbf{x}(\mathbf{X})$ and strong discontinuity in $\beta(\mathbf{X})$ across the singular surface. In what follows, it is presumed that the boundary of this surface \mathcal{S} is a fixed curve that coincides with a curve on the outer surface $\partial \mathcal{V}$ of the crystal.

Adding an energy contribution for the grain boundary to (4.12) and performing integration of the volume integral over $\mathcal{V} \setminus \mathcal{S}$, thus excluding \mathcal{S} , gives

$$I[\mathbf{x}(\mathbf{X}), \beta(\mathbf{X})] = \int_{\mathcal{V} \setminus \mathcal{S}} w(\mathbf{F}, \beta, \nabla \beta) \, dV + \int_{\mathcal{S}} \zeta \, dA - \int_{\partial \tau} \boldsymbol{\tau} \cdot \mathbf{x} \, dA, \quad (4.22)$$

where in the second term on the right-hand side ζ corresponds to the energy per unit area of the grain boundary. Assume ζ to be constant, justified if the angle of misorientation, as defined in Chapter 2, is not less than 15° . The variational principle formulated in the previous Section then must be rephrased: among all functions admitting weak discontinuity in $\mathbf{x}(\mathbf{X})$ and strong discontinuity in $\beta(\mathbf{X})$ across the surface \mathcal{S} , as specified above, the true deformation $\tilde{\mathbf{x}}(\mathbf{X})$ and the true plastic slip $\tilde{\beta}(\mathbf{X})$ in the final equilibrium state of deformation minimize the energy functional (4.22), subject to (4.11).

To perform the actual variation, the crystal's energy must be investigated in the neighborhood of some deformed configuration, similar to the situation shown in Figure 3.9 in Section 3.6, illustrating the virtual displacement of a generic body \mathcal{B} deforming purely elastically. Introducing a one-parameter family of deformations $\mathbf{x}(\mathbf{X}, \epsilon)$ and plastic slip $\beta(\mathbf{X}, \epsilon)$, the minimizers must satisfy $\mathbf{x}(\mathbf{X}, 0) = \tilde{\mathbf{x}}(\mathbf{X})$ and $\beta(\mathbf{X}, 0) = \tilde{\beta}(\mathbf{X})$. In addition to that, the surface of discontinuity is unknown and therefore must be obtained from an admissible set \mathcal{S}_ϵ to give the true surface $\tilde{\mathcal{S}}$ by variation. The associated energy functional reads

$$I[\mathbf{x}(\mathbf{X}, \epsilon), \beta(\mathbf{X}, \epsilon)] = \int_{\mathcal{V}_\epsilon^+} w(\mathbf{F}, \beta, \nabla \beta) dV + \int_{\mathcal{V}_\epsilon^-} w(\mathbf{F}, \beta, \nabla \beta) dV + \int_{\mathcal{S}_\epsilon} \zeta dA - \int_{\partial \tau} \boldsymbol{\tau} \cdot \mathbf{x} dA. \quad (4.23)$$

Using the concept of the directional derivative, introduced in (3.68), the variation of the family of admissible functions can be computed according to

$$\delta I = \left. \frac{d}{d\epsilon} I[\mathbf{x}(\mathbf{X}, \epsilon), \beta(\mathbf{X}, \epsilon)] \right|_{\epsilon=0}. \quad (4.24)$$

Interpreting $I[\mathbf{x}(\mathbf{X}, \epsilon), \beta(\mathbf{X}, \epsilon)]$ as a function of the single scalar variable ϵ , it attains its minimum value at $\epsilon = 0$, as required before, and the first variation must be equal to zero, i.e.

$$\delta I = 0, \quad (4.25)$$

see also MacCluer (2005); Weinstock (1974). To actually compute the variation in (4.25) it has to be noted that the regions of integration \mathcal{V}_ϵ^\pm as well as the singular surfaces \mathcal{S}_ϵ depend on ϵ , which renders the process of variation complicated. To overcome this issue a one-parameter family of smooth and injective mappings $\mathbf{z}(\mathbf{X}, \epsilon)$ of \mathcal{V} into itself, defined by

$$\check{\mathcal{V}}^+ \xrightarrow{\mathbf{z}} \mathcal{V}_\epsilon^+, \quad \check{\mathcal{V}}^- \xrightarrow{\mathbf{z}} \mathcal{V}_\epsilon^-, \quad \check{\mathcal{S}} \xrightarrow{\mathbf{z}} \mathcal{S}_\epsilon, \text{ where} \\ \mathbf{z}(\mathbf{X}, \epsilon) = \mathbf{X}, \text{ if } \epsilon = 0 \text{ or if } \mathbf{X} \in \partial \mathcal{V},$$

is introduced, see e.g. Le (2010). Using these mappings the regions of integration \mathcal{V}_ϵ^\pm and \mathcal{S}_ϵ in (4.23) are transformed to $\check{\mathcal{V}}^\pm$ and $\check{\mathcal{S}}^\pm$, respectively, independent of ϵ . Thus, now differentiation with respect to ϵ may be performed, not affecting the domains of integration. Employing index notation, the first variation of the first term on the right-hand side of (4.23) reads

$$\begin{aligned} \delta \int_{\mathcal{V}_\epsilon^+} w(x_{i,a}, \beta, \beta_{,a}) dV &= \delta \int_{\check{\mathcal{V}}^+} w\left(\frac{\partial x_i}{\partial z_a}, \beta, \frac{\partial \beta}{\partial z_a}\right) \det z_{a,b} dV \\ &= \int_{\check{\mathcal{V}}^+} \left[\delta w\left(\frac{\partial x_i}{\partial z_a}, \beta, \frac{\partial \beta}{\partial z_a}\right) + w \delta \det z_{a,b} \right] dV \\ &= \int_{\check{\mathcal{V}}^+} \left(P_{ia} \delta \frac{\partial x_i}{\partial z_a} + \frac{\partial w}{\partial \beta} \delta \beta + \frac{\partial w}{\partial \beta_{,a}} \delta \frac{\partial \beta}{\partial z_a} + w \delta z_{a,a} \right) dV, \end{aligned}$$

where $\mathbf{P} = \partial w / \partial \mathbf{F}$ is the first Piola-Kirchhoff stress, as encountered in the purely elastic setting in Section 3.3, and identity $\delta \det z_{a,b} = \delta z_{a,a}$ has been used. In accordance with (4.24) the variational operator δ implies partial differentiation with respect to ϵ and subsequent evaluation of the derivative at $\epsilon = 0$, while keeping \mathbf{X} constant. Applying the chain rule it can be found that

$$\frac{\partial x_i}{\partial X_b} = \frac{\partial x_i}{\partial z_a} \frac{\partial z_a}{\partial X_b}, \quad \frac{\partial \beta}{\partial X_b} = \frac{\partial \beta}{\partial z_a} \frac{\partial z_a}{\partial X_b}$$

and then

$$\delta \frac{\partial x_i}{\partial z_a} = \delta x_{i,a} - x_{i,b} \delta z_{b,a}, \quad \delta \frac{\partial \beta}{\partial z_a} = \delta \beta_{,a} - \beta_{,b} \delta z_{b,a},$$

by the product rule. Plugging the above results into the expression obtained for the first variation gives

$$\delta \int_{\mathcal{V}_\epsilon^+} w(x_{i,a}, \beta, \beta_{,a}) dV = \int_{\mathcal{V}^+} \left(P_{ia} \delta x_{i,a} + \frac{\partial w}{\partial \beta} \delta \beta + \frac{\partial w}{\partial \beta_{,a}} \delta \beta_{,a} + \mu_{ab} \delta z_{a,b} \right) dV, \quad (4.26)$$

with the generalized Eshelby tensor

$$\mu_{ab} = -x_{i,a} P_{ib} - \beta_{,a} \frac{\partial w}{\partial \beta_{,b}} + w \delta_{ab}$$

and δ_{ab} denoting the Kronecker delta. To get the first variation of the second term on the right-hand side of (4.23) the same procedure as outlined before applies. The first variation of the surface integrals reads

$$\delta \int_{\mathcal{S}_\epsilon} \zeta dA = - \int_{\mathcal{S}} 2\zeta \eta N_a \delta z_a dA, \quad \delta \int_{\partial_\tau} \tau_i x_i dA = \int_{\partial_\tau} \tau_i \delta x_i dA, \quad (4.27)$$

where η refers to the mean curvature of the minimizing surface $\check{\mathcal{S}}$. Applying integration by parts to (4.26) and the corresponding expression related to region \mathcal{V}^- , subsequently making use of the divergence theorem and considering result (4.27) as well as (4.11) yields

$$\begin{aligned} \delta I = & \int_{\mathcal{V} \setminus \check{\mathcal{S}}} \left\{ -P_{ia,a} \delta x_i + \left[w_\beta - (w_{\beta,a})_{,a} \right] \delta \beta - \mu_{ab,b} \delta z_a \right\} dV \\ & - \int_{\check{\mathcal{S}}} \left\{ \llbracket P_{ia} \rrbracket N_a \delta x_i + w_{\beta,a}^+ N_a \delta \beta^+ - w_{\beta,a}^- N_a \delta \beta^- + (\llbracket \mu_{ab} \rrbracket N_b + 2\zeta \eta N_a) \delta z_a \right\} dA \\ & + \int_{\partial_\tau} \left[(P_{ia} N_a - \tau_i) \delta x_i + w_{\beta,a} N_a \delta \beta \right] dA = 0. \end{aligned} \quad (4.28)$$

In virtue of the discussion in Section 3.6 it may be deduced from (4.28) that the following equilibrium equations

$$\mathbf{P} \cdot \nabla = \mathbf{0}, \quad w_\beta - \nabla \cdot w_{\nabla \beta} = 0, \quad \boldsymbol{\mu} \cdot \nabla = 0 \quad (4.29)$$

must hold for the minimizers in region $\mathcal{V} \setminus \check{\mathcal{S}}$, obeying the kinematic boundary conditions (4.11) and the natural boundary conditions

$$\mathbf{P} \mathbf{N} = \boldsymbol{\tau}, \quad w_{\nabla \beta} \cdot \mathbf{N} = 0 \quad \text{at } \partial_\tau.$$

In (4.29) $w_\beta = -\tau_r$ defines the resolved shear stress or Schmid stress. In contrast to conventional theories of crystal plasticity the back stress $\varsigma = \nabla \cdot w_{\nabla\beta}$ has been obtained as a natural consequence of the variational process. Equation (4.29)₁ defines the equilibrium of macro-forces acting on the crystal, whereas (4.29)₂ can be interpreted as the equilibrium of micro-forces exerted on dislocations. It can be found that (4.29)₃ does not provide additional information and is satisfied automatically if (4.29)_{1,2} hold. As variations $\delta\mathbf{x}$, $\delta\beta^\pm$ and $\delta\mathbf{z}$ are arbitrary on $\check{\mathcal{S}}$ the jump conditions

$$[[\mathbf{P}]]\mathbf{N} = \mathbf{0}, \quad w_{\nabla\beta} \cdot \mathbf{N} = 0, \quad [[\boldsymbol{\mu}]]\mathbf{N} + 2\zeta\eta\mathbf{N} = \mathbf{0} \quad (4.30)$$

across the surface of discontinuity must be satisfied, too. Equation (4.30)₂ has to be satisfied on both sides of $\check{\mathcal{S}}$, where strong discontinuity in $\beta(\mathbf{X})$ holds. Since (4.20) and (4.30)_{1,2} apply on $\check{\mathcal{S}}$, (4.30)₃ can be expressed as

$$[[\boldsymbol{\mu}]]\mathbf{N} + 2\zeta\eta\mathbf{N} = -[[\mathbf{F}^T]]\mathbf{P}\mathbf{N} + [[w]]\mathbf{N} + 2\zeta\eta\mathbf{N} = \mathbf{N}(-\mathbf{q} \cdot \mathbf{P}\mathbf{N} + [[w]] + 2\zeta\eta),$$

where \mathbf{P} may lie on either side of $\check{\mathcal{S}}$. Multiplying the above result by \mathbf{N} gives the below independent scalar equation

$$f = -\mathbf{q} \cdot \mathbf{P}\mathbf{N} + [[w]] + 2\zeta\eta = 0, \quad (4.31)$$

which constitutes a thermodynamic equilibrium equation saying that the thermodynamic driving force exerted on the grain boundary must vanish so that the grain boundary remains at a fixed position.

The constitutive equations can be obtained by analogy with the general hyperelastic formulation (3.52), i.e. as partial derivatives of the free energy density. Hence, the first Piola-Kirchhoff stress reads

$$\mathbf{P} = w_{\mathbf{F}} = 2\mathbf{F}^e \Psi_{\mathbf{C}^e} \mathbf{F}^{p-T}. \quad (4.32)$$

The resolved shear stress is given by

$$\tau_r = -w_\beta = -\mathbf{s} \cdot \mathbf{F}^{eT} \mathbf{P} \mathbf{m} \quad (4.33)$$

and the back stress can be expressed as

$$\varsigma = \nabla \cdot w_{\nabla\beta} = \frac{1}{b} \operatorname{sgn}[(\nabla\beta \times \mathbf{m}) \cdot \mathbf{l}] \mathbf{l} \cdot \nabla(\Psi_\rho) \times \mathbf{m}. \quad (4.34)$$

Plugging the above constitutive laws (4.32) to (4.34) in equations (4.29) to (4.30) yields a closed system of equations and boundary conditions. Then, supplementing this set of equations with condition (4.20) allows for the determination of minimizers $\check{\mathbf{x}}(\mathbf{X})$, $\check{\beta}(\mathbf{X})$ and $\check{\mathcal{S}}$.

4.1.3 Energy Formulation and Constitutive Equations

In Koster, Le and Nguyen (2015) the free energy per unit volume of the undeformed crystal was proposed as a Saint-Venant Kirchhoff (SVK) energy with two additional terms, one for the energy to satisfy the growth condition (3.56), the other one representing the energy contribution of the dislocation network. Before turning to computations the general SVK model needs to be discussed in more detail, where the below properties can be found in Ciarlet (1988).

First, it has to be noted that it is the simplest hyperelastic model whose response function can be expressed in terms of the Green-Lagrange strain as

$$\mathfrak{G}(\mathbf{E}) = \lambda (\text{tr} \mathbf{E}) \mathbf{I} + 2\mu \mathbf{E} + o(\mathbf{E}), \quad (4.35)$$

introducing the Lamé constants λ and μ . The ‘little oh’ o notation used in (4.35) denotes the Landau order symbol and means that

$$o(\mathbf{E}) = \mathfrak{G}(\mathbf{E}) - \lambda (\text{tr} \mathbf{E}) \mathbf{I} - 2\mu \mathbf{E}$$

approaches zero faster than $\mathbf{E} \rightarrow \mathbf{0}$, see e.g. Gonzalez and Stuart (2008); Holzapfel (2000). This is expressed in mathematical terms as

$$\lim_{\mathbf{E} \rightarrow \mathbf{0}} \frac{o(\mathbf{E})}{\|\mathbf{E}\|} = \mathbf{0},$$

where $\|\mathbf{E}\|$ is the standard Euclidean norm. It can be found that relation (4.35) is invertible for $\mu(3\lambda + 2\mu) \neq 0$, but it turns out that there exist cases where large strains may occur in connection with small stresses, see Antman (1979); Truesdell (1978), which is not in agreement with a linear stress–strain relation. In addition to that, the standard SVK model does not reflect the behavior implied by the growth condition (3.56), a serious deficiency which has been removed in Koster, Le and Nguyen (2015), as stated before.

Since the notion of convexity of strain-energy functions is important for the existence of minimizers, convexity features of functions and their implications are discussed in the following ‘Extra’ Section. It is shown that convexity is a property that cannot be satisfied by strain-energy functions and that there exists a more reasonable requirement, called polyconvexity. There is an outline of the construction of general polyconvex energy functions in hyperelasticity, eventually leading to a practical way to check for polyconvexity.

Extra: Notions of Convexity. There exist various interrelated notions of convexity, two of which are of particular interest in this thesis. Convexity properties rule the behavior of functions. Strain-energy functions on the one hand must represent the physics underlying the type of material they are supposed to model, on the other hand the existence of solutions must be ensured. It has been found that convexity is not a useful assumption, whereas polyconvexity is a desirable feature in the context of strain-energy functions, see e.g. Ciarlet (1988); Marsden and Hughes (1994). Thus, the notions of convexity and polyconvexity are introduced in what follows. The discussion is mainly based on the ideas presented in Ciarlet (1988), where the essential theorems are given without any proofs. For a detailed account of the various aspects of convexity and the corresponding derivations and proofs see Dacorogna (2008). A treatment related to the description of crystal microstructures is given in Dolzmann (2003).

To start the presentation, a short discussion on how the terms convexity, convex hull and lower convex hull apply to sets and functions is given. A simple geometric interpretation of a convex set, defined as a subset U of a vector space V , is that for any two arbitrary points, denoted $u, v \in U$, respectively, the closed segment $[u, v]$ is also contained in this set. What is more, if U is a convex subset of a normed vector space, then its closure \overline{U} and interior $\text{int } U$ are convex, too.

The convex hull of a nonempty subset U of a vector space V , denoted $\text{co } U$, is defined as the intersection of all convex subsets of V containing U . In the field of elasticity there

exist two important examples of convex hulls of sets. Starting with the definition $\mathbb{M}_+^3 = \{\mathbf{F} \in \mathbb{M}^3; \det \mathbf{F} > 0\}$, being the set of all real square matrices of order 3 with positive determinant, it can be shown that

$$\text{co } \mathbb{M}_+^3 = \mathbb{M}^3, \quad (4.36)$$

$$\text{co } \{(\mathbf{F}, \text{Cof } \mathbf{F}, \det \mathbf{F}) \in \mathbb{M}^3 \times \mathbb{M}^3 \times \mathbb{R}; \mathbf{F} \in \mathbb{M}_+^3\} = \mathbb{M}^3 \times \mathbb{M}^3 \times]0, +\infty[, \quad (4.37)$$

where the nonconvexity of the set \mathbb{M}_+^3 can be deduced from (4.36), immediately.

The point of departure for the discussion of the lower convex hull is the definition of convexity of a function $J: U \subset V \rightarrow \mathbb{R}$, where the domain of definition is a convex subset U of a vector space V , expressed through

$$\begin{aligned} u, v \in U \text{ and } \theta \in [0, 1] \\ \Rightarrow J(\theta u + (1 - \theta)v) \leq \theta J(u) + (1 - \theta)J(v) \end{aligned} \quad (4.38)$$

and

$$\begin{aligned} u, v \in U, u \neq v \text{ and } \theta \in]0, 1[\\ \Rightarrow J(\theta u + (1 - \theta)v) < \theta J(u) + (1 - \theta)J(v), \end{aligned} \quad (4.39)$$

where (4.38) corresponds to the criterion to be satisfied for J to be convex and (4.39) specifies strict convexity. The geometric interpretation is that the secant line connecting any two points $(u, J(u))$ and $(v, J(v))$ on the graph is always above or on the graph of the function, as shown in Figure 4.3. Actually, condition (4.38) constitutes a special case of the relation

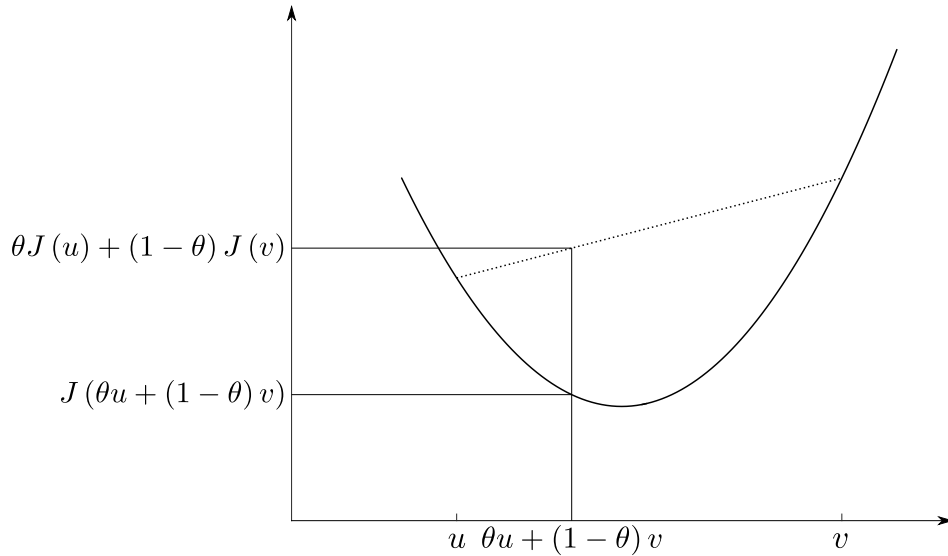


Figure 4.3: Geometric interpretation of convexity in terms of the secant line to a generic function J .

$$J(u) \leq \sum_{i=1}^s \theta_i J(u_i), \quad (4.40)$$

where, introducing the convex combination $\sum_{i=1}^s \theta_i u_i = u$ with $\sum_{i=1}^s \theta_i = 1$, J is convex if $u_i \in U$, $\theta_i \geq 0$ and $J(\theta u_i) < \infty$ hold for all $i = 1, \dots, s$. Then, u is called a point of convexity. Strict convexity is defined in the same spirit as in (4.39), see Šilhavý (1997).

What is of particular importance to the computations to follow later in this Section is the concept of the lower convex hull of functions, as introduced in Šilhavý (1997). Assuming now a function $J: U \subset V \rightarrow \{-\infty\} \cup \mathbb{R} \cup \{\infty\}$, where the codomain consists of the extended real numbers, then there exists a unique convex function $J^{\text{co}}: V \rightarrow \{-\infty\} \cup \mathbb{R} \cup \{\infty\}$ such that

$$J^{\text{co}} \leq J \quad \text{on } U \quad (4.41)$$

and if $G: V \rightarrow \{-\infty\} \cup \mathbb{R} \cup \{\infty\}$ is a convex function with $G \leq J$ on U , then

$$G \leq J^{\text{co}} \quad \text{on } V.$$

To further specify the nature of the function J^{co} it has to be noted that

$$J^{\text{co}} = \infty \quad \text{on } V \setminus \text{co } U.$$

Also, if $u \in U$ constitutes a point of convexity of J , then

$$J^{\text{co}}(u) = J(u).$$

In addition to that, if $J < \infty$ on U , then

$$J^{\text{co}} < \infty \quad \text{on } \text{co } U.$$

And eventually, if there exists an affine lower bound for J , defined by $J(u) \geq c \cdot u + b$ for all $u \in V$, some $b \in \mathbb{R}$ and $c \in V$, then

$$J^{\text{co}}(u) \geq c \cdot u + b$$

and therefore $J^{\text{co}} > -\infty$ on V .

When the above properties hold, J^{co} is called the lower convex hull of the function J and defines the largest convex function that minorizes J . The outline for the construction of such a function is as follows: since J^{co} is assumed convex, (4.40) is true for J^{co} at every $u \in V$. For the points $u_i \in U$ (4.41) implies that $J^{\text{co}}(u) \leq \sum_{i=1}^s \theta_i J(u_i)$, where the right-hand side must hold for all combinations of θ_i and u_i of u . From that the lower convex hull of J may be defined as the infimum of all of the right-hand side's possible representations, where for $u \notin \text{co } U$ the infimum is taken with respect to the empty set, thus being infinite. It can be found that it is appropriate to consider just representations with up to $n + 1$ points of U , with n corresponding to $\dim V$. Then, presuming $J(u_i) < \infty$ gives

$$J^{\text{co}}(u) = \inf \left\{ \sum_{i=1}^{n+1} \beta_i J(u_i) : \sum_{i=1}^{n+1} \beta_i u_i = u, \sum_{i=1}^{n+1} \beta_i = 1, \beta_i \geq 0, J(u_i) < \infty, u_i \in U \right\}.$$

From this it can be seen that if u is a point of convexity, then $J^{\text{co}}(u) = J(u)$. For the case of a scalar function of one scalar variable the above infimum is given as

$$J^{\text{co}}(u) = \inf \{ \beta_A J(u_A) + \beta_B J(u_B) : \beta_A u_A + \beta_B u_B = u, \beta_A + \beta_B = 1, \beta_{A,B} \geq 0, J(u_{A,B}) < \infty, u_{A,B} \in \mathbb{R} \},$$

which corresponds to the tangent line to J , passing through points $(u_{A,B}, J(u_{A,B}))$. An illustration of this specific case is provided in the below Figure 4.4. A plot of the derivatives

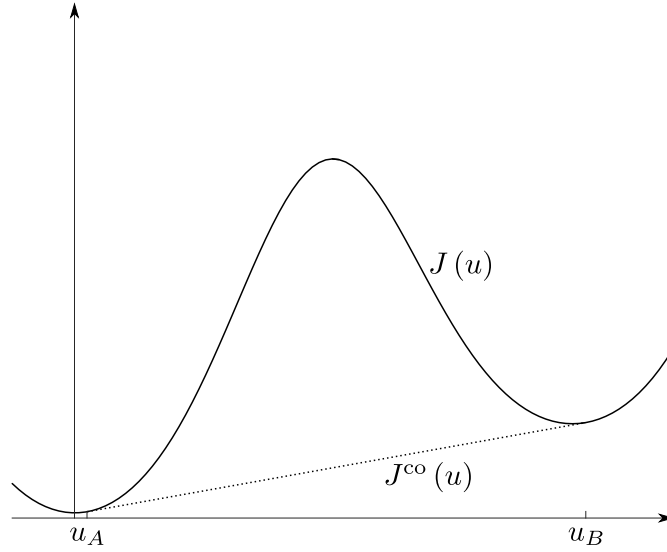


Figure 4.4: Geometric interpretation of the lower convex hull $J^{\text{co}}(u)$ as the tangent line to the nonconvex function $J(u)$, intersecting points $(u_{A,B}, J(u_{A,B}))$.

of functions J and J^{co} is shown in Figure 4.5, revealing an important relation between functions $J'(u)$ and $[J^{\text{co}}(u)]'$, going by the name of Maxwell's construction, see Le (2010); Šilhavý (1997), i.e. the constant function $[J^{\text{co}}(u)]' = m$ intersects $J'(u)$ three times and thus creates two equally sized areas enclosed by the two functions. This is a vital observation that can be used in the practical construction of lower convex hulls.

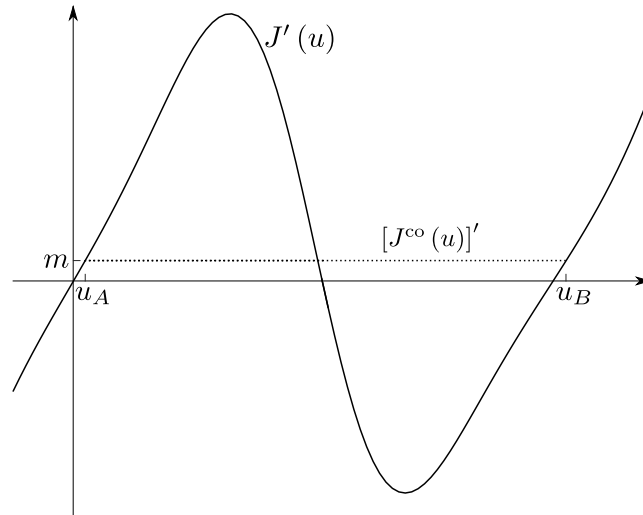


Figure 4.5: Maxwell's rule of equal areas.

Next, alternative conditions for the convexity of functions related to function minimization are introduced. For a function J , defined on an open set containing a local minimum u , the necessary condition $J'(u) = 0$ can be extended to the case, where the domain of definition of J is a convex set. This leads to the so-called Euler inequalities, defined as follows: assume a function $J: U \rightarrow \mathbb{R}$ with U being a subset of a normed vector space, as encountered above. If

J attains a local minimum at $u \in U$ and if the derivative of J at u exists, then

$$J'(u)(v - u) \geq 0 \quad \text{for all } v \in U.$$

Now, relations between convexity and derivatives can be established. The domain of definition of the generic function $J: U \rightarrow \mathbb{R}$ under investigation is a convex subset of a normed vector space, where it is assumed that J is differentiable on U . The function J is said to be convex or strictly convex if and only if

$$J(v) \geq J(u) + J'(u)(v - u) \quad \text{for all } u, v \in U$$

and if and only if

$$J(v) > J(u) + J'(u)(v - u) \quad \text{for all } u, v \in U, u \neq v$$

hold, respectively. Geometrically, the above conditions mean that a convex function always lies above its tangent plane, illustrated in Figure 4.6. Yet another definition of convexity is available

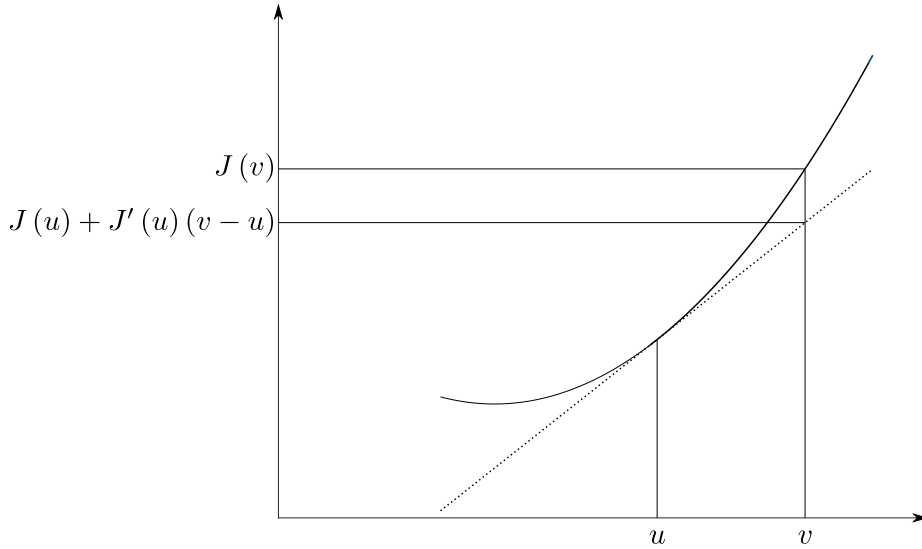


Figure 4.6: Geometric interpretation of convexity in terms of the tangent plane to a generic function J , adapted from Ciarlet (1988).

assuming a twice differentiable function $J: U \rightarrow \mathbb{R}$, which is convex if and only if

$$J''(u)(v - u, v - u) \geq 0 \quad \text{for all } u, v \in U \quad (4.42)$$

and strictly convex if

$$J''(u)(v - u, v - u) > 0 \quad \text{for all } u, v \in U, u \neq v.$$

The notation $J''(a)(h, k)$ denotes the Gâteaux derivative of the mapping $x \in \Omega \subset X \rightarrow J'(x)k \in Y$ at $x = a \in \Omega$ in the direction of h , with X and Y normed vector spaces, and $J'(a)h$ is to be understood as the inner product $(\text{Grad } J(a), h)$ for all $h \in X$.

So far, convexity of functions defined on convex sets has been treated. An extension, needed in the following paragraphs, is the investigation of convexity of functions, where the domain of definition is not necessarily convex. Assume an arbitrary nonempty subset of V and its

corresponding convex hull, denoted U and $\text{co } U$, respectively. Then, a mapping $J^*: U \rightarrow \mathbb{R}$ is convex if there exists a convex function $J: \text{co } U \rightarrow \mathbb{R}$ for which $J^*(v) = J(v)$ holds for all $v \in U$.

The central question of the current discussion is if it is possible to find convex functions that qualify as candidates for strain-energy functions from a mathematical as well as physical point of view. To see that, it is presumed that there exists a convex strain-energy function

$$\hat{W}(\mathbf{X}, \bullet) : \mathbf{F} \in \mathbb{M}_+^3 \rightarrow \hat{W}(\mathbf{X}, \mathbf{F}) \in \mathbb{R}$$

where $\mathbf{X} \in \bar{\Omega}$ denote material coordinates and \mathbf{F} is interpreted as the deformation gradient, as introduced in Chapter 3. It can be found that this kind of situation is not in agreement with the growth condition (3.56). This immediately prevents the case of convex strain-energy functions explicitly depending on $\det \mathbf{F}$. In addition to that, from the principle of material objectivity of the Cauchy stress tensor, discussed in Section 3.4, it can be deduced that for any deformation of a body the eigenvalues λ_i of the Cauchy stress must fulfill the inequalities

$$\lambda_i + \lambda_{i+1} \geq 0 \quad (4.43)$$

for all points in the current configuration, see Coleman and Noll (1959); Truesdell and Noll (2004). It turns out that (4.43) cannot be satisfied in situations of uniform pressure, see the example of a spherical body under uniform compression in Ciarlet (1988).

As stated before, convexity is not a desired feature of strain-energy functions since the mathematics associated with it does not reflect the physical properties of real materials. The notion of polyconvexity, introduced in Ball (1977), imposing weaker requirements on energy functions that agree with physical principles, constitutes a suitable criterion when developing strain-energy functions.

In Ball (1977) it is assumed that a function $\hat{W}: \mathbb{F} \rightarrow \mathbb{R}$, defined on an arbitrary $\mathbb{F} \subset \mathbb{M}^3$, is polyconvex if there exists a convex mapping $\mathbb{W}^*: \mathbb{U} \rightarrow \mathbb{R}$, with \mathbb{U} defined by

$$\mathbb{U} := \{(\mathbf{F}, \text{Cof } \mathbf{F}, \det \mathbf{F}) \in \mathbb{M}^3 \times \mathbb{M}^3 \times \mathbb{R}; \mathbf{F} \in \mathbb{F}\}$$

and

$$\hat{W}(\mathbf{F}) = \mathbb{W}^*(\mathbf{F}, \text{Cof } \mathbf{F}, \det \mathbf{F}) \quad \text{for all } \mathbf{F} \in \mathbb{F}.$$

An alternative definition is as follows: a function $\hat{W}: \mathbb{F} \rightarrow \mathbb{R}$ is polyconvex if there exists a convex mapping $\mathbb{W}: \text{co } \mathbb{U} \rightarrow \mathbb{R}$ with

$$\hat{W}(\mathbf{F}) = \mathbb{W}(\mathbf{F}, \text{Cof } \mathbf{F}, \det \mathbf{F}) \quad \text{for all } \mathbf{F} \in \mathbb{F}.$$

Hence, in virtue of (4.37), a function $\hat{W}: \bar{\Omega} \times \mathbb{M}_+^3 \rightarrow \mathbb{R}$, given as

$$\hat{W}(\mathbf{X}, \mathbf{F}) = \mathbb{W}(\mathbf{X}, \mathbf{F}, \text{Cof } \mathbf{F}, \det \mathbf{F}) \quad \text{for all } \mathbf{F} \in \mathbb{M}_+^3 \quad (4.44)$$

is polyconvex if there exists a convex function

$$\mathbb{W}(\mathbf{X}, \bullet) : \mathbb{M}^3 \times \mathbb{M}^3 \times]0, +\infty[\rightarrow \mathbb{R}$$

for each $\mathbf{X} \in \bar{\Omega}$.

In what follows, concepts in the construction of polyconvex strain-energy functions and criteria to check for polyconvexity of energy functions are discussed. To see what (4.44) actually means when considering specific examples, check out the function

$$\hat{W}: \mathbf{F} \in \mathbb{M}_+^3 \rightarrow \hat{W}(\mathbf{F}) = \text{tr Cof } \mathbf{F}^T \mathbf{F} = \|\text{Cof } \mathbf{F}\|^2 \quad (4.45)$$

and matrices

$$\mathbf{F}_\lambda = \lambda \text{Diag}(2, 1, 1) + (1 - \lambda) \text{Diag}(1, 2, 1) \in \mathbb{M}_+^3, \quad 0 \leq \lambda \leq 1, \quad (4.46)$$

where the notation $\text{Diag}(a, b, c) := a \mathbf{i} \otimes \mathbf{i} + b \mathbf{j} \otimes \mathbf{j} + c \mathbf{k} \otimes \mathbf{k}$, employing the standard Cartesian basis vectors \mathbf{i} , \mathbf{j} and \mathbf{k} , is used for diagonal matrices. Plugging (4.46) in (4.45) gives the explicit expression

$$\lambda \in [0, 1] \rightarrow \text{tr Cof } \mathbf{F}_\lambda^T \mathbf{F}_\lambda = 9 + 2\lambda - \lambda^2 - 2\lambda^3 + \lambda^4.$$

It can be found that the above function (4.45) is not convex in general and specifically in the neighborhood of 0 for the given matrices \mathbf{F}_λ . But, convexity of the below function

$$\mathbb{W}: \mathbf{H} \in \mathbb{M}^3 \rightarrow \mathbb{W}(\mathbf{H}) = \text{tr } \mathbf{H}^T \mathbf{H} = \|\mathbf{H}\|^2$$

renders \hat{W} polyconvex, where $\mathbb{W}''(\mathbf{H})(\mathbf{G}, \mathbf{G}) = \frac{\partial}{\partial \mathbf{H}} \left(\frac{\partial \mathbb{W}}{\partial \mathbf{H}} : \mathbf{G} \right) : \mathbf{G} = 2 \|\mathbf{G}\|^2 \geq 0$ for all $\mathbf{H}, \mathbf{G} \in \mathbb{M}^3$, in agreement with (4.42). Another example of a polyconvex function is

$$\hat{W}: \mathbf{F} \in \mathbb{M}_+^3 \rightarrow \hat{W}(\mathbf{F}) = \det \mathbf{F}. \quad (4.47)$$

Again, the function (4.47) is nonconvex in general and in the special case

$$\lambda \in [0, 1] \rightarrow \det \mathbf{F}_\lambda = 2 + \lambda - \lambda^2,$$

using (4.46), again. Polyconvexity of (4.47) can be inferred from the fact that $\mathbb{W}(\delta) = \delta$ is convex.

From the above results it is deduced that a polyconvex energy function can be constructed in the form

$$\hat{W}: \mathbf{F} \in \mathbb{M}_+^3 \rightarrow \hat{W}(\mathbf{F}) = a \|\mathbf{F}\|^2 + b \|\text{Cof } \mathbf{F}\|^2 + \Gamma(\det \mathbf{F}),$$

where constants $a, b > 0$ and function $\Gamma:]0, +\infty[\rightarrow \mathbb{R}$ is convex, as

$$\mathbb{W}(\mathbf{X}, \mathbf{F}, \mathbf{H}, \delta) = a \|\mathbf{F}\|^2 + b \|\mathbf{H}\|^2 + \Gamma(\delta)$$

is a convex function on $\mathbb{M}^3 \times \mathbb{M}^3 \times]0, +\infty[$. To introduce a more general form of polyconvex functions, a criterion for convexity of functions of matrix arguments is given first. Assume a symmetric and convex function $\Phi: [0, +\infty[^n \rightarrow \mathbb{R}$ which is nondecreasing in all of its arguments. According to Thompson and Freede (1971) this renders function

$$W: \mathbf{F} \in \mathbb{M}^n \rightarrow W(\mathbf{F}) = \Phi(v_1(\mathbf{F}), v_2(\mathbf{F}), \dots, v_n(\mathbf{F}))$$

convex, where $v_i = v_i(\mathbf{F}) := \left\{ \lambda_i^{\mathbf{F}^T \mathbf{F}} \right\}^{1/2}$ denote the singular values of \mathbf{F} , defined as the square roots of the eigenvalues $\lambda_i^{\mathbf{F}^T \mathbf{F}}$ of the matrix $\mathbf{F}^T \mathbf{F}$. Then, a general class of strain-energy functions for homogeneous materials can be defined by

$$\begin{aligned} \hat{\mathbf{F}} \in \mathbb{M}_+^3 \rightarrow \hat{W}(\mathbf{F}) = & \sum_{i=1}^M a_i (v_1^{\gamma_i} + v_2^{\gamma_i} + v_3^{\gamma_i}) \\ & + \sum_{j=1}^N b_j \left[(v_2 v_3)^{\delta_j} + (v_3 v_1)^{\delta_j} + (v_1 v_2)^{\delta_j} \right] + \Gamma(\det \mathbf{F}), \end{aligned} \quad (4.48)$$

where $a_i > 0$ and $\gamma_i \geq 1$, with $1 \leq i \leq M$. What is more, $b_j > 0$ and $\delta_j \geq 1$, with $1 \leq j \leq N$. The function $\Gamma:]0, +\infty[\rightarrow \mathbb{R}$ is assumed convex. If (4.48) holds, \hat{W} is polyconvex and fulfills the below coerciveness inequality

$$\hat{W}(\mathbf{F}) \geq \alpha \{ \|\mathbf{F}\|^p + \|\text{Cof } \mathbf{F}\|^q \} + \Gamma(\det \mathbf{F}) \quad \text{for all } \mathbf{F} \in \mathbb{M}_+^3$$

for $\alpha > 0$, $p = \max_i \gamma_i$ and $q = \max_j \delta_j$. To express the sums in (4.48) in terms of \mathbf{F} , the following definitions can be used. Assuming $\mathbf{F} \in \mathbb{M}_+^3$, there exists the unique representation

$$(\mathbf{F}^T \mathbf{F})^{1/2} = \mathbf{P} \text{Diag } v_i \mathbf{P}^T, \mathbf{P} \in \mathbb{O}^3, v_i = v_i(\mathbf{F}) = \{ \lambda_i(\mathbf{F}^T \mathbf{F}) \}^{1/2},$$

where \mathbb{O}^3 denotes the set of all orthogonal matrices of order 3. In the general case the symmetric matrix

$$(\mathbf{F}^T \mathbf{F})^{\delta/2} := \mathbf{P} \text{Diag } v_i^\delta \mathbf{P}^T$$

can be defined for any $\delta > 0$. It can be shown that the above expression is independent of the specific matrix \mathbf{P} used in the diagonalization of $\mathbf{F}^T \mathbf{F}$. Applying the preceding definition the terms involving summation in (4.48) may be replaced by

$$v_1^\gamma + v_2^\gamma + v_3^\gamma = \text{tr}(\mathbf{F}^T \mathbf{F})^{\gamma/2}$$

and

$$(v_2 v_3)^\delta + (v_3 v_1)^\delta + (v_1 v_2)^\delta = \text{tr}(\text{Cof } \mathbf{F}^T \mathbf{F})^{\delta/2}$$

to give

$$\hat{W}(\mathbf{F}) = \sum_{i=1}^M a_i \text{tr}(\mathbf{F}^T \mathbf{F})^{\gamma_i/2} + \sum_{j=1}^N b_j \text{tr}(\text{Cof } \mathbf{F}^T \mathbf{F})^{\delta_j/2} + \Gamma(\det \mathbf{F}).$$

Strain-energy functions of the above type, in agreement with the presumptions pertaining to (4.48) and satisfying

$$\lim_{\delta \rightarrow 0^+} \Gamma(\delta) = +\infty$$

define the class of so-called Ogden materials, see Ogden (1972), which are important from a theoretical point of view and at the same time relevant to practical applications.

A practical criterion, of relevance for the investigations to follow, states that a strain-energy function given in the form

$$\hat{W}(\mathbf{F}) = a_1 \text{tr } \mathbf{C} + a_2 \text{tr}(\mathbf{C}\mathbf{C}) + b \text{tr } \text{Cof } \mathbf{C} \quad \text{with } a_2 > 0, b > 0 \quad (4.49)$$

is not polyconvex if $a_1 < 0$, see Raoult (1986). A deficiency associated with nonpolyconvex energy functions is that only partial existence results are available. This means that there is no guarantee for minimizers to be found. What is more, the energy can turn nonconvex in a way that is not predictable, caused by a certain deformation imposed on the body under investigation. With (4.49) the discussion of the convexity properties of the general hyperelastic SVK model

$$\hat{W}(\mathbf{F}) = \check{W}(\mathbf{E}) = \frac{\lambda}{2} (\text{tr } \mathbf{E})^2 + \mu \text{tr}(\mathbf{E}\mathbf{E}) \quad (4.50)$$

can be continued, where it can be found that there exists the representation

$$\begin{aligned}\hat{W}(\mathbf{F}) &= -\left(\frac{3\lambda + 2\mu}{4}\right)(v_1^2 + v_2^2 + v_3^2) + \left(\frac{\lambda + 2\mu}{8}\right)(v_1^4 + v_2^4 + v_3^4) \\ &\quad + \frac{\lambda}{4}(v_2^2 v_3^2 + v_3^2 v_1^2 + v_1^2 v_2^2) + \left(\frac{6\mu + 9\lambda}{8}\right), \quad v_i = v_i(\mathbf{F}) \\ &= -\left(\frac{3\lambda + 2\mu}{4}\right)\text{tr } \mathbf{C} + \left(\frac{\lambda + 2\mu}{8}\right)\text{tr}(\mathbf{C}\mathbf{C}) + \frac{\lambda}{4}\text{tr } \text{Cof } \mathbf{C} + \left(\frac{6\mu + 9\lambda}{8}\right).\end{aligned}\tag{4.51}$$

It can be observed immediately that the SVK strain-energy is not polyconvex, as there is a negative sign in front of the first term on the right hand sides of (4.51). From the fact that (4.50) is not polyconvex it is obvious that care must be taken when dealing with SVK material models. However, it must be noted that there exist methods to construct polyconvex energy functions that reproduce the behavior of an SVK material for $\|\mathbf{E}\|$ small, see Ciarlet and Geymonat (1982). In general, it can be assumed that SVK materials perform adequately only for large displacements causing small strains, hence being called ‘large displacement–small strain’ models, see Ciarlet (1988). Hyperelastic SVK models do not work well for large compressive strains and have to be avoided in the investigation of this kind of deformation, see e.g. Holzapfel (2000). For instance, it can be shown in a one-dimensional setting that the energy turns nonconvex in purely elastic compression, see Ibrahimbegovic (2009). \triangle

One of the fundamental hypotheses of the current Chapter is that the formation of microstructure is possible only when the relaxed energy, obtained from the free energy via minimization, turns out to be nonconvex, see Carstensen et al. (2002); Ortiz and Repetto (1999). It is assumed that this is due to the kinematics introduced in (4.1). From the mathematical point, to be able to predict nonconvexity as a result of the multiplicative decomposition of the deformation gradient, along with the form of the plastic deformation chosen, the underlying strain-energy function must exhibit polyconvexity. To see the impact of the choice of the strain-energy function on the results of the computations, the SVK energy is compared with a polyconvex model, based on a compressible neo-Hookean (NH) strain-energy, according to Kochmann and Hackl (2010). Both energy formulations are introduced below, accompanied by their respective constitutive relations resulting from nonlinear CDT.

The SVK model is defined by the free energy per unit volume of the undeformed crystal, given as

$$\Psi^{SVK}(\mathbf{E}^e, \rho) = \frac{\lambda}{2}(\text{tr } \mathbf{E}^e)^2 + \mu \text{tr}(\mathbf{E}^e \mathbf{E}^e) - \mu\chi(\ln J^e)^3 + \mu cb^2 \rho.\tag{4.52}$$

The elastic Green-Lagrange strain tensor is defined as $\mathbf{E}^e = \frac{1}{2}(\mathbf{C}^e - \mathbf{I})$, combining (4.7) and (4.1) along with (4.8). As explained before, the third term in (4.52) is a correction, needed for the energy to satisfy the growth condition (3.56) and at the same time ensuring adequate material behavior for small strains, as observed in metals. The determinant of the elastic deformation is denoted J^e , where from (4.1) and taking into account that the plastic deformation is volume preserving $J^e = \det \mathbf{F}^e = \det \mathbf{F} = J$. For positive and small χ and the principal stretches tending to 1 the correction term is small, too. An alternative approach to formulating the free energy using the Hencky strain can be found in Xiao et al. (1997); Brünig (1999). The last term of (4.52) represents the energy of the dislocation network appropriate for small dislocation densities, see Ortiz and Repetto (1999); Berdichevsky (2006b), where c is a positive parameter of the order of 0.3.

To get the constitutive equations the general expressions as given in the preceding Section 4.1.2 can be applied to the energy formulation (4.52). Then, the first Piola-Kirchhoff stress can be obtained as

$$\mathbf{P}^{SVK} = 2\mathbf{F}^e \Psi_{C^e} \mathbf{F}^{p-T} = \mathbf{F}^e \left[\lambda (\text{tr} \mathbf{E}^e) \mathbf{I} + 2\mu \mathbf{E}^e - 3\mu\chi (\ln J^e)^2 \mathbf{C}^{e-1} \right] \mathbf{F}^{p-T}. \quad (4.53)$$

The resolved shear stress reads

$$\begin{aligned} \tau_r^{SVK} &= -w_\beta = -\mathbf{s} \cdot \mathbf{F}^{eT} \mathbf{P}^{SVK} \mathbf{m} \\ &= -\mathbf{s} \cdot \mathbf{C}^e \left[\lambda (\text{tr} \mathbf{E}^e) \mathbf{I} + 2\mu \mathbf{E}^e - 3\mu\chi (\ln J^e)^2 \mathbf{C}^{e-1} \right] \mathbf{F}^{p-T} \mathbf{m} \end{aligned} \quad (4.54)$$

and the back stress can be written as

$$\zeta^{SVK} = \nabla \cdot w_{\nabla\beta} = \mu cb \nabla \cdot [\text{sgn}(\nabla\beta \cdot \mathbf{s}) \mathbf{s}], \quad (4.55)$$

which is nonzero unless the dislocation density equals zero. In the zero case the back stress must be interpreted as the subderivative.

The free energy density per unit volume of the undeformed crystal for the NH material reads

$$\Psi^{NH}(\mathbf{C}^e, \rho) = \frac{\mu}{2} (\text{tr} \mathbf{C}^e - 3) + \frac{\lambda}{4} \left[J^{e2} - 2 \left(1 + 2\frac{\mu}{\lambda} \right) \ln J^e - 1 \right] + \mu cb^2 \rho, \quad (4.56)$$

where the compressible formulation is taken according to Kochmann and Hackl (2010). Denoting the compressibility contribution of (4.56) by $\Gamma(\delta) = \frac{\lambda}{4} [\delta^2 - 2(1 + 2\frac{\mu}{\lambda}) \ln \delta - 1]$ it can be found from $\Gamma''(\delta) = \frac{\lambda}{4} [2 + 2(1 + 2\frac{\mu}{\lambda}) \delta^{-2}] > 0$ for all $\delta > 0$ that Γ is a convex function. Thus, taking into account that $\text{tr} \mathbf{C}^e = \text{tr} \mathbf{F}^{eT} \mathbf{F}^e = \|\mathbf{F}^e\|^2$, the compressible NH formulation used is polyconvex.

Again, the corresponding constitutive equations may be derived from the general expressions. The first Piola-Kirchhoff stress is given by

$$\mathbf{P}^{NH} = 2\mathbf{F}^e \Psi_{C^e} \mathbf{F}^{p-T} = \mathbf{F}^e \left\{ \mu \mathbf{I} + \frac{\lambda}{2} \left[J^{e2} - \left(1 + 2\frac{\mu}{\lambda} \right) \right] \mathbf{C}^{e-1} \right\} \mathbf{F}^{p-T}. \quad (4.57)$$

Deriving the resolved shear stress and the back stress yields

$$\tau_r^{NH} = -w_\beta = -\mathbf{s} \cdot \mathbf{F}^{eT} \mathbf{P}^{NH} \mathbf{m} = -\mathbf{s} \cdot \mathbf{C}^e \left\{ \mu \mathbf{I} + \frac{\lambda}{2} \left[J^{e2} - \left(1 + 2\frac{\mu}{\lambda} \right) \right] \mathbf{C}^{e-1} \right\} \mathbf{F}^{p-T} \mathbf{m} \quad (4.58)$$

and

$$\zeta^{NH} = \nabla \cdot w_{\nabla\beta} = \mu cb \nabla \cdot [\text{sgn}(\nabla\beta \cdot \mathbf{s}) \mathbf{s}], \quad (4.59)$$

respectively, where (4.59) coincides with (4.55) since the expression for the energy of the dislocation network is the same in both cases.

4.1.4 Plane-Strain Deformation and Laminate Construction

In this Section the relations established before in their general form are defined for the case of a plane-strain setting, where the expressions of the free energy, as introduced in (4.52) and (4.56) are used.

Assume a single crystal which occupies a region in space that has the shape of a rectangular cuboid of width L , height H and depth D and is dislocation-free in its reference configuration. Its geometry is given with respect to a Cartesian coordinate frame in Euclidean space, as defined in Section 3.1, such that $0 \leq X_1 \leq L$, $0 \leq X_2 \leq H$ and $0 \leq X_3 \leq D$, depicted in Figure 4.7. A state of plane-strain is realized prescribing $D \gg L, H$. Therefore, $x_3 = X_3$ everywhere,

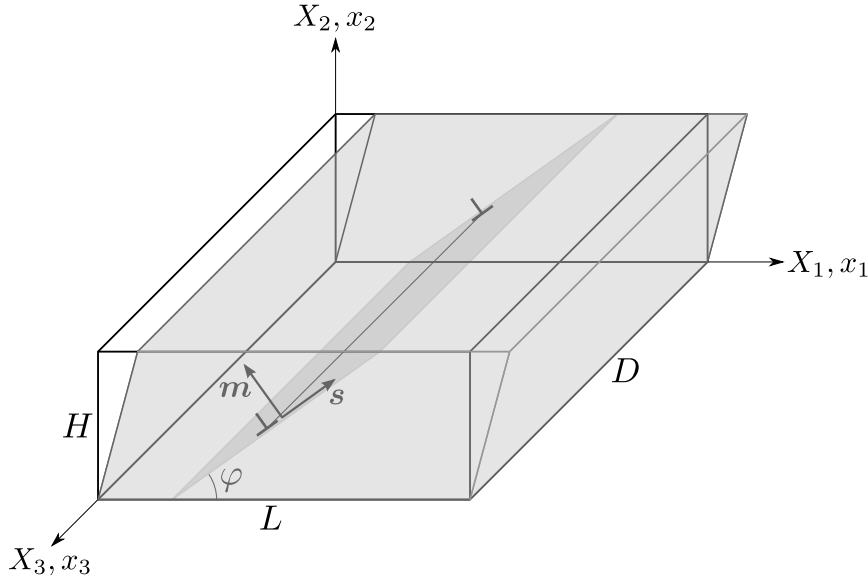


Figure 4.7: Reference state and plane-strain shear deformation of a single crystal containing a single active slip system.

rendering the deformation mapping

$$\mathbf{x} = \mathbf{x}(\mathbf{X})$$

two-dimensional. If the crystal is exposed to small displacements it is assumed to deform elastically and there is no plastic slip. Edge dislocations may be created at the crystal's boundary due to large deformations, where the slip direction and the orientation of the Burgers vectors are characterized by an orientation inclined at an angle φ with respect to the X_1 -axis. In addition to that, the straight dislocation lines have an orientation that coincides with the X_3 -axis. Hence, the single active slip system can be defined by vectors

$$\mathbf{s} = [\cos \varphi \quad \sin \varphi]^T, \quad \mathbf{m} = [-\sin \varphi \quad \cos \varphi]^T. \quad (4.60)$$

In (4.60) \mathbf{s} denotes the slip direction and \mathbf{m} represents the unit normal to the slip plane. What is more, in plane-strain plastic slip β is a function of X_1 and X_2 only and the element of area dA is defined in the (X_1, X_2) -plane. Thus, the resultant Burgers vector of excess dislocations with straight dislocation lines piercing dA at an angle of 90° reads

$$\mathbf{b}_r = \mathbf{s} (\beta_{,1} \cos \varphi + \beta_{,2} \sin \varphi) dA.$$

As the orientation of \mathbf{b}_r coincides with the direction of \mathbf{s} it can be deduced that the above formulation just accounts for edge dislocations. Then, the scalar dislocation density is given by

$$\rho = \frac{1}{b} |\beta_{,1} \cos \varphi + \beta_{,2} \sin \varphi|.$$

Now, the crystal, as specified before, is placed in a ‘hard’ device, imposing the deformation

$$x_1 = X_1 + \gamma X_2, \quad x_2 = X_2$$

at its boundary, where γ denotes the overall shear strain, thus defining a plane-strain simple shear deformation. The goal is to find a deformation $\mathbf{x}(\mathbf{X})$ and plastic slip $\beta(\mathbf{X})$ for a prescribed shear strain γ . The corresponding total and plastic deformations read

$$\mathbf{F} = \mathbf{I} + \gamma \mathbf{e}_1 \otimes \mathbf{e}_2, \quad \mathbf{F}^p = \mathbf{I} + \beta \mathbf{s} \otimes \mathbf{m}. \quad (4.61)$$

Since deformations (4.61) are assumed uniform, γ and β are constants. From (4.1) the elastic deformation can be obtained as $\mathbf{F}^e = \mathbf{F} \mathbf{F}^{p-1}$. For the specific case under investigation, combining (4.60) and (4.61), the following expression

$$\mathbf{F}^e = \begin{bmatrix} \beta \gamma \sin^2 \varphi + \beta \cos \varphi \sin \varphi + 1 & \gamma (1 - \beta \cos \varphi \sin \varphi) - \beta \cos^2 \varphi \\ \beta \sin^2 \varphi & 1 - \beta \cos \varphi \sin \varphi \end{bmatrix} \quad (4.62)$$

can be found for the elastic contribution to the deformation. As simple shear is a plane isochoric deformation, see e.g. Ogden (1997), the Jacobian is $J = \det \mathbf{F} = 1 = \det \mathbf{F}^p$ and hence $\det \mathbf{F}^e = 1$, too. Presuming uniform plastic deformation, it can be seen from (4.10) that the dislocation density ρ equals zero. Thus, the terms containing J^e , as well as the last terms of (4.52) and (4.56) vanish.

For fixed $\gamma \geq 0$ there are situations under which the elastic Green-Lagrange strain tensor \mathbf{E}^e vanishes, where it turns out that \mathbf{s} must be in the second or fourth quadrant of the (X_1, X_2) -plane, corresponding to $\varphi \in (\pi/2, \pi)$ or $\varphi \in (-\pi/2, 0)$, respectively. In addition to that, the elastic deformation must be a pure rotation for \mathbf{E}^e to attain zero entries. From (4.62) it can be deduced that this is true if

$$\gamma = -2 \cot \varphi, \quad \beta = 2 \cot \varphi,$$

so that \mathbf{F}^e can be expressed in following form

$$\mathbf{F}^e = \begin{bmatrix} -\cos 2\varphi & -\sin 2\varphi \\ \sin 2\varphi & -\cos 2\varphi \end{bmatrix},$$

independent of γ and β . Comparing the above expression with the standard rotation matrix

$$\mathbf{R}^e = \begin{bmatrix} \cos \theta & \sin \theta \\ -\sin \theta & \cos \theta \end{bmatrix},$$

where the rotation is clockwise through an angle θ , gives relation $\theta = 2\varphi + \pi$. As stated before, a vital ingredient to the construction of laminate structures based on energetic considerations, according to Ortiz and Repetto (1999); Ortiz et al. (2000); Carstensen et al. (2002), is the non-convexity of the energy function. That is why the features of \mathbf{E}^e are of paramount importance to the investigations at hand. From the above discussion it can be concluded that there exist situations, where the elastic Green-Lagrange strain \mathbf{E}^e renders the energy function nonconvex for uniform deformations. To see that, the free energy densities proposed in (4.52) and (4.56) are taken as a basis, where the Lamé constants are set to $\lambda = 40.38$ GPa and $\mu = 26.92$ GPa, respectively. Then, choosing different slip system orientations in the range $\varphi \in (\pi/2, \pi)$ and $\varphi \in (-\pi/2, 0)$, the normalized energy $E(\gamma, \beta)$, obtained by dividing the free energy by the second Lamé parameter μ and the volume of the crystal $|\mathcal{V}|$, is computed. Solving $\partial E / \partial \beta = 0$

for β , the minimum of the energy with respect to β can be found, which after substitution into the normalized energy yields an expression for the condensed energy $e(\gamma)$. The corresponding plots of $e^{SVK}(\gamma)$ and $e^{NH}(\gamma)$ are shown in the below Figures 4.8 and 4.9, respectively.

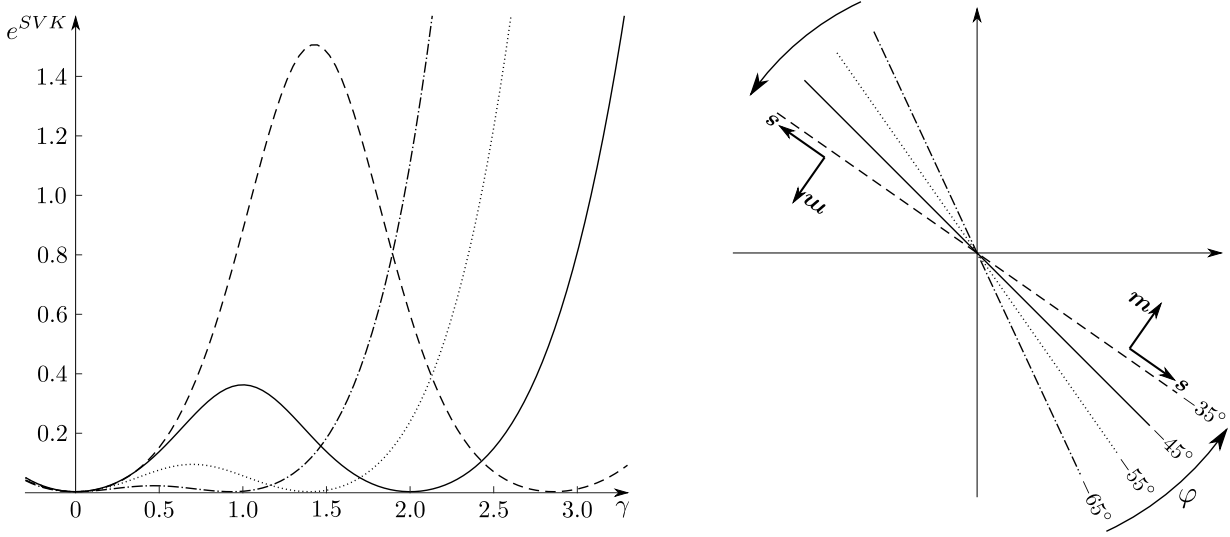


Figure 4.8: Nonconvex energy function plots of SVK type for different choices of the slip system orientation.

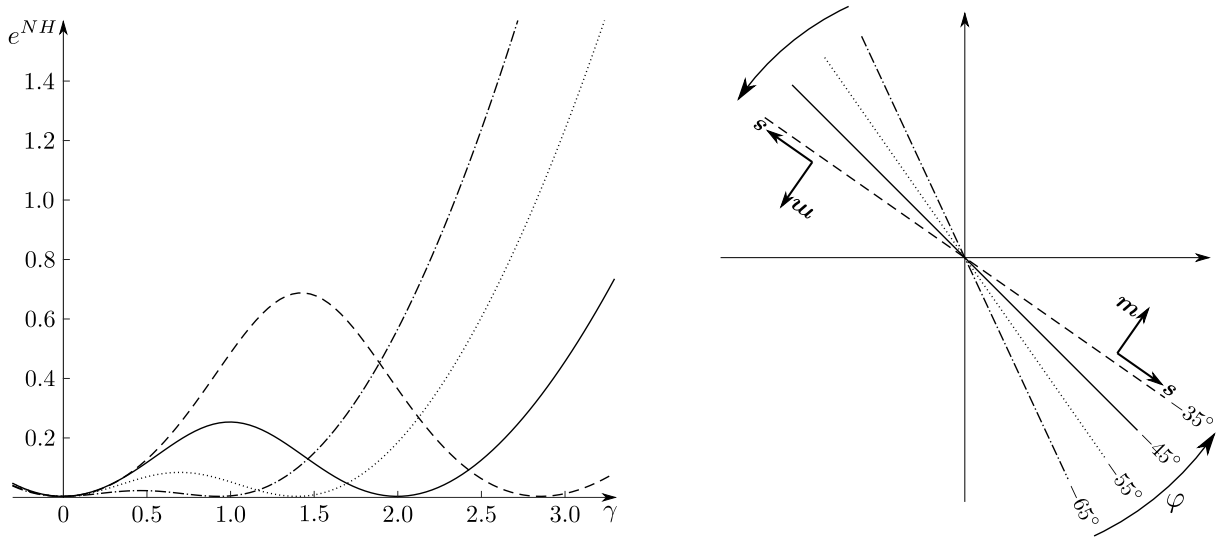


Figure 4.9: Nonconvex energy function plots of NH type for different choices of the slip system orientation.

It can be seen immediately that the condensed energy function plots are nonconvex for the slip system orientations chosen, proving the above hypothesis. The orientation φ is indicated on the right side of both Figures, implying that the plots coincide for slip system orientations rotated by 180° , i.e. the functions are identical for $\varphi = -65^\circ$ and $\varphi = 115^\circ$, $\varphi = -55^\circ$ and $\varphi = 125^\circ$,

$\varphi = -45^\circ$ and $\varphi = 135^\circ$, as well as $\varphi = -35^\circ$ and $\varphi = 145^\circ$. The qualitative behavior of the condensed energy is equal for both models, where it has to be noted that nonconvexity in all cases is due to a double-well energy function with the same minimum values for the same slip system orientations, corresponding to a zero energy. The first minimum value is always at $\gamma = 0$ and the second one is shifted more and more to the right, the greater the slip system orientation becomes. It can be observed that the maxima of the models diverge as the angle φ becomes greater.

According to the choice of slip system in Carstensen et al. (2002) in what follows explicit expressions for $E(\gamma, \beta)$, $\beta(\gamma)$ and $e(\gamma)$ are provided for $\varphi = -45^\circ$. For the SVK model the normalized energy is given as

$$\begin{aligned} E^{SVK}(\gamma, \beta) = & \left\{ \frac{1}{2} \left[\left(\gamma - \frac{\beta}{2} + \frac{\beta\gamma}{2} \right)^2 + \left(\frac{\beta}{2} + 1 \right)^2 - 1 \right] \right\}^2 \\ & + \frac{3}{8} \left\{ \left[\left(\gamma - \frac{\beta}{2} + \frac{\beta\gamma}{2} \right)^2 + \left(\frac{\beta}{2} + 1 \right)^2 + \left(\frac{\beta\gamma}{2} - \frac{\beta}{2} + 1 \right)^2 + \frac{\beta^2}{4} \right] - 2 \right\}^2 \\ & + \left\{ \frac{1}{2} \left[\left(\frac{\beta\gamma}{2} - \frac{\beta}{2} + 1 \right)^2 + \frac{\beta^2}{4} - 1 \right] \right\}^2 \\ & + \frac{1}{2} \left[\left(\frac{\beta\gamma}{2} - \frac{\beta}{2} + 1 \right) \left(\gamma - \frac{\beta}{2} + \frac{\beta\gamma}{2} \right) + \frac{\beta}{2} \left(\frac{\beta}{2} + 1 \right) \right]^2, \end{aligned} \quad (4.63)$$

the NH material formulation yields

$$E^{NH}(\gamma, \beta) = \frac{\beta^2 \gamma^2}{4} - \frac{\beta^2 \gamma - \beta^2 - \beta \gamma^2 - \gamma^2}{2}. \quad (4.64)$$

From computing the partial derivatives of (4.63) and (4.64) with respect to β and setting the resulting functions equal to zero, respectively, the functions of plastic slip can be found for the models under investigation. It turns out that both formulations amount to the same minimizer

$$\beta^{SVK, NH} = -\frac{\gamma^2}{\gamma^2 - 2\gamma + 2}. \quad (4.65)$$

A plot of the energy landscape for both models according to (4.63) and (4.64) is shown in Figure 4.10. To actually see the nonconvexity of the energy surface, the minimizing function (4.65) is plotted in the (γ, β) -plane along with the corresponding curve on the energy surface above it. It can be seen that the energies of both models behave similarly along (4.65) and large differences in their magnitude can be found approaching points $(0, -2)$ and $(2, 0)$.

Plugging the above result (4.65) back in (4.63) and (4.64) gives the condensed energy functions

$$e^{SVK}(\gamma) = \min_{\beta} E^{SVK} = \frac{\gamma^2 (\gamma - 2)^2 (7\gamma^4 - 28\gamma^3 + 44\gamma^2 - 32\gamma + 32)}{64 (\gamma^2 - 2\gamma + 2)^2}, \quad (4.66)$$

$$e^{NH}(\gamma) = \min_{\beta} E^{NH} = \frac{\gamma^2 (\gamma - 2)^2}{4 (\gamma^2 - 2\gamma + 2)}. \quad (4.67)$$

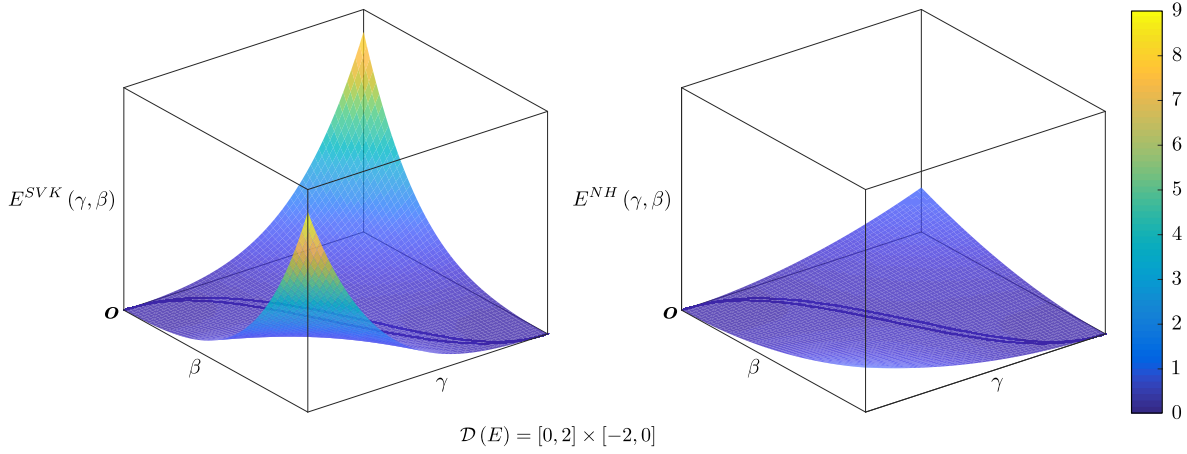


Figure 4.10: Comparison of energy landscape plots for the SVK and the NH model on the domain $[0, 2] \times [-2, 0]$.

The below Figure 4.11 shows a comparison of the plots of the condensed energies (4.66) and (4.67), where here and in what follows the starred plot corresponds to the NH formulation, as indicated in the illustration. Both energy functions exhibit nonconvexity on the interval $\gamma \in (0, 2)$, caused by two equal minima at which the energy equals zero, thus constituting a double-well energy. The first minimum can be found at the undeformed state $\gamma = 0$, denoted γ_A , the second one is encountered at $\gamma = 2$, called state γ_B in what follows. It has to be noted that this is true for both models.

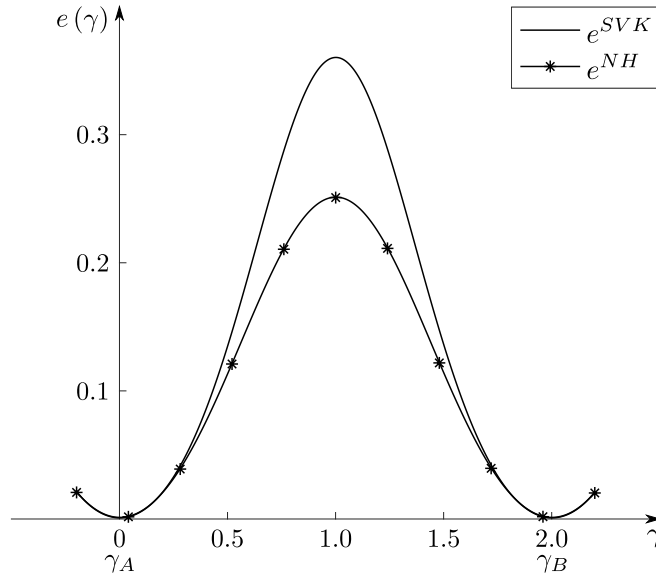


Figure 4.11: Comparison of nonconvex condensed energy plots.

The reason why these two states are of interest is that constructing a tangent line to curve $e(\gamma)$, passing through $\gamma_{A,B}$, and replacing $e(\gamma)$ in the range $\gamma_A < \gamma < \gamma_B$ by this tangent gives the lower convex hull of the condensed energy. As outlined in the interlude in the previous Subsection 4.1.3, the lower convex hull constitutes the largest convex function below the original curve. In the general case the exact values of states $\gamma_{A,B}$ cannot be identified immediately

since $e(\gamma_{A,B}) \neq 0$. An appropriate means to compute the unknown states is Maxwell's rule of equal area, introduced before. Here, it makes use of the fact that $e(\gamma)$ can be obtained from the normalized shear stress $e'(\gamma)$ by integration. Differentiation of (4.66) and (4.67) gives

$$(e^{SVK})'(\gamma) = \frac{\gamma(7\gamma^8 - 63\gamma^7 + 260\gamma^6 - 644\gamma^5 + 1032\gamma^4 - 1072\gamma^3 + 736\gamma^2 - 384\gamma + 128)}{16(\gamma^2 - 2\gamma + 2)^3}$$

and

$$(e^{NH})'(\gamma) = \frac{\gamma(\gamma^4 - 5\gamma^3 + 12\gamma^2 - 16\gamma + 8)}{2(\gamma^2 - 2\gamma + 2)^2},$$

respectively, shown in Figure 4.12. Applying some basic geometry it may be found that there

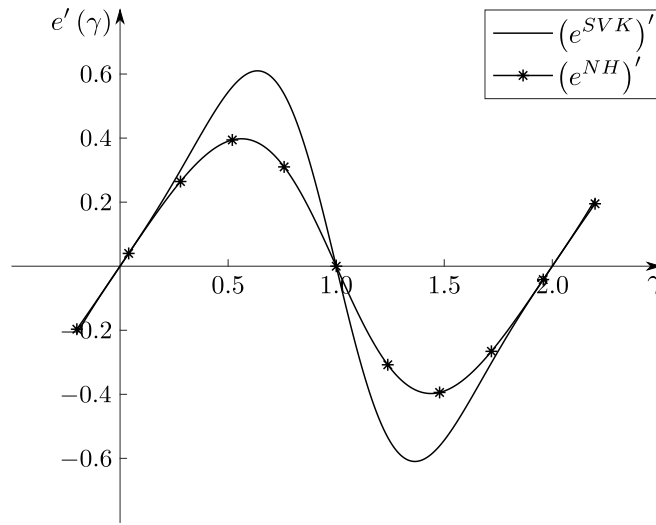


Figure 4.12: Comparison of shear stress plots.

exists a constant function that intersects $e'(\gamma)$ in such a way that the resulting areas enclosed by $e'(\gamma)$ and the horizontal line are of equal area. The points of intersection of the two curves give the values $\gamma_{A,B}$ sought. The resulting value of the constant function then corresponds to the slope of the tangent line to $e(\gamma)$. For more details on the procedure in connection with rank-1 connections and the construction of lower convex hulls see e.g. Šilhavý (1997); Le (2010). In practical applications there are different strategies to actually find the appropriate geometrical construction introduced above.

Here, it can be verified quickly that the tangent line to the condensed energy function is just a horizontal line at $e(\gamma) = 0$, connecting states $\gamma_A = 0$ and $\gamma_B = 2$. From these results the values of plastic slip connected to $\gamma_{A,B}$ can be computed using (4.65), giving $\beta_A = 0$ and $\beta_B = -2$ for both models, since the functions of plastic slip coincide, as found before. A plot of (4.65), accompanied by illustrations of its physical interpretation in terms of plastic slip of atom layers is given in Figure 4.13. It has to be noted that \mathbf{E}^e equals zero at $\gamma_{A,B}$ and hence, according to the before discussion, the condensed energy exhibits nonconvexity for all $\varphi \in (\pi/2, \pi)$ and $\varphi \in (-\pi/2, 0)$ and for all $\lambda \geq 0$.

So far, results have been obtained for the uniform total and plastic deformations, based on the kinematics defined in (4.61). To get the corresponding results for the relevant quantities that specify a 1st-order laminate the set of simultaneous equations defined in Section 4.1.2 has to

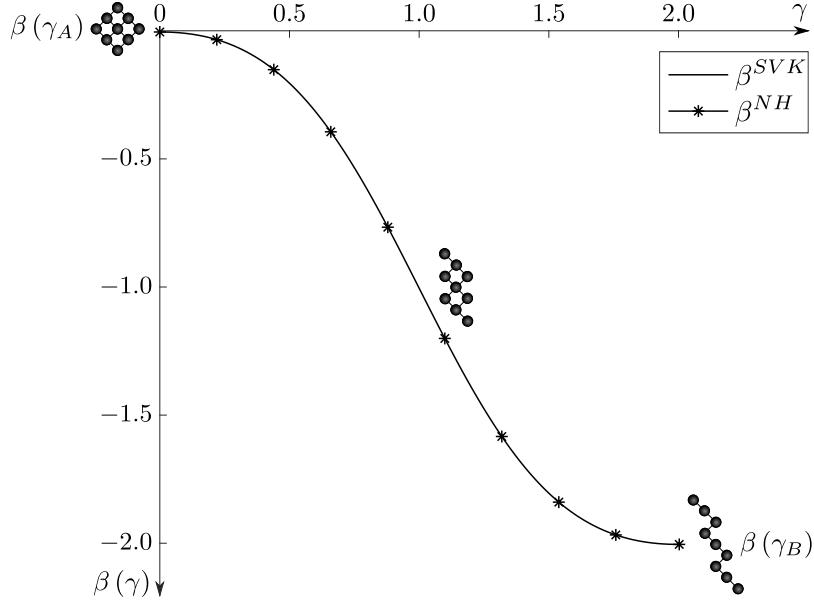


Figure 4.13: Comparison of function plots of plastic slip and the corresponding shift of atomic layers at states $\gamma_A = 0$, $\gamma = 1.0$ and $\gamma_B = 2.0$.

be solved. It can be found that $\mathbf{E}_{A,B}^e$, $\rho_{A,B}$, $w_{A,B}$ and η identically equal zero, where indices A, B indicate evaluation at states A, B . In addition, $\mathbf{C}_{A,B}^e = \mathbf{I}$ and $J_{A,B} = 1$. Then, it can be seen from (4.53) and (4.54) as well as (4.57) and (4.58) that (4.29)_{1,2}, (4.30)_{1,2} and (4.31) are satisfied immediately. For the special case of plane-strain simple shear, assuming uniform deformations, the problem reduces to finding the unknown amplitude of the jump \mathbf{q} and the material unit normal \mathbf{N} from (4.20). Solving the four scalar equations simultaneously for the four unknowns $q_{1,2}$ and $N_{1,2}$ yields

$$\mathbf{q} = \begin{bmatrix} 2 \\ 0 \end{bmatrix}, \quad \mathbf{N} = \begin{bmatrix} 0 \\ 1 \end{bmatrix}. \quad (4.68)$$

Even though the deformations found satisfy equilibrium equations (4.29), they do not constitute the actual minimizers of the energy in the range between γ_A and γ_B , due to the nonconvexity of the condensed energy function on the interval $\gamma \in (0, 2)$. The lowest possible energy can be obtained defining an energy minimizing sequence of placements and plastic slip, making the energy approach zero as close as prescribed, see e.g. Le (2010). The procedure is as follows: the crystal in its undeformed state is divided in alternating laminate layers made up of planes parallel to the (X_1, X_3) -plane, denoted $+$ and $-$, respectively, as illustrated in Figure 4.14. This approach is in agreement with the results found for the unit normal \mathbf{N} , defining laminate strips in the undeformed configuration which are not inclined with respect to the X_1 -axis. Each of both types of layers is assigned a certain volume fraction, where laminate layer $+$ has volume s and layer $-$ is assumed to occupy a volume of $1 - s$. Thus, one pair of layers $+$ and $-$ has a total volume of 1. The total and plastic deformations \mathbf{F}^\pm and $\mathbf{F}^{p\pm}$, intrinsic to these laminate layers, are defined via (4.61), with values of total strain and plastic slip according to

$$\gamma^- = \gamma_A = 0, \quad \gamma^+ = \gamma_B = 2, \quad (4.69)$$

$$\beta^- = \beta_A = 0, \quad \beta^+ = \beta_B = -2. \quad (4.70)$$

Now, all the information needed to perform the construction of a 1st-order laminate is at hand, where the impact of the plastic and elastic contributions of the deformation is investigated in

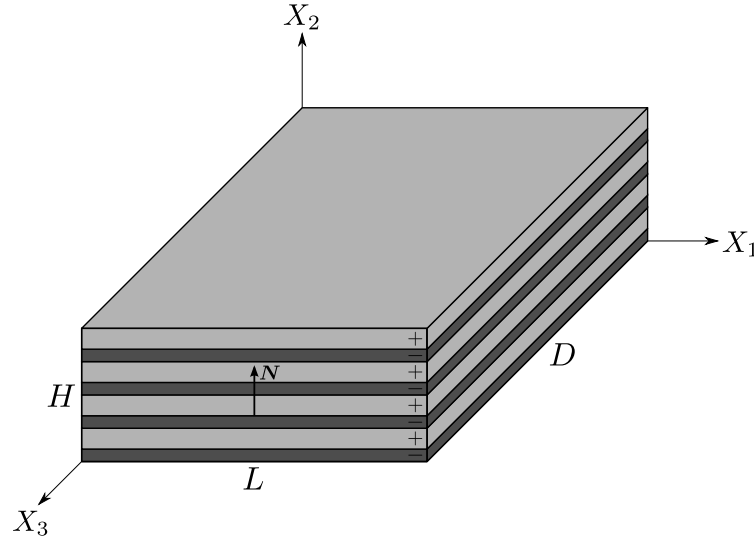


Figure 4.14: Single crystal in its reference configuration divided in layers $+$ and $-$.

detail in what follows. Starting with layer $+$, assume a strip of the undeformed crystal, as defined before. The value of plastic slip of $\beta^+ = -2$ in (4.70) means that each atom layer in the strip is shifted by 2 lattice positions in the direction of $-\mathbf{s}$, where the original layer has a simple cubic crystal structure with orientation $\varphi = -45^\circ$, according to the choice of slip system. This plastic deformation must be assisted by a large number of dislocations. As the slip system orientation tends to -90° , less and less dislocations are needed to achieve a plastic deformation of this kind. The justification for these assumptions can be given by physical reasoning. Since the crystal is initially dislocation-free, as presumed before, dislocations must be created in the form of dipoles, i.e. statistically stored dislocations, through thermal fluctuations, which requires only a small amount of energy, see Berdichevsky and Le (2002). In the presence of a large resolved shear stress, of the order of the theoretical strength of material, as shown in Figure 4.12, dislocation dipoles turn to freely moving dislocations, where the sign determines the direction of the motion. When these dislocations hit the boundary of the crystal strip the energy as well as the stresses decay to a value of zero. This is what happens during plastic deformation. As discussed before, the elastic deformation must be a pure rotation, where the angle of rotation is 90° clockwise in the case under investigation. Then, \mathbf{F} corresponds to a simple shear deformation with total shear strain $\gamma = 2$. The deformation of layer $+$ is shown in Figure 4.15, illustrating the effect of the plastic and elastic contributions to the deformation, according to (4.1). From (4.69) and (4.70) it can be seen that laminate layer $-$ is not exposed to any deformation at all and remains in its undeformed state.

Eventually, the resulting 1st-order laminate structure can be obtained by joining two single layers of species $+$ and $-$ and then stacking this bundle repeatedly, as shown schematically in Figure 4.16, where the transition from γ_A to γ_B is indicated in the plot on the right by the change of color of the tangent line connecting states A and B from dark gray to light gray. In the present case the interfaces between adjacent laminate layers can be interpreted as coherent grain boundaries, not exhibiting misorientation. However, in the general case incoherent grain boundaries are encountered, where the misorientation is governed by the elastic rotation angle $\theta = 2\varphi + \pi$. Due to the geometrical arrangement discussed before there are alternating parts of the crystal's external boundaries $(0, X_2)$ and (L, X_2) which are undeformed and sheared, respectively, according to $\gamma^- = 0$ and $\gamma^+ = 2$. From relation $\gamma = s\gamma^+ + (1-s)\gamma^-$, see e.g. Le

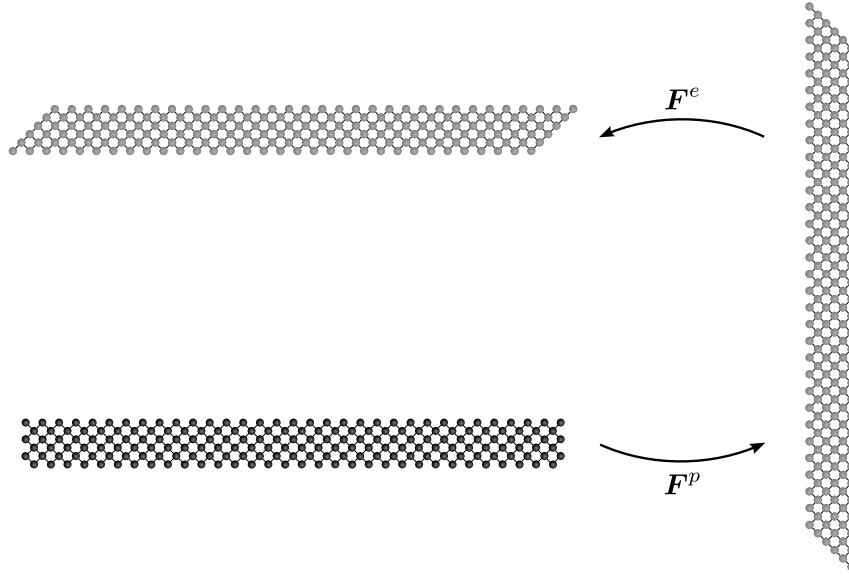


Figure 4.15: Deformation $\mathbf{F} = \mathbf{F}^e \mathbf{F}^p$ acting on atomic layers of the crystal.

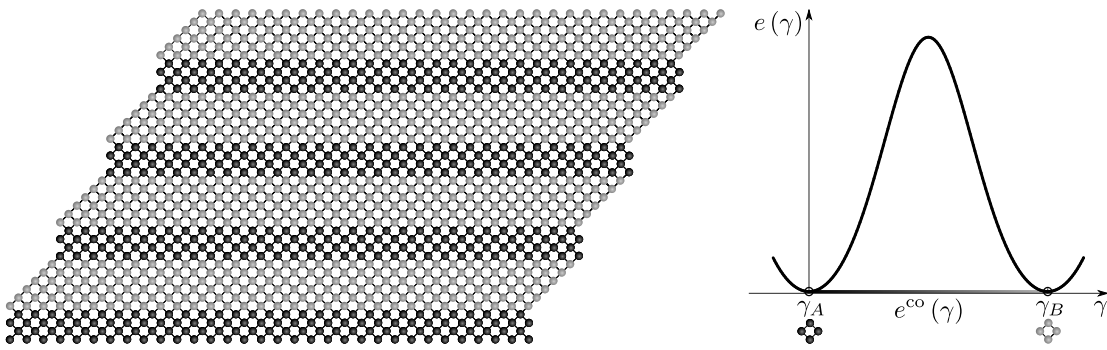


Figure 4.16: 1st-order laminate structure and corresponding lower convex hull of the energy function.

(2010), it can be found that the overall shear may be realized for volume fraction $s = \gamma/2$, where γ depends on the geometry of the simple shear deformation. It has to be noted that the boundary conditions at the external boundaries $(0, X_2)$ and (L, X_2) cannot be satisfied exactly, requiring some correction of α and β in the vicinity of these sides of the crystal. Hence, let the height of a pair of laminate layers $+$ and $-$ be given as ε . From minimization of the sum of the energy contributions of boundary layers near the side boundaries and the energy of grain boundaries, of the order of $\mu H D \varepsilon$ and ζ^{DLH}/ε , respectively, it can be found that $\varepsilon \sim \sqrt{\zeta^L/\mu}$, which reveals the size effect.

The idea of constructing laminate structures resulting from large plastic deformations is based on the experimental observation of shear band formation in ductile metals. The formation and rearrangement of grain boundaries are analyzed extensively using ECAP. There are studies by Fukuda et al. (2003), investigating the impact of ECAP on aluminum single crystals, where it was found that the resulting grain boundaries have a certain inclination, deviating from the horizontal orientation, which is not in agreement with the results obtained from the procedure outlined in the current Section. The same is true for the shearing experiments performed by Dmitrieva et al. (2009). A possible explanation for this discrepancy is the dynamic recrystal-

ization process at high strain rates, i.e. it is hypothesized that the grains in the problem studied in this thesis are not in their final equilibrium state. Additional studies of the behavior of polycrystals exposed to ECAP reveal an elongation and alignment of grains in the direction of shear after processing of the specimens, see e.g. Segal (1995); Lee et al. (2002), which is in good agreement with the results presented before.

4.2 Grain Boundaries of Finite Thickness

In the preceding Section 4.1 a model for the formation of grain boundaries has been established based on the hypothesis that from a nonconvex energy formulation a 1st-order laminate structure can be constructed, interpreting grain boundaries as sharp interfaces. However, in Kuhlmann-Wilsdorf and Hansen (1991) it is pointed out that there exist geometrically necessary boundaries of small but finite thickness, where dislocations accumulate. In what follows, the terms grain boundary and geometrically necessary boundary are used interchangeably. To account for finite-sized boundaries the present Section introduces a dislocation model capable to mimic the formation of nonvanishing grain boundaries within the framework of CDT.

In contrast to what has been presented before, now the plastic slip is assumed to be non-constant. This presumption allows for the introduction of the gradient of plastic slip via the energy of the dislocation network. This is a vital ingredient of the model to be discussed in what follows, as it serves as a regularization of the nonconvex energy minimization problem. Actually, the use of a gradient term in the interfacial energy has already been proposed by Cahn and Hilliard (1958) and may also be found in the more recent literature, see e.g. Bulatov and Cai (2006); Chen (2001); Janssens et al. (2007). The application to crystal plasticity, admitting the physical interpretation of the gradient term as the energy of the dislocation network, is a novel approach, see Koster and Le (2015).

The current analysis takes the results obtained in Section 4.1 as a basis and provides an enhanced laminate model for the case of a simple shear deformation of a single crystal containing a single active slip system, as introduced before. The dislocation structure of a geometrically necessary boundary of small but finite thickness is investigated and the height and the energy of the resulting boundary are given as functions of the misorientation angle θ .

4.2.1 Regularized Energy Functional

According to the situation considered in the previous Subsection 4.1.4 the single crystal to be examined is assumed to be initially dislocation-free. The expression for the incompatible plastic deformation

$$\mathbf{F}^p(\mathbf{X}) = \mathbf{I} + \beta(\mathbf{X}) \mathbf{s} \otimes \mathbf{m},$$

defined by (4.8), is now taken as a function of the material coordinates \mathbf{X} . In addition to that, in virtue of (4.1), the incompatible elastic deformation

$$\mathbf{F}^e = \mathbf{F} \mathbf{F}^{p-1} = \frac{\partial \mathbf{x}}{\partial \mathbf{X}} [\mathbf{I} - \beta(\mathbf{X}) \mathbf{s} \otimes \mathbf{m}]$$

is formulated using the most general form of the deformation gradient (3.7). The dislocation density tensor

$$\mathbf{T} = -\mathbf{F}^p \times \nabla = \mathbf{s} \otimes (\nabla \beta \times \mathbf{m}),$$

given in its material form (4.9), provides a measure of the incompatibility of \mathbf{F}^p and the corresponding formula for the scalar dislocation density

$$\rho = \frac{|\mathbf{T}\mathbf{l}|}{b} = \frac{1}{b} |(\nabla \beta \times \mathbf{m}) \cdot \mathbf{l}|$$

is chosen in accordance with (4.10), where the straight dislocation lines have an orientation perpendicular to the unit vector \mathbf{l} . Recalling the discussion of the properties of energy functions in Subsection 4.1.3, the free energy per unit volume of the undeformed crystal is proposed in two forms, corresponding to the SVK material type of energy

$$\Psi^{SVK}(\mathbf{E}^e, \rho) = \frac{1}{2} \lambda (\text{tr} \mathbf{E}^e)^2 + \mu \text{tr}(\mathbf{E}^e \mathbf{E}^e) - \mu \chi (\ln J^e)^3 + \frac{1}{2} \mu k \frac{\rho^2}{\rho_s^2} \quad (4.71)$$

and the NH model

$$\Psi^{NH}(\mathbf{C}^e, \rho) = \frac{\mu}{2} (\text{tr} \mathbf{C}^e - 3) + \frac{\lambda}{4} \left[J^{e2} - 2 \left(1 + 2 \frac{\mu}{\lambda} \right) \ln J^e - 1 \right] + \frac{1}{2} \mu k \frac{\rho^2}{\rho_s^2}, \quad (4.72)$$

where the last terms in (4.71) and (4.72) represent the energy of the dislocation network for a moderate number of dislocations, with k a material constant and ρ_s the saturated dislocation density. In contrast to that, small or very large dislocation densities, close to ρ_s , can be captured by the logarithmic formulation found in Berdichevsky (2006a).

The crystal, in its reference state occupying some region \mathcal{V} of \mathcal{E} , is deformed in a displacement-controlled manner such that boundary conditions

$$\mathbf{x}(\mathbf{X}) = \bar{\mathbf{F}} \mathbf{X}, \quad \beta(\mathbf{X}) = 0 \quad \text{for } \mathbf{X} \in \partial \mathcal{V} \quad (4.73)$$

hold at $\partial \mathcal{V}$, where $\bar{\mathbf{F}}$ is a prescribed overall isothermal deformation. In addition to that, it is presumed that no body forces act on the crystal and the resistance to dislocation motion is negligibly small. Then, the following variational principle holds: among all continuously differentiable functions $\mathbf{x}(\mathbf{X})$ and $\beta(\mathbf{X})$ the true placement $\check{\mathbf{x}}(\mathbf{X})$ and plastic slip $\check{\beta}(\mathbf{X})$ minimize the functional

$$I[\mathbf{x}(\mathbf{X}), \beta(\mathbf{X})] = \int_{\mathcal{V}} w(\mathbf{F}, \beta, \nabla \beta) \, dV \quad (4.74)$$

in the final equilibrium state of deformation, subject to conditions (4.73). In (4.74) the free energy density is to be interpreted as $w(\mathbf{F}, \beta, \nabla \beta) = \Psi^{SVK}(\mathbf{E}^e, \rho)$ and $w(\mathbf{F}, \beta, \nabla \beta) = \Psi^{NH}(\mathbf{C}^e, \rho)$, respectively. It is shown in what follows that due to the nonconvexity of (4.71) and (4.72) and the introduction of the gradient terms the formation of regular grain boundaries with finite thickness is energetically preferable.

4.2.2 Enhanced Laminate Model

The point of departure of the investigations to follow is Subsection 4.1.4, where the plane-strain simple shear deformation of a single crystal was analyzed. The underlying boundary conditions

$$x_1 = X_1 + \gamma X_2, \quad x_2 = X_2, \quad \beta = 0$$

and uniform total and plastic deformations

$$\mathbf{F} = \overline{\mathbf{F}} = \mathbf{I} + \gamma \mathbf{e}_1 \otimes \mathbf{e}_2, \quad \mathbf{F}^p = \mathbf{I} + \beta \mathbf{s} \otimes \mathbf{m}$$

gave rise to the formation of a 1st-order laminate structure corresponding to constant deformation states in each layer with overall shear strain γ^\pm and plastic slip β^\pm , depending on the slip system orientation φ , according to

$$\begin{aligned} \gamma^- &= 0, & \gamma^+ &= -2 \cot \varphi, \\ \beta^- &= 0, & \beta^+ &= 2 \cot \varphi. \end{aligned}$$

In this case the volume fraction of layer $+$ was given as $s = -\gamma/(2 \cot \varphi)$. It was shown that the equilibrium equations and boundary conditions were satisfied, except at the external boundaries $(0, X_2)$ and (L, X_2) , where a correction was needed. In addition to that, the energy of the resulting laminate structure was found to exhibit the lowest possible value of zero. However, these results are valid only for the formulation assuming grain boundaries as sharp interfaces, where jumps of the total deformation \mathbf{F} and plastic slip β occur, hence, not constituting minimizers of the variational problem defined by (4.73) and (4.74).

In the enhanced laminate model the outcome of the previous investigations is used as a starting point, where the sharp interfaces between laminate layers are replaced by thin layers of thickness h , representing geometrically necessary boundaries containing dislocations. It is assumed that inside these additional layers there exist smooth functions α and β that connect the states γ^\pm and β^\pm in laminate layers $+$ and $-$, as indicated in Figure 4.17 by the change of color of the boundary layer from dark gray at the bottom, related to the deformation properties of state $-$, to light gray at its top surface, where state $+$ governs the deformation. Since the

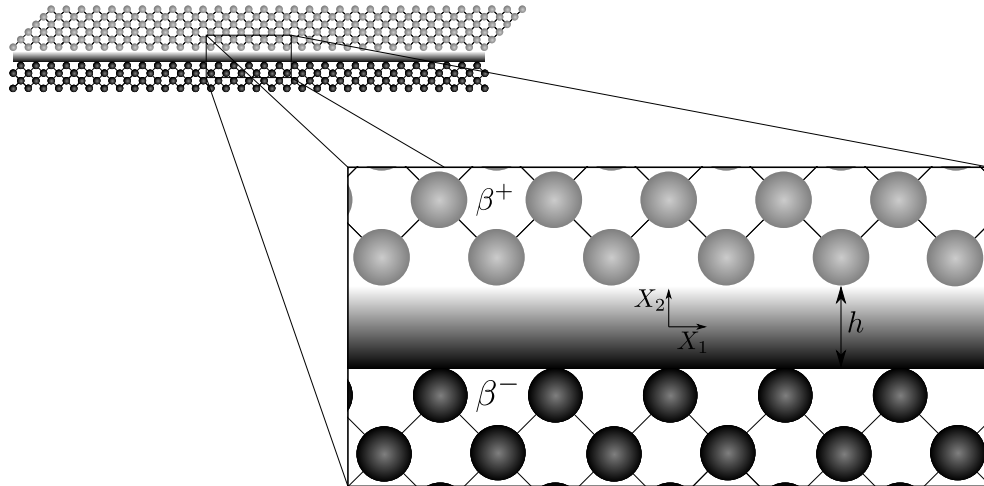


Figure 4.17: Enhanced laminate model.

boundaries are thin, i.e. $h \ll sH, (1-s)H$, and much smaller than the dimensions of the crystal under investigation, it is presumed that the displacement in the X_2 -direction equals zero and the displacement in the X_1 -direction and the plastic slip are functions of coordinate X_2 only, given by

$$x_1 = X_1 + u(X_2), \quad x_2 = X_2, \quad \beta = \beta(X_2).$$

This approach implies that the functions $u(X_2)$ and $\beta(X_2)$ and the unknown boundary layer can be obtained from minimization of the functional

$$I_b[u(X_2), \beta(X_2)] = \int_{l_1}^{l_2} [f(u_{,2}, \beta) + g(\beta_{,2})] dX_2, \quad (4.75)$$

where $u(X_2)$ and $\beta(X_2)$ and the lengths $l_{1,2}$ to be determined must be such that

$$\begin{aligned} u_{,2}(l_1) &= \gamma^- = 0, & u_{,2}(l_2) &= \gamma^+ = -2 \cot \varphi, \\ \beta(l_1) &= \beta^- = 0, & \beta(l_2) &= \beta^+ = 2 \cot \varphi. \end{aligned} \quad (4.76)$$

For the SVK model the function $f(u_{,2}, \beta)$ can be expressed as

$$\begin{aligned} f^{SVK}(u_{,2}, \beta) &= \frac{1}{64} \left\{ 2 \left[(2\beta \cos^2 \varphi - 2u_{,2} + \beta u_{,2} \sin 2\varphi) (2\beta u_{,2} \sin^2 \varphi + \beta \sin 2\varphi + 2) \right. \right. \\ &\quad \left. \left. + 2\beta \sin^2 \varphi (\beta \sin 2\varphi - 2) \right]^2 + 3 (2\beta^2 + 2u_{,2}^2 + \beta^2 u_{,2}^2 - \beta^2 u_{,2}^2 \cos 2\varphi - 4\beta u_{,2} \cos 2\varphi \right. \\ &\quad \left. - 2\beta u_{,2}^2 \sin 2\varphi + 2\beta^2 u_{,2} \sin 2\varphi)^2 + \left[(2\beta u_{,2} \sin^2 \varphi + \beta \sin 2\varphi + 2)^2 + 4\beta^2 \sin^4 \varphi - 4 \right]^2 \right. \\ &\quad \left. + [(\beta - 2u_{,2} + \beta \cos 2\varphi + \beta u_{,2} \sin 2\varphi)^2 + (\beta \sin 2\varphi - 2)^2 - 4]^2 \right\}, \quad (4.77) \end{aligned}$$

the NH formulation leads to

$$\begin{aligned} f^{NH}(u_{,2}, \beta) &= \frac{1}{8} (4\beta^2 + 4u_{,2}^2 + 2\beta^2 u_{,2}^2 - 2\beta^2 u_{,2}^2 \cos 2\varphi \\ &\quad - 4\beta u_{,2}^2 \sin 2\varphi + 4\beta^2 u_{,2} \sin 2\varphi - 8\beta u_{,2} \cos 2\varphi). \quad (4.78) \end{aligned}$$

For both material models the gradient term is defined as

$$g(\beta_{,2}) = \frac{1}{2} k \frac{\beta_{,2}^2 \sin^2 \varphi}{b^2 \rho_s^2}.$$

The above dimensionless expressions can be found from division by μ , using the values for the Lamé constants introduced in Subsection 4.1.4. From the variation of (4.75) with respect to $u(X_2)$, taking into account the boundary conditions (4.76), it can be deduced that

$$\frac{\partial f}{\partial u_{,2}} = 0. \quad (4.79)$$

Hence, no stresses act in the boundary layer. Then, recalling the results obtained in Subsection 4.1.4, it can be concluded that the whole crystal is stress-free. Using (4.77) and (4.78) in (4.79) and solving for $u_{,2}$ the above equation may be expressed as a function of plastic slip β . It turns out that both models give the same result

$$u_{,2}^{SVK,NH}(\beta) = \frac{\beta^2 \sin 2\varphi - 2\beta \cos 2\varphi}{2\beta \sin 2\varphi + \beta^2 \cos 2\varphi - \beta^2 - 2}. \quad (4.80)$$

Plugging (4.80) in (4.77) and (4.78), respectively, yields the energy functional

$$I_b^{SVK,NH}[\beta(X_2)] = \int_{l_1}^{l_2} [p^{SVK,NH}(\beta) + g(\beta_{,2})] dX_2, \quad (4.81)$$

with $\beta(X_2)$, l_1 and l_2 as the independent variables and

$$\begin{aligned}
p^{SVK}(\beta) = & \frac{(\beta \sin 2\varphi - 2)^2}{4(2\beta \sin 2\varphi + \beta^2 \cos 2\varphi - \beta^2 - 2)^2} \\
& + \frac{1}{64} \left[(\beta \sin 2\varphi - 2)^2 + \frac{4\beta^2 (\cos 2\varphi - 1)^2}{(2\beta \sin 2\varphi + \beta^2 \cos 2\varphi - \beta^2 - 2)^2} - 4 \right]^2 \\
& + \frac{1}{8} \left\{ \beta (\beta \sin 2\varphi - 2) \left(\frac{\cos 2\varphi}{2} - \frac{1}{2} \right) + 2 \left[\beta^2 \left(\frac{\cos 2\varphi}{2} - \frac{1}{2} \right)^2 - 1 \right]^2 \right\} \\
& + \frac{64\beta^2 (\beta \sin 2\varphi - 2)^2 (\cos 2\varphi - 1)^2}{1024 \left(8\beta \sin 2\varphi + 4\beta^2 \cos 2\varphi + 2\beta^2 \cos 4\varphi + 2\beta^4 \cos 2\varphi \right. \\
& \quad \left. - \frac{\beta^4 \cos 4\varphi}{2} + 4\beta^3 \sin 2\varphi - 2\beta^3 \sin 4\varphi - 6\beta^2 - \frac{3\beta^4}{2} - 4 \right)^2} \\
& + \frac{3\beta^4 (16 \cos 4\varphi + 56\beta \sin 2\varphi - 16\beta \sin 4\varphi - 8\beta \sin 6\varphi + 28\beta^2 \cos 2\varphi}{1024 \left(8\beta \sin 2\varphi + 4\beta^2 \cos 2\varphi + 2\beta^2 \cos 4\varphi + 2\beta^4 \cos 2\varphi \right. \\
& \quad \left. - \frac{\beta^4 \cos 4\varphi}{2} + 4\beta^3 \sin 2\varphi - 2\beta^3 \sin 4\varphi - 6\beta^2 - \frac{3\beta^4}{2} - 4 \right)^2} \\
& + \frac{20\beta^2 \cos 4\varphi + 15\beta^4 \cos 2\varphi - 12\beta^2 \cos 6\varphi - 6\beta^4 \cos 4\varphi + \beta^4 \cos 6\varphi}{1024 \left(8\beta \sin 2\varphi + 4\beta^2 \cos 2\varphi + 2\beta^2 \cos 4\varphi + 2\beta^4 \cos 2\varphi \right. \\
& \quad \left. - \frac{\beta^4 \cos 4\varphi}{2} + 4\beta^3 \sin 2\varphi - 2\beta^3 \sin 4\varphi - 6\beta^2 - \frac{3\beta^4}{2} - 4 \right)^2} \\
& + \frac{30\beta^3 \sin 2\varphi - 24\beta^3 \sin 4\varphi + 6\beta^3 \sin 6\varphi - 36\beta^2 - 10\beta^4 - 16)^2}{1024 \left(8\beta \sin 2\varphi + 4\beta^2 \cos 2\varphi + 2\beta^2 \cos 4\varphi + 2\beta^4 \cos 2\varphi \right. \\
& \quad \left. - \frac{\beta^4 \cos 4\varphi}{2} + 4\beta^3 \sin 2\varphi - 2\beta^3 \sin 4\varphi - 6\beta^2 - \frac{3\beta^4}{2} - 4 \right)^2}
\end{aligned}$$

for the SVK material and

$$\begin{aligned}
p^{NH}(\beta) = & \frac{\beta^2 (16 \cos 4\varphi + 56\beta \sin 2\varphi - 16\beta \sin 4\varphi - 8\beta \sin 6\varphi + 28\beta^2 \cos 2\varphi}{16 \left(8\beta \sin 2\varphi + 4\beta^2 \cos 2\varphi + 2\beta^2 \cos 4\varphi + 2\beta^4 \cos 2\varphi \right. \\
& \quad \left. - \frac{\beta^4 \cos 4\varphi}{2} + 4\beta^3 \sin 2\varphi - 2\beta^3 \sin 4\varphi - 6\beta^2 - \frac{3\beta^4}{2} - 4 \right)} \\
& + \frac{20\beta^2 \cos 4\varphi + 15\beta^4 \cos 2\varphi - 12\beta^2 \cos 6\varphi - 6\beta^4 \cos 4\varphi + \beta^4 \cos 6\varphi}{16 \left(8\beta \sin 2\varphi + 4\beta^2 \cos 2\varphi + 2\beta^2 \cos 4\varphi + 2\beta^4 \cos 2\varphi \right. \\
& \quad \left. - \frac{\beta^4 \cos 4\varphi}{2} + 4\beta^3 \sin 2\varphi - 2\beta^3 \sin 4\varphi - 6\beta^2 - \frac{3\beta^4}{2} - 4 \right)} \\
& + \frac{30\beta^3 \sin 2\varphi - 24\beta^3 \sin 4\varphi + 6\beta^3 \sin 6\varphi - 36\beta^2 - 10\beta^4 - 16)}{16 \left(8\beta \sin 2\varphi + 4\beta^2 \cos 2\varphi + 2\beta^2 \cos 4\varphi + 2\beta^4 \cos 2\varphi \right. \\
& \quad \left. - \frac{\beta^4 \cos 4\varphi}{2} + 4\beta^3 \sin 2\varphi - 2\beta^3 \sin 4\varphi - 6\beta^2 - \frac{3\beta^4}{2} - 4 \right)}
\end{aligned}$$

the corresponding NH formulation. Performing the variation of (4.81) with respect to $\beta(X_2)$, l_1 and l_2 and considering (4.76) gives the Euler equation

$$\frac{d}{dX_2} g'(\beta, 2) - (p^{SVK, NH})'(\beta) = 0, \quad (4.82)$$

subject to the boundary conditions

$$\begin{aligned}\beta(l_1) &= 0, & \beta(l_2) &= 2 \cot \varphi, \\ \beta_{,2}(l_1) &= 0, & \beta_{,2}(l_2) &= 0.\end{aligned}\tag{4.83}$$

The second row of (4.83) indicates that the dislocation density vanishes at the top and bottom surface of layers $-$ and $+$ in Figure 4.17, respectively. It can be found that (4.82) has a first integral of the form

$$g(\beta_{,2}) - p^{SVK,NH}(\beta) = c.\tag{4.84}$$

Using identities $p^{SVK,NH}(\beta^-) = p^{SVK,NH}(\beta^+) = 0$ and boundary conditions (4.83) it follows that $c = 0$.

The phase portraits related to (4.84) for the SVK material and the NH model are shown in Figure 4.18 and Figure 4.19, respectively, where parameter values $b = 2.5 \times 10^{-10}$ m, $\rho_s = 10^{16}$ m $^{-2}$, $k = 10^{-6}$ and the slip system orientation $\varphi = -\pi/4$ have been used. The phase curves corresponding to the case $c = 0$ are the separatrices, given as the dotted lines, that connect states $-$ and $+$ in the lower half of the $(\beta, \beta_{,2})$ -plane, where the arrow indicates the direction of the change of β as X_2 changes from l_1 to l_2 . It can be shown that the phase curves

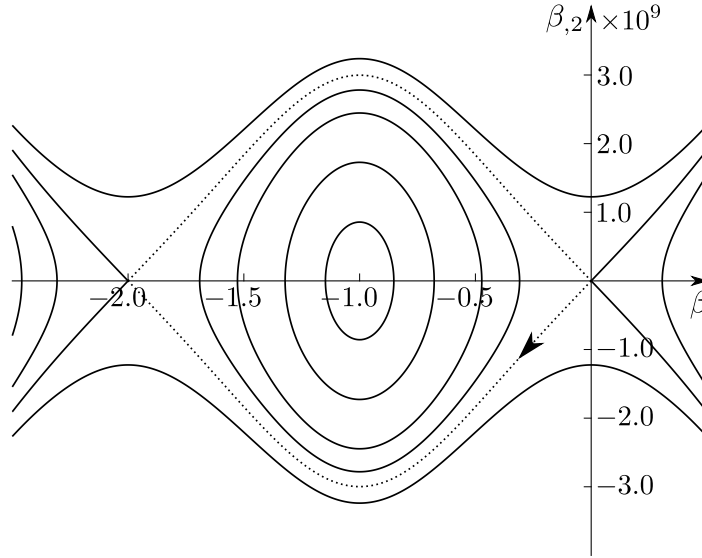


Figure 4.18: Phase plot for the SVK model.

that connect states $+$ and $-$ correspond to the separatrices in the upper half plane, indicating that the dislocations in the boundary layer between $+$ and $-$ have the opposite sign of those occupying the geometrically necessary boundary between layers $-$ and $+$.

From (4.84) β may be obtained implicitly for the case $c = 0$ in terms of the coordinate X_2 , given as

$$X_2 = -\frac{\sqrt{k} |\sin \varphi|}{\sqrt{2} b \rho_s} \int_{\cot \varphi}^{\beta} \frac{dt}{\sqrt{p^{SVK,NH}(t)}}.\tag{4.85}$$

Even though there exists no closed-form solution to the integration in (4.85) it is possible to compute the values on some interval of β using numerical integration. The accompanying plots

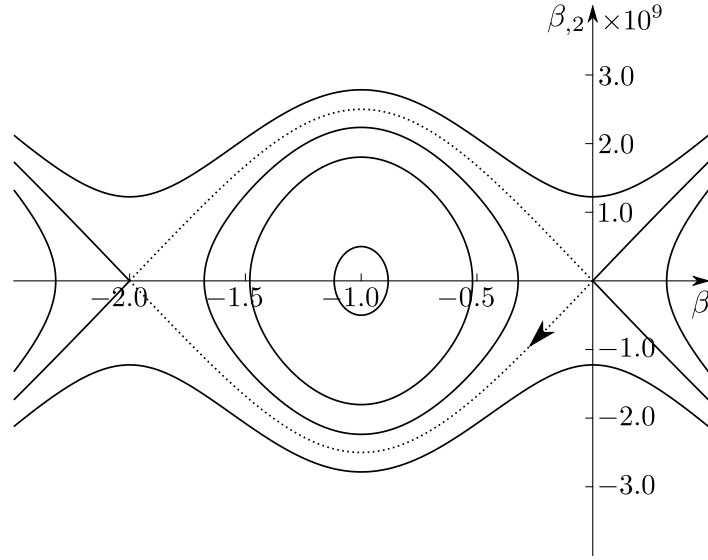
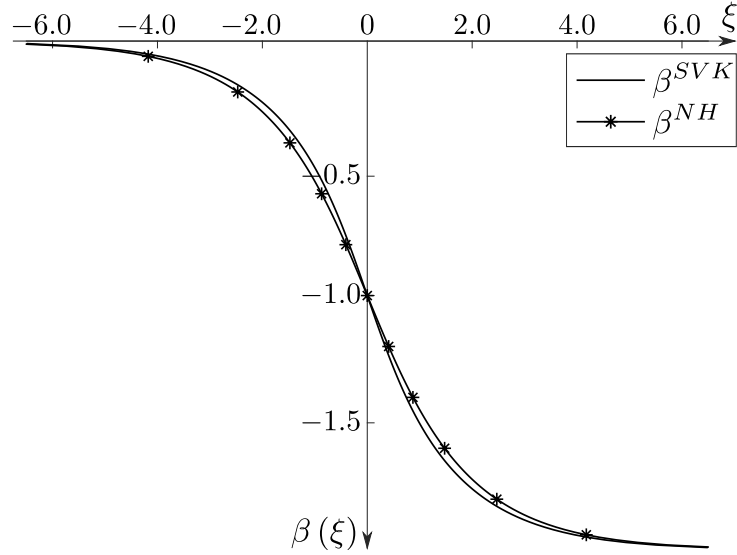


Figure 4.19: Phase plot for the NH model.

of $\beta^{SVK,NH}$ as functions of the dimensionless coordinate $\xi = (\sqrt{2}X_2 b \rho_s)/(\sqrt{k}|\sin \varphi|)$ are depicted in the below Figure 4.20. It can be seen that the curves for the two models under investigation almost coincide and that $\beta^{SVK,NH}$ approach values β^\pm as the magnitude of ξ becomes large, whereas the values of $\beta^{SVK,NH}$ change rapidly in a finite range about $\xi = 0$. Computing the

Figure 4.20: Comparison of the plots of plastic slip as a function of coordinate ξ .

height of the resulting geometrically necessary boundary naively, according to

$$h = l_2 - l_1 = \frac{\sqrt{k}|\sin \varphi|}{\sqrt{2}b\rho_s} \int_{2\cot \varphi}^0 \frac{dt}{\sqrt{p^{SVK,NH}(t)}},$$

it turns out that its value becomes infinitely large. From physical reasoning it can be deduced that the discrete nature of dislocations has to be taken into account here. As there exists only a finite natural number of dislocations inside the crystal the total number of dislocations in the

boundary layer can be computed from the dislocation density $\rho = |\beta_{,2} \sin \varphi|/b$, giving

$$N = L \int_{l_1}^{l_2} \rho dX_2 = |\beta(l_2)| |\sin \varphi| \frac{L}{b}.$$

Since the smallest possible number of dislocations in the boundary equals 1 the corresponding quantum of plastic slip leading to an observable change of N corresponds to $\beta_q = b/(L|\sin \varphi|)$. Then, assuming the ratio b/L small and modifying the limits of integration using β_q , given as

$$h = l_2 - l_1 = \frac{\sqrt{k} |\sin \varphi|}{\sqrt{2} b \rho_s} \int_{2 \cot \varphi + \beta_q}^{-\beta_q} \frac{dt}{\sqrt{p^{SVK,NH}(t)}}, \quad (4.86)$$

the height of the geometrically necessary boundary becomes finite, except for a slip system orientation of $\varphi = -\pi/2$. It can be seen from (4.86) that the height can be interpreted as a function of the slip system orientation. Thus, it is possible to plot the height of the grain boundary versus the angle of misorientation $\theta = 2\varphi + \pi$, as defined in Koster, Le and Nguyen (2015). The plots for both models, using the parameter values introduced before and $b/L = 10^{-4}$, are shown in Figure 4.21. It can be observed that the curves representing the height of the grain

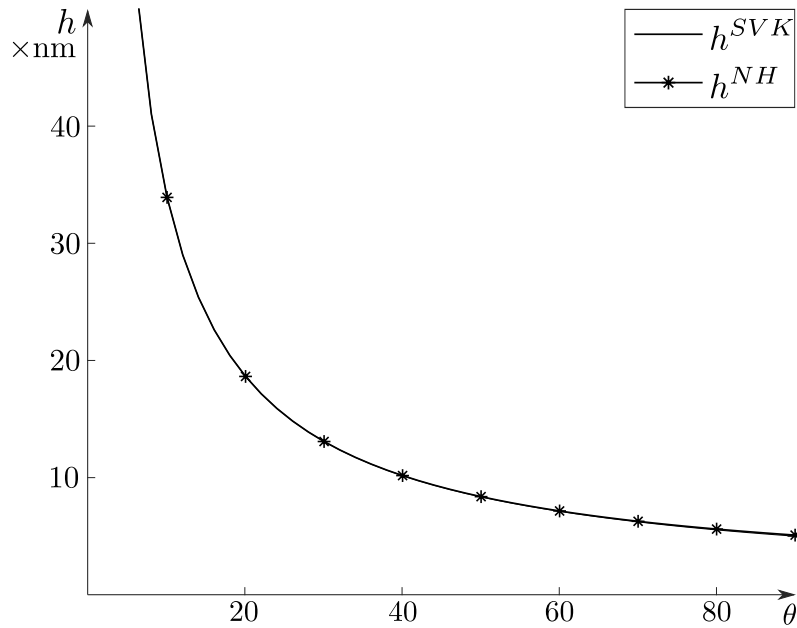


Figure 4.21: Comparison of the plots of the geometrically necessary boundary's height as a function of the angle of misorientation θ (in degrees).

boundary are identical. In both cases the thickness is between 50 nm and 6 nm for $\theta > 10^\circ$, where it must be noted that for very small angles of misorientation (4.86) is not well-defined and the small-angle tilt boundary model given in Read and Shockley (1950) might be more appropriate.

Computing the minimum of (4.81), using the first integral (4.84), it can be found that the energy of the geometrically necessary boundary per unit area, normalized by μ , is given by

$$I_b^{SVK,NH} = 2 \int_{l_1}^{l_2} p^{SVK,NH}(\beta) dX_2 = \frac{2\sqrt{k} |\sin \varphi|}{\sqrt{2} b \rho_s} \int_{2 \cot \varphi}^0 \sqrt{p^{SVK,NH}(\beta)} d\beta. \quad (4.87)$$

Then, the energy density of the boundary corresponds to $\gamma_G^{SVK,NH} = \mu I_b^{SVK,NH}$. By analogy with (4.86) the energy density can be interpreted as a function of θ . Keeping the parameter values as introduced before the plot of the grain boundary's energy density versus the misorientation angle can be obtained, where (4.87) is well-defined for all values of θ , shown in Figure 4.22. Inspecting the curves it can be seen that the energy densities coincide in the range $\theta \in [0, 60]$ and deviate as θ becomes larger, where the values found for the SVK model are greater than those obtained for the NH material. At an angle of misorientation of about 50° the energy density approaches a value of approximately 1 N/m . This is in good agreement with the value of 0.625 N/m , reported in Hirth and Lothe (1982). Recalling the results for the estimation

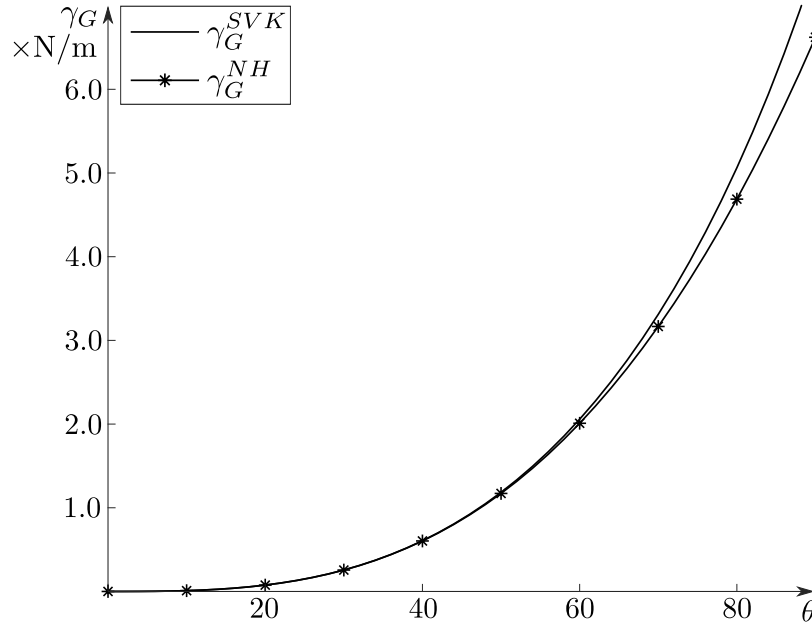


Figure 4.22: Comparison of the plots of the geometrically necessary boundary's energy as a function of the angle of misorientation θ (in degrees).

of the energy of grain boundaries given at the end of Subsection 4.1.4 and taking into account the formulation for the energy of geometrically necessary boundaries, being of the order of $\gamma_G DLH/\varepsilon$, yields

$$\varepsilon \sim \sqrt{\gamma_G L/\mu} \sim \sqrt{I_b L},$$

again exhibiting the size effect. Hence, the vital characteristics of a small but finite-sized geometrically necessary boundary have been established.

4.3 Inclined Grain Boundaries

So far, results have been found that predict a horizontal alignment of 1st-order laminate layers, representing the formation of grain boundaries in ductile single crystals. However, what can be observed in aluminum single crystal samples after ECAP processing is the formation of striations under a certain orientation inclined with respect to the horizontal axis, interpreted as boundaries forming inside the crystal, see e.g. Fukuda et al. (2003). Thus, next a procedure is proposed that allows for the construction of a 1st-order laminate structure, in the same spirit as

outlined in Section 4.1, which gives rise to the orientation of laminate layers other than coinciding with the horizontal axis. This leads to modifications of the laminate model introduced before, where in terms of kinematics a novel geometrical condition is introduced, prescribing the final laminate orientation after an overall shear deformation of the crystal. With regard to the energy formulation it is assumed that a vital ingredient to mimicking the formation of rotated boundaries is the consideration of dissipative effects, reflecting resistance to the motion of dislocations in the crystal. Therefore, the energy has to be enhanced by a term accounting for energy dissipation. This kind of setting results in a more general nonconvex energy, where $e(\gamma_{A,B}) \neq 0$ holds for the minima with states $\gamma_A > 0$ and $\gamma_B > 2$ for a slip system orientation of $\varphi = -\pi/4$.

4.3.1 Kinematics from Experimental Analysis

The following investigation is based on the ECAP experiment discussed in Fukuda et al. (2003). This paragraph gives a brief overview of the experimental findings of importance to the definition of the problem at hand and the corresponding computations. A simplified sketch of the original setup, just providing the details of the geometry of the channel of interest for the problem formulation, is shown in Figure 4.23. The specimen used was a high-purity aluminum

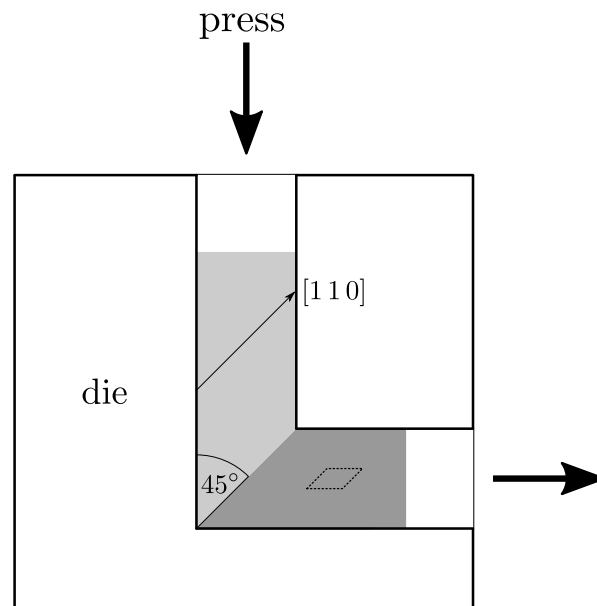


Figure 4.23: ECAP experimental setting, adapted from Fukuda et al. (2003).

single crystal that was processed in a die containing a 90° ECAP channel, where the thick arrows indicate the direction of pressing. The sample was prepared in such a way that the $[1\ 1\ 0]$ slip direction of the FCC crystal was aligned parallel to the theoretical shear plane with orientation 45° . To distinguish the reference state of the crystal from its current configuration the undeformed portion of the crystal is depicted in light gray color, whereas the deformed part is shown in dark gray color. In Fukuda et al. (2003) it was found that after deformation the crystal forms striations, where the pattern of the resulting microstructure depends on the location inside the sample, indicating an inhomogeneous deformation. However, there exist portions of the deformed crystal, where piecewise homogeneous patterns can be identified. The region of the deformed crystal that is of particular importance in what follows is illustrated as the area

enclosed by the dotted line in Figure 4.23, containing prominent striations, inclined under an angle of 20° with respect to the horizontal channel axis. The experimental analysis revealed that this area corresponds to a bicrystal, where one crystal has a lattice orientation that is rotated by 60° with respect to the original lattice and the other crystal exhibits no lattice rotation.

The goal of this Subsection is to provide a continuum interpretation of the experiment described in the above paragraph which is able to mimic the corresponding deformation characteristics. As outlined before, the highlighted area in Figure 4.23 is at the focus of the following analysis. The theoretical experiment associated with the deformation of this region is illustrated in Figure 4.24. In agreement with the computations in Subsection 4.1.4 it is assumed that the part of the single crystal sample of interest undergoes a prescribed deformation $\tilde{\mathbf{F}}$.

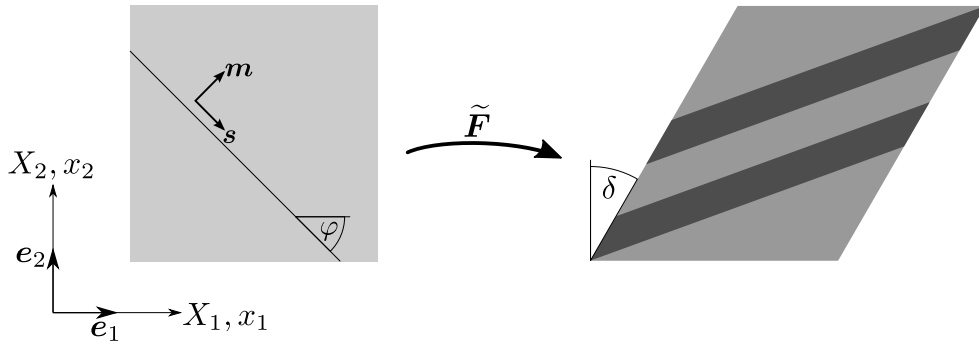


Figure 4.24: Continuum interpretation of the ECAP experiment.

The slip direction $[1\ 1\ 0]$ found in the experiment is interpreted as a slip system orientation of $\varphi = -45^\circ$. It must be pointed out that the alternative choice of $\varphi = 45^\circ$ must be ruled out immediately since this does not lead to a nonconvex energy function, as discussed in Subsection 4.1.4. As opposed to the geometry of the experimental setup the obvious choice of $\delta = 45^\circ$ cannot be assumed a priori. The reason is that the overall shear is governed by the deformation resulting from an energy minimization procedure. It is shown that δ may not be chosen arbitrarily. Finally, the deformation must be such that it gives rise to a 1st-order laminate structure which is inclined under a prescribed angle with respect to the X_1 -axis, representing the final state after ECAP processing in an average sense.

To be able to find a condition to compute the final laminate orientation in the general case the kinematics peculiar to the results obtained in Subsection 4.1.4 is analyzed first. So far, the geometry of the plastic deformation has been considered in terms of its atomistic interpretation. Now, atomistics are abandoned and a pure continuum view is at the focus of the subsequent investigation. What is illustrated in Figure 4.15 of Subsection 4.1.4 is the atomistic interpretation of the continuum deformation applied. Inspecting the plastic and elastic deformations of layer $+$ in Subsection 4.1.4 from a pure continuum perspective, it can be found that the plastic deformation induces a shear deformation of the originally horizontally aligned strip of the crystal plus a 90° positive rotation of the sheared layer. After that, the elastic deformation rotates the plastically deformed strip back to the horizontal orientation. Hence, in this case the plastic deformation can be formulated as a multiplicative decomposition of the form

$$\mathbf{F}^p = \mathbf{R}(\alpha) \mathbf{G}(\kappa), \quad (4.88)$$

where $\mathbf{R}(\alpha)$ is a proper orthogonal tensor, given by

$$\mathbf{R}(\alpha) = \begin{bmatrix} \cos \alpha & -\sin \alpha \\ \sin \alpha & \cos \alpha \end{bmatrix}$$

and the shear deformation corresponds to

$$\mathbf{G}(\kappa) = \mathbf{I} + \kappa \mathbf{e}_1 \otimes \mathbf{e}_2,$$

where $\alpha = \pi/2$ and $\kappa = 2$ in the case at hand. The elastic deformation is the pure rotation defined by

$$\mathbf{F}^e = \mathbf{R}(-\pi/2).$$

It can be found that the decomposition (4.88) is true for slip systems $\varphi \in (-\pi/2, 0)$ and situations, where $e(\gamma_{A,B}) = 0$. In more general situations, as encountered in the case with energy dissipation, such a relation is not valid, as the plastic deformation gets more complex. However, dealing with laminate orientations, the details of the actual mode of deformation due to plastic effects do not have to be known. What is of practical interest to the construction and the alignment of a 1st-order laminate is the angle between the direction of line elements horizontally aligned in their reference state and their push-forward counterpart. To see what that means, an illustration of the above relations for the results obtained for layer + in Subsection 4.1.4 applied to the edges of a unit square in its reference configuration is given in Figure 4.25. Since the de-

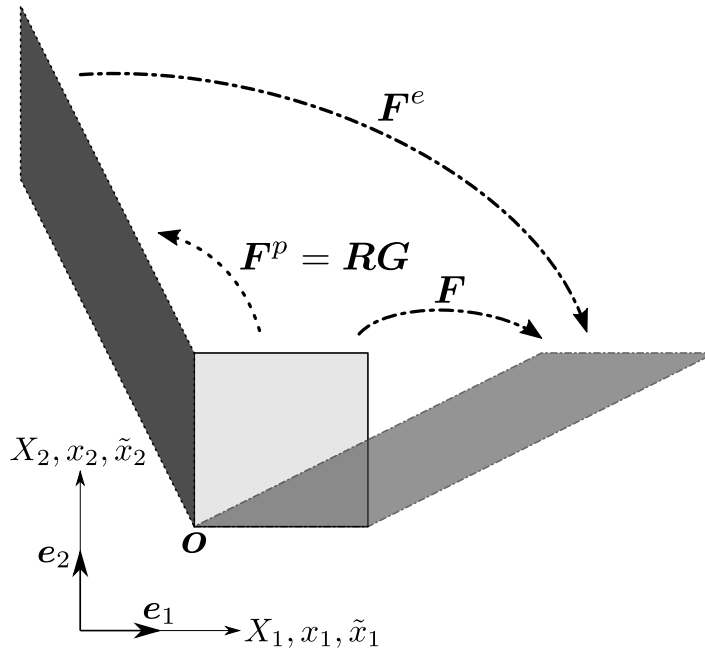


Figure 4.25: General continuum interpretation of the multiplicative decomposition of the deformation gradient $\mathbf{F} = \mathbf{F}^e \mathbf{F}^p$.

formation gradient considered here and in what follows is uniform, it is sufficient to investigate the deformation of a single line element originally oriented along the X_1 -axis, corresponding to the initial orientation of a strip of the undeformed layer. Then, the bottom and top edges of a unit square, as introduced in Figure 4.25, can be figured as the bottom and top edges of a laminate layer in its reference state. Thus, the final orientation after some overall deformation of a

laminate strip can be found from the successive application of the plastic and elastic deformations to a horizontal line element, as this allows for the computation of the signed angle between the initial line element and the plastically deformed unit vector as well as the signed angle taking this vector to its final orientation. The impact of the deformation for the case introduced before is shown in Figure 4.26, where on the left the plastic deformation takes the horizontal unit vector to a vertical position and on the right the elastic deformation rotates the plastically deformed line element back to the horizontal position. Therefore, the laminate orientation after the overall deformation coincides with the alignment in its reference configuration. Hence, the

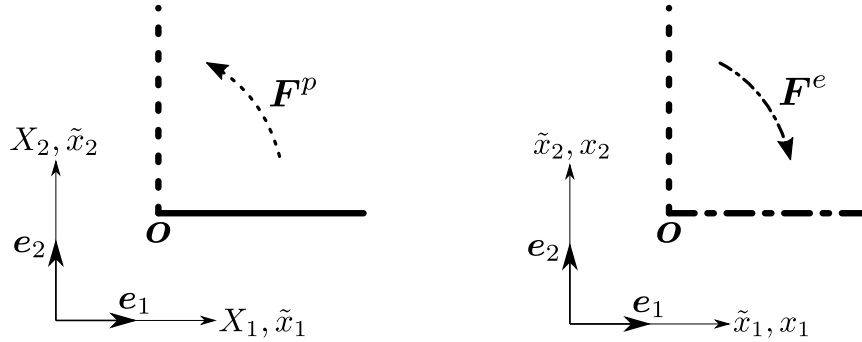


Figure 4.26: Successive application of the plastic and elastic deformations to an originally horizontally oriented line element of unit length.

final laminate orientation can be obtained as the push-forward of the unit normal \mathbf{N} to laminate layer — in its reference state according to Nanson's formula (3.12), given by

$$\mathbf{n} = \text{Cof } \mathbf{F}^- \mathbf{N} = \text{Cof } \mathbf{F}^{e-} \text{Cof } \mathbf{F}^{p-} \mathbf{N}, \quad (4.89)$$

which definitely is true for the results of Subsection 4.1.4. Actually, the same must be true applying the deformation \mathbf{F}^+ , since the laminate structure is formed by an arrangement of alternating parallel layers of type $-$ and $+$. It turns out for the case at hand with $\gamma^+ = 2$, $\beta^+ = -2$ and result (4.68)₂ that $\text{Cof } \mathbf{F}^p \mathbf{N} = [-1 \ 0]^T$ and $\text{Cof } \mathbf{F}^e [-1 \ 0]^T = [0 \ 1]^T$. Hence, the laminate orientation in the reference and the current configurations coincide, confirming the results obtained before, shown in Figures 4.25 and 4.26.

4.3.2 System Formulation and Solution Strategy

Employing the above observations via (4.89) and introducing a dissipation term in the free energy, indicating the resistance to dislocation motion, allows for the formation of 1st-order laminate structures of a prescribed orientation. The simplest type of rate-independent dissipation (4.14), introduced in Subsection 4.1.1, is modified defining K as a function of polynomial type, given by $K = K(\beta) = c_0 - c_1\beta$, implying a linear hardening behavior of the material. This yields a dissipation function of the form

$$D(\dot{\beta}) = K(\beta) |\dot{\beta}| = (c_0 - c_1\beta) |\dot{\beta}|, \quad (4.90)$$

where parameters c_0 and c_1 are not known a priori and are treated as part of the solution defining the 1st-order laminate. As before, the SVK and NH models are investigated in what follows.

The corresponding energy formulations are given as

$$\Psi^{SVK}(\mathbf{E}^e, \rho) = \frac{\lambda}{2} (\text{tr } \mathbf{E}^e)^2 + \mu \text{tr } (\mathbf{E}^e \mathbf{E}^e) - \mu \chi (\ln J^e)^3 + \mu c b^2 \rho + \left(c_0 \beta - \frac{1}{2} c_1 \beta^2 \right) \text{sgn } \dot{\beta} \quad (4.91)$$

and

$$\begin{aligned} \Psi^{NH}(\mathbf{C}^e, \rho) = & \frac{\mu}{2} (\text{tr } \mathbf{C}^e - 3) + \frac{\lambda}{4} \left[J^{e2} - 2 \left(1 + 2 \frac{\mu}{\lambda} \right) \ln J^e - 1 \right] + \mu c b^2 \rho \\ & + \left(c_0 \beta - \frac{1}{2} c_1 \beta^2 \right) \text{sgn } \dot{\beta} \quad (4.92) \end{aligned}$$

in the general case, respectively. Since $\beta = \beta(\gamma)$ is a monotonically decreasing function for $\gamma_A \leq \gamma \leq \gamma_B$ the dissipation terms in (4.91) and (4.92) are assigned a negative sign, stemming from the $\text{sgn } \dot{\beta}$ factor. Again, the solution for the unknown variables to construct the inclined laminate structure involves the minimization of the free energy, as outlined in Subsection 4.1.4. Obviously, the solution procedure becomes more intricate here, due to the unknown parameters c_0 and c_1 appearing in (4.91) and (4.92). In addition to that, the dissipational term gives rise to states $\gamma_{A,B}$ with $e(\gamma_{A,B}) \neq 0$ and a reinterpretation of the states $\gamma_{A,B}$ with regard to the laminate construction is needed. An outline of the solution strategy is given in what follows.

For the current model it is not possible anymore to obtain a solution for the construction of a laminate structure just using (4.20). It can be found that rank-1 connections have to be obtained assuming $\beta^\pm \neq \beta_{B,A}$, see Koster, Le and Nguyen (2015). Again, piecewise constant deformations \mathbf{F}^\pm are considered in the following computations. The deformation properties peculiar to states $\gamma_{A,B}$ and the corresponding $\beta_{A,B}$, pertaining to the construction of the lower convex hull $e^{\text{co}}(\gamma)$ of the energy function $e(\gamma)$, given in detail later, is preserved in the elastic stretch tensors

$$\mathbf{U}^{e\pm} = \sqrt{\mathbf{F}_{B,A}^{eT} \mathbf{F}_{B,A}^{eT}}. \quad (4.93)$$

The above relation (4.93) makes use of the decomposition of the elastic deformations $\mathbf{F}^{e\pm} = \mathbf{R}^{e\pm} \mathbf{U}^{e\pm}$, according to (3.17)₁, where the corresponding proper orthogonal tensors $\mathbf{R}^{e\pm}$ are given as

$$\mathbf{R}^{e\pm} = \begin{bmatrix} \cos \theta^\pm & -\sin \theta^\pm \\ \sin \theta^\pm & \cos \theta^\pm \end{bmatrix}.$$

The plastic deformations read

$$\mathbf{F}^{p\pm} = \mathbf{I} + \beta^\pm \mathbf{s} \otimes \mathbf{m},$$

as before, but the values of β^\pm now have to be obtained as part of the solution of an appropriate system of equations. Then, the overall deformation in laminate layers $+$ and $-$ can be determined via

$$\mathbf{F}^\pm = \mathbf{F}^{e\pm} \mathbf{F}^{p\pm}.$$

Accordingly, the system of equations to be solved to construct a 1st-order laminate is comprised of the compatibility condition (4.20), the macroscopic force equilibrium (4.30)₁, the thermodynamic equilibrium (4.31) and the geometric relation (4.89). What is more, the unit normal to laminate layer $-$ in the reference configuration is defined as $\mathbf{N} = [\cos \alpha \quad \sin \alpha]^T$, accounting

for condition $\|N\| = 1$ immediately, hence reducing the number of unknowns by one. Then, the corresponding set of nonlinear equations defining the desired 1st-order laminate is summarized as

$$\begin{aligned} \llbracket F \rrbracket &= q \otimes N, \\ \llbracket P \rrbracket N &= 0, \\ -q \cdot P^- N + \llbracket w \rrbracket &= 0, \\ n &= \text{Cof } F^- N, \end{aligned} \tag{4.94}$$

where states $(\bullet)^-$ have been chosen as unit normal N is defined on layer $-$. Actually, states $(\bullet)^+$ equally work here, as the laminate layers have the same orientation and the last two equations of (4.94) must be satisfied in both types of layers. Assuming a state of plane-strain deformation, this defines a system of 9 scalar equations for the unknown quantities θ^\pm , β^\pm , $q_{1,2}$, α as well as $c_{0,1}$, stemming from the dissipation function.

Having defined the equations governing the problem at hand, now the solution strategy is outlined. Recall the procedure introduced in Subsection 4.1.4, where the point of departure for the solution of the relevant equations was the minimization of the free energy with respect to the plastic slip β . Actually, the same approach remains valid here, but as the free energy depends on the unknown parameters c_0 and c_1 it is not possible to start with a minimization of the free energy immediately. To circumvent this issue, the strategy is as follows: as the ultimate goal is the solution of the system of nonlinear equations (4.94), involving the energy minimization of the free energy, a nested minimization procedure is employed to solve the set of nonlinear equations. The starting point is a redefinition of (4.94), using methods from optimization, see e.g. Nokedal and Wright (2006). The first step is to rewrite (4.94) in the form

$${}^1r(\bar{x}) = 0, \tag{4.95}$$

where the nonlinear system of equations is expressed as a vector of residuals ${}^1r(\bar{x})$, depending on the vector of unknowns $\bar{x} = [\theta^+ \ \theta^- \ \beta^+ \ \beta^- \ q_1 \ q_2 \ \alpha \ c_0 \ c_1]^T$. To find a solution to this set of equations (4.95) is interpreted in a least-squares sense, providing an objective function

$${}^1f = \sum_{i=1}^9 {}^1r_i^2(\bar{x}).$$

Then, the unconstrained minimization problem can be written as

$$\min_{\bar{x}} {}^1f. \tag{4.96}$$

Here, in contrast to a least-squares problem, the number of unknowns equals the number of scalar residuals, see e.g. Nokedal and Wright (2006). It has to be kept in mind that the minimization problem (4.96) cannot be solved immediately, as it requires the construction of the lower convex hull to $e(\gamma)$, needed to compute the elastic stretch tensors (4.93), which in turn are introduced in (4.94) via the elastic deformations $F^{e\pm}$. To see how to obtain the related system of nonlinear equations from Maxwell's construction, recall the generic function $J(u)$ and its derivative $J'(u)$, shown in Figures 4.4 and 4.5 of Subsection 4.1.3. Maxwell's rule of equal area postulates that if the constant function of $[J^{co}]' = m$, shown as dotted line in Figure 4.5, intersects $J'(u)$ in such a way that the areas enclosed by the line and $J'(u)$ are of equal size, then the tangent line of slope m touches $J(u)$ at the points of intersection $u_{A,B}$, providing the

lower convex hull $J^{\text{co}}(u)$. Computing both areas, exploiting the relation between $J(u)$ and $J'(u)$, and setting the difference equal to zero yields

$$J(u_B) - J(u_A) - m(u_B - u_A) = 0,$$

see e.g. Le (2010). In addition to that, the slope of the tangent line must be equal at both states $u_{A,B}$, giving

$$J'(u_A) = J'(u_B) = m.$$

Applying these results to the energy function, this corresponds to the nonlinear system of equations

$$\begin{aligned} e(\gamma_B) - e(\gamma_A) - m(\gamma_B - \gamma_A) &= 0, \\ e'(\gamma_A) &= m, \\ e'(\gamma_B) &= m, \end{aligned}$$

where the unknowns are γ_A , γ_B and m . Thus, the solution to Maxwell's construction can be formulated in the same spirit as before, where introducing the vector of residuals ${}^2\mathbf{r}(\bar{\mathbf{y}})$ and rewriting yields

$${}^2\mathbf{r}(\bar{\mathbf{y}}) = \mathbf{0}, \quad (4.97)$$

with $\bar{\mathbf{y}} = [\gamma_A(c_0, c_1) \quad \gamma_B(c_0, c_1) \quad m(c_0, c_1)]^T$. As indicated, one has to keep in mind that the solution to (4.97) depends on the parameters c_0 and c_1 . The corresponding objective function is given by

$${}^2f = \sum_{i=1}^3 {}^2r_i^2(\bar{\mathbf{y}})$$

and the minimization problem reads

$$\min_{\bar{\mathbf{y}}} {}^2f. \quad (4.98)$$

Hence, the construction of the 1st-order laminate sought can be obtained combining minimization problems (4.96) and (4.98), introduced before. The implementation was performed in MATLAB using a nested formulation, where the outer minimization corresponds to (4.96) and the inner minimization (4.98) provides the solution to Maxwell's construction. This procedure works iteratively, providing initial values $\bar{\mathbf{x}}_0$ and $\bar{\mathbf{y}}_0$ and defining ranges of the solution variables, where intrinsic MATLAB algorithms perform the actual minimization process. During the solution procedure the vector $\bar{\mathbf{x}}$ passes numerical values for c_0 and c_1 to vector $\bar{\mathbf{y}}$ to allow for the inner solution of equation (4.97), which is the first step of the nested minimization, needed to solve (4.95).

It turns out that there exist different types of solutions to the overall problem, i.e. vectors $\bar{\mathbf{x}}$, that satisfy (4.95) and yield different deformation characteristics of the resulting laminate structure. There exists one type of solution that exhibits deformation behavior similar to the results obtained in Subsection 4.1.4, where the deformation is prominent in laminate layer + and little deformation is found in layer -. What is more, the solution found agrees very well with the observations reported in Fukuda et al. (2003).

4.3.3 Inclined Laminate Structure

The result for the SVK model (4.91) in the case of plane-strain deformation, using (4.53) in system (4.94), is given as

$$\bar{\mathbf{x}}^{SVK} = \begin{bmatrix} -9.3509 \times 10^{-1} \\ -1.7424 \times 10^{-2} \\ -9.7411 \times 10^{-1} \\ 1.3565 \times 10^{-2} \\ 9.3625 \times 10^{-1} \\ 3.4012 \times 10^{-1} \\ 3.2478 \times 10^{-1} \\ 7.5 \times 10^{-2} \\ 1.0 \times 10^{-4} \end{bmatrix}, \quad \bar{\mathbf{y}}^{SVK} = \begin{bmatrix} 7.1729 \times 10^{-2} \\ 2.0768 \\ 7.5280 \times 10^{-2} \end{bmatrix}. \quad (4.99)$$

The resulting condensed energy plot is shown in Figure 4.27. It can be observed that the minima of the energy have been shifted due to the presence of the dissipation term, introduced via function (4.90) to the free energy. To obtain the lower convex hull $(e^{SVK})^{\text{co}}(\gamma)$ the associated shear stress function, depicted in Figure 4.28, must be employed. Clearly, the general

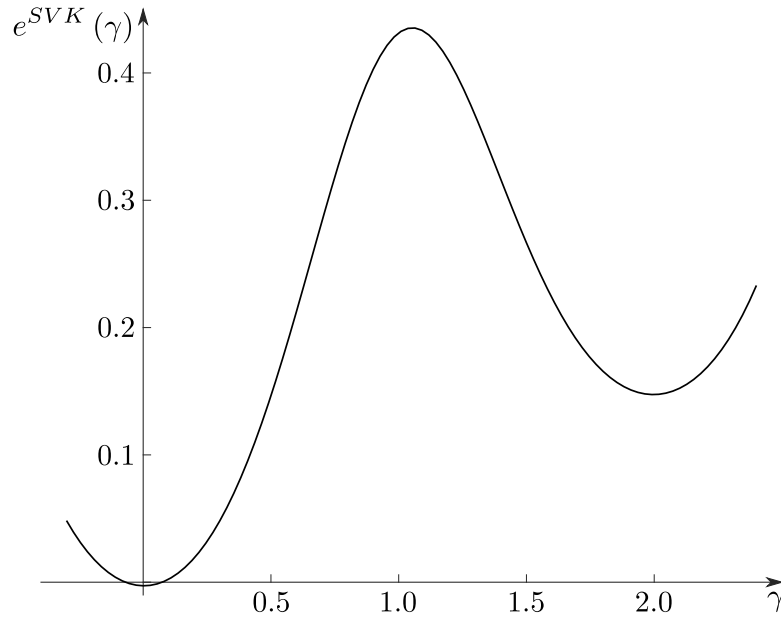


Figure 4.27: Nonconvex condensed energy plot for the SVK model with dissipation.

behavior is the same as seen in Figure 4.12, but the function has been shifted upwards. The corresponding Maxwell construction, combining information from both function plots, is illustrated in Figure 4.29, where the procedure has been outlined before and the relation between the tangent line to $e^{SVK}(\gamma)$ and the constant function is indicated using dotted lines on the interval $[\gamma_A, \gamma_B]$.

What is of interest now is the resulting 1st-order laminate structure. Thus, the details of the deformation of layers $+$ and $-$ are explored in detail in the following paragraphs. The first thing to observe, before giving a graphical representation of the final laminate structure, is the orientation of a generic strip cut from the crystal in its reference state, shown in Figure 4.30.

By definition, the unit normal N , prescribing the angle of inclination α , is associated with a strip of type $-$. Obviously, for a 1st-order laminate this orientation must pertain to both types

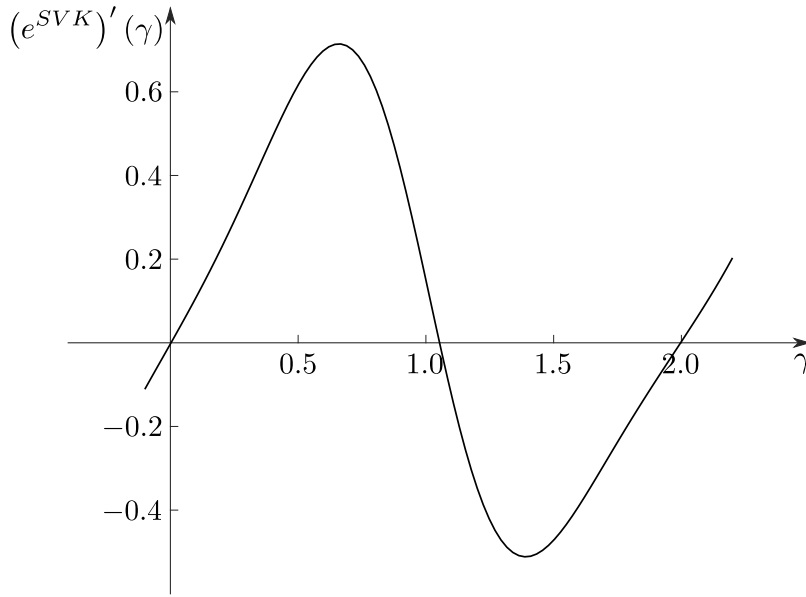


Figure 4.28: Shear stress plot for the SVK model with dissipation.

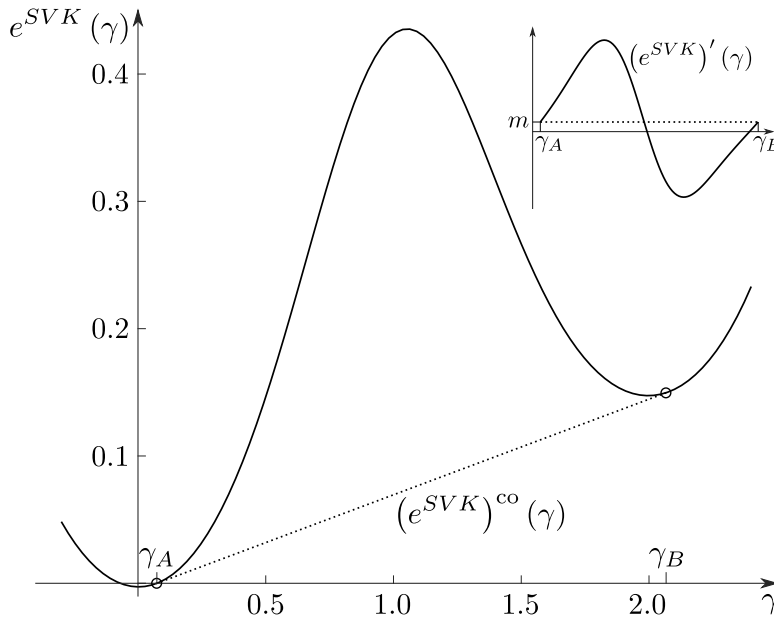


Figure 4.29: Maxwell's construction providing the lower convex hull of the nonconvex energy function for the SVK model with dissipation.

of layers. Here, it can be found that $\alpha = 18.6^\circ$, which is close to the final laminate orientation of 20° , prescribed via (4.89). Tracking the successive plastic and elastic deformations of a reference strip, applying $\mathbf{F}^\pm = \mathbf{F}^{e\pm} \mathbf{F}^{p\pm}$, gives the final geometry of both types of layers in their current configuration, illustrated in Figures 4.31 and 4.32. From the continuum point of view the plastic deformation of layer $+$ can be interpreted as a stretch, which is followed by a large elastic rotation and an elastic stretch. This amounts to a simple shear deformation

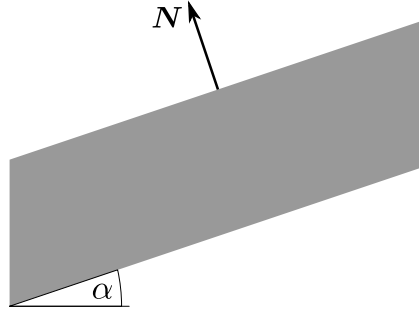


Figure 4.30: Orientation of a generic layer in its reference configuration for the SVK model with dissipation.

in the 20° direction. In layer $-$ only very small deformation can be observed. To find the volume fractions of both laminate layers it is important to note that the total deformations \mathbf{F}^\pm are simple shear deformations prescribed by the results of the minimization procedure outlined above. Thus, the definition of an average total deformation is not arbitrary, but must be such that it can be accommodated by the total deformations \mathbf{F}^\pm . Therefore, it turns out that an overall shear of $\gamma = \tan \pi/6$ in the bulk of the crystal is a reasonable assumption, to be described by a simple shear deformation

$$\tilde{\mathbf{F}}^{SVK} = \mathbf{I} + \tilde{\gamma}^{SVK} \mathbf{s}_{20^\circ} \otimes \mathbf{m}_{20^\circ}$$

in the direction of 20° , where $\mathbf{s}_{20^\circ} = [\cos \pi/9 \ \sin \pi/9]^\top$ and $\mathbf{m}_{20^\circ} = [-\sin \pi/9 \ \cos \pi/9]^\top$. The geometry of the above deformation can be seen in Figure 4.33, from which a shear of $\tilde{\gamma}^{SVK} = \cot 40^\circ - \cot 70^\circ$ can be concluded. From the relation for the average compatibility, see e.g. Bhattacharya (2003); Le (2010), given by

$$\tilde{\mathbf{F}}^{SVK} = s \mathbf{F}^+ + (1 - s) \mathbf{F}^-, \quad (4.100)$$

a volume fraction s of laminate layer $+$ with value 0.7625 can be obtained. In addition to that, it can be shown that

$$\begin{aligned} \text{Cof } \tilde{\mathbf{F}}^{SVK} &= s \text{Cof } \mathbf{F}^+ + (1 - s) \text{Cof } \mathbf{F}^-, \\ \det \tilde{\mathbf{F}}^{SVK} &= s \det \mathbf{F}^+ + (1 - s) \det \mathbf{F}^- \end{aligned} \quad (4.101)$$

also hold. Thus, the complete set of the minors relations, see Bhattacharya (2003), is satisfied, as required for a 1st-order laminate. The successive deformations of layers with the presumed volume fractions of s and $1 - s$ are illustrated in Figures 4.34 and 4.35, respectively. The associated arrangement for a set of layers $+$ and $-$ is shown in Figure 4.36.

The crystal sample in the reference configuration, whose bulk is divided into layers of type $+$ and $-$, exhibiting the respective volume fractions, is illustrated in Figure 4.37. Applying the total deformation $\tilde{\mathbf{F}}^{SVK}$ to the reference state gives the desired 1st-order laminate structure that satisfies compatibility in an average sense, as defined by relations (4.100) and (4.101). It can be seen that the transition between adjacent layers is not represented as a sharp interface, but there exists some transition zone which can be interpreted as a grain boundary. To be able to further characterize these boundaries, the misorientation between the resulting laminate layers is inspected below. This is done as follows: as the plastic deformations do not alter the shape

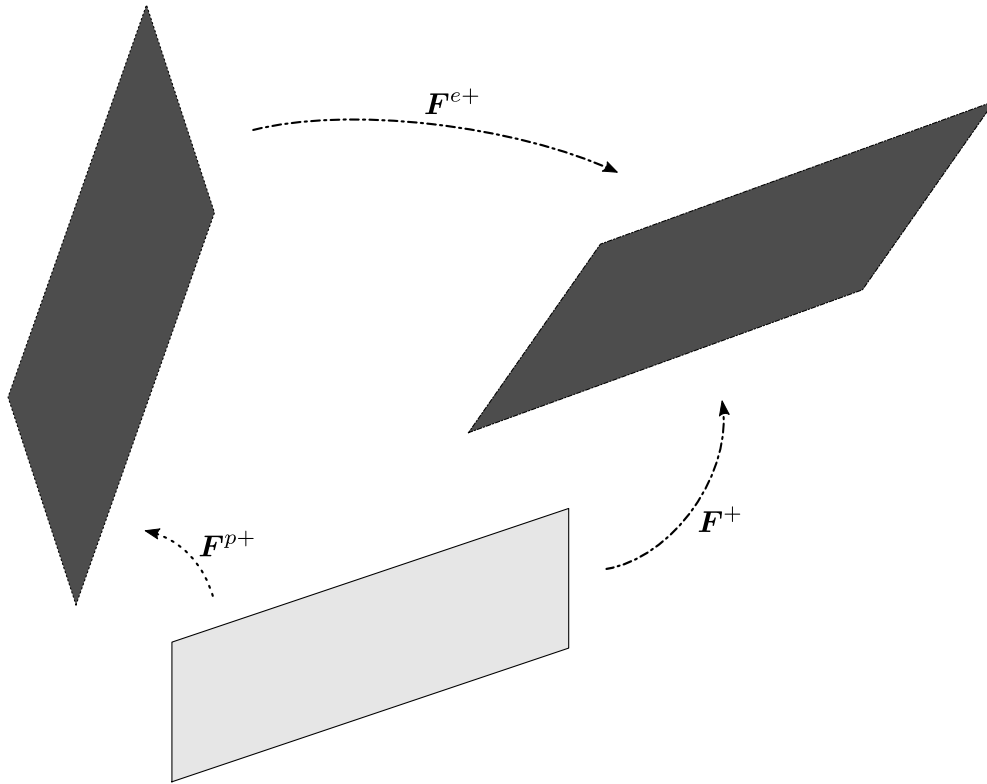


Figure 4.31: Successive deformation of layer + with unit volume for the SVK model with dissipation.

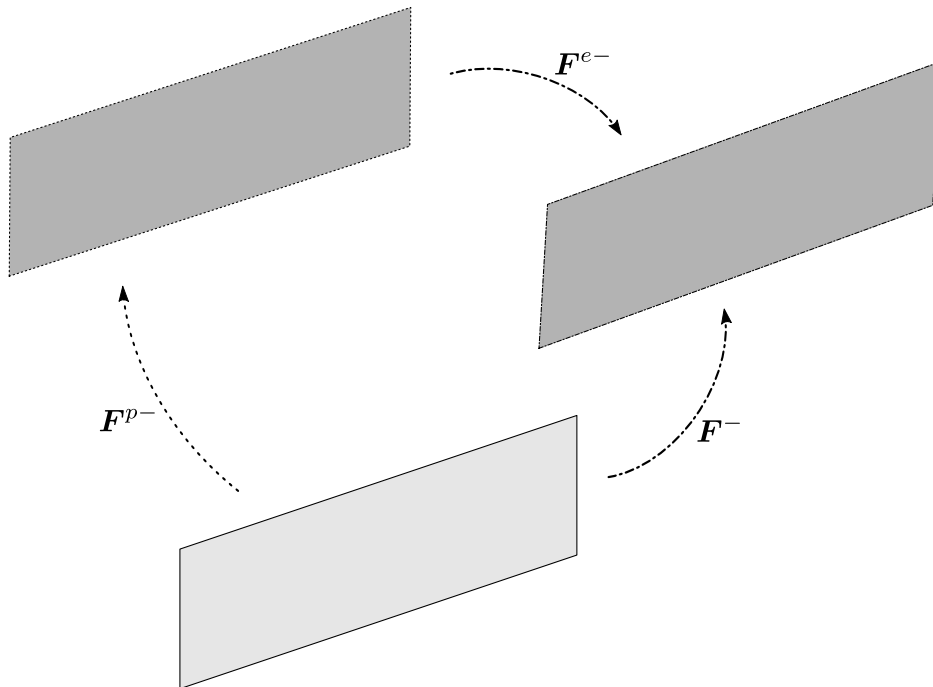


Figure 4.32: Successive deformation of layer - with unit volume for the SVK model with dissipation.

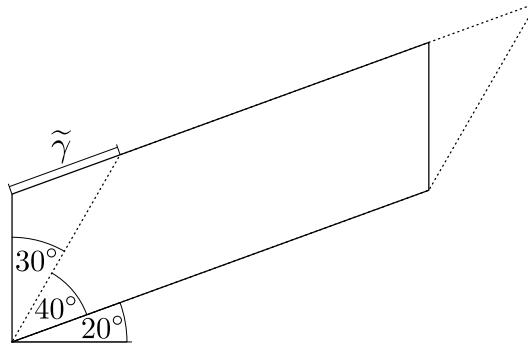


Figure 4.33: The geometry of $\tilde{\gamma}^{SVK}$ in the 20° direction.

and orientation of unit cells in the crystal lattice, the unit cells of both layers are compared after being exposed to the elastic deformations to get the angle of misorientation. The elastic deformation of a unit cell of layer +, shown in Figure 4.39, reveals that the unit cell is exposed to a large rotation and a stretch, successively. A unit cell of layer — is rotated and stretched, too, but its final shape and orientation just deviate slightly from the configuration after plastic deformation, as can be seen immediately from Figure 4.40.

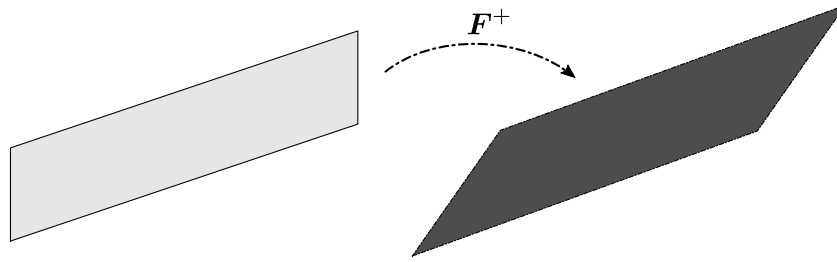


Figure 4.34: Total deformation of layer + with volume s for the SVK model with dissipation.

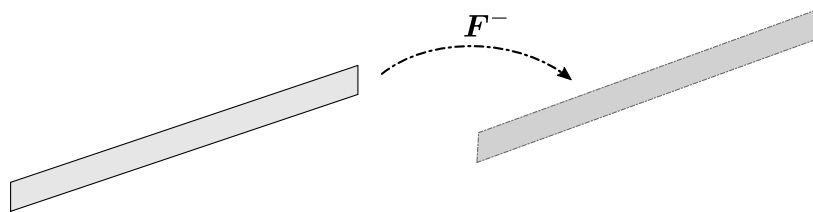


Figure 4.35: Total deformation of layer — with volume $1 - s$ for the SVK model with dissipation.

Hence, the misorientation can be measured as the angle between line elements whose orientation originally coincided in both layers. This yields an angle of misorientation of $\theta = 52.4^\circ$ for the laminate model at hand, depicted in Figure 4.41. The angle found must give rise to a large-angle grain boundary. To further analyze the nature of this grain boundary, refer to the below Figure 4.42. The illustration shows one pair of laminate layers of type + and —, respectively, with a detailed view of the atomic arrangement in the vicinity of the boundary. It reveals that the grain boundary obtained is an incoherent large-angle grain boundary, which can be seen when trying to match lattice positions from both lattices at an orientation of 20° . It can be found that there is no overlap of the lattices' Bravais sites.

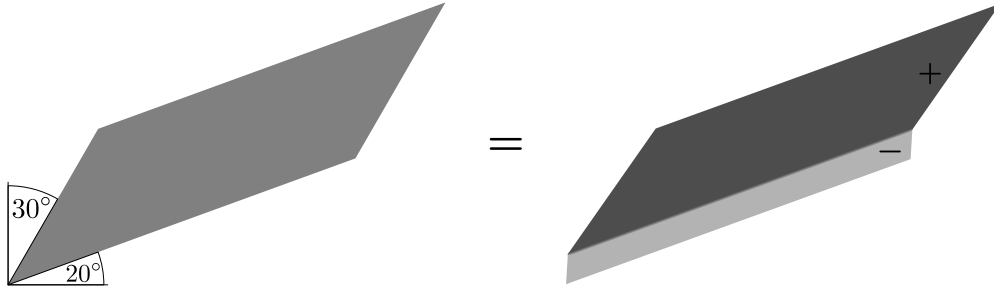


Figure 4.36: Average deformation $\tilde{\mathbf{F}}^{SVK} = s \mathbf{F}^+ + (1 - s) \mathbf{F}^-$.

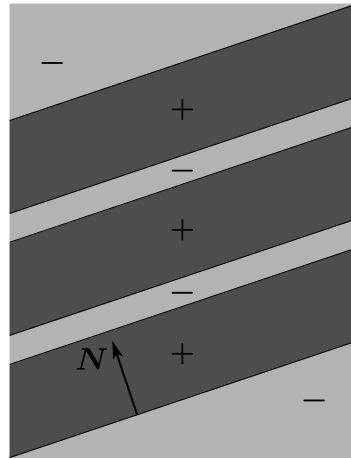


Figure 4.37: Crystal in its reference configuration with strips $+$ and $-$ having volume fractions s and $1 - s$, respectively, for the SVK model with dissipation.

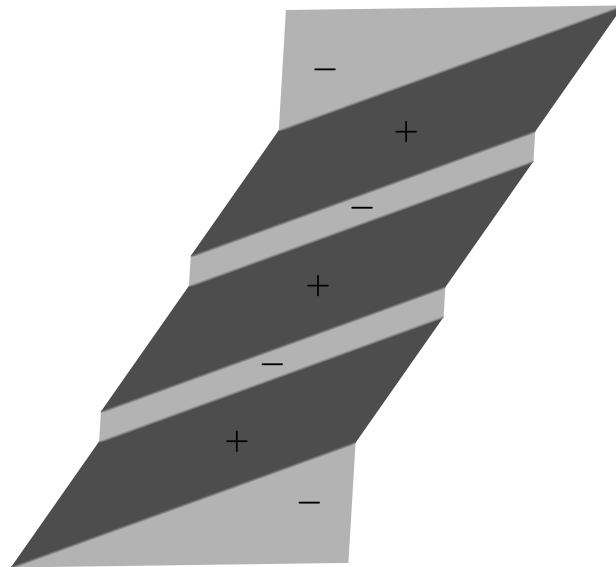


Figure 4.38: 1st-order laminate structure accommodating the deformation $\tilde{\mathbf{F}}^{SVK}$.

Finally, it can be stated that the above results clearly agree with what has been found in Subsection 4.1.4, where layer $+$ shows prominent deformation and layer $-$ does not deform at

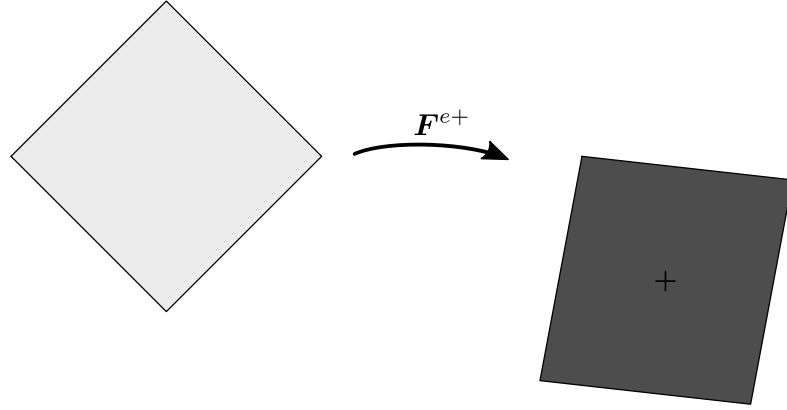


Figure 4.39: Distortion of a unit cell in the crystal lattice due to the elastic deformation F^{e+} for the SVK model with dissipation.

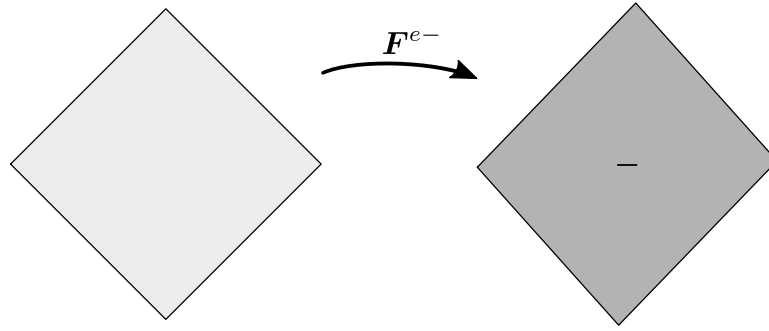


Figure 4.40: Distortion of a unit cell in the crystal lattice due to the elastic deformation F^{e-} for the SVK model with dissipation.

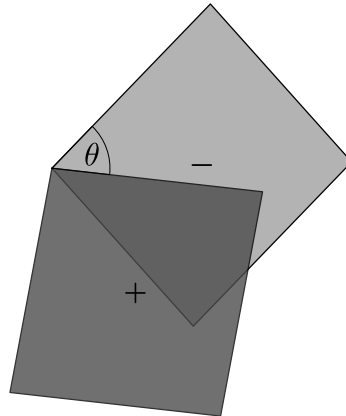


Figure 4.41: Angle of misorientation θ for the SVK model with dissipation.

all. For the current model a similar behavior can be found, where the deformation of layer + is large and, in contrast, layer — exhibits very little deformation. In addition to that, the results found here agree very well with the observations in Fukuda et al. (2003), showing the same orientation of striations, as well as a large angle of misorientation between the crystal lattices of the two species identified.

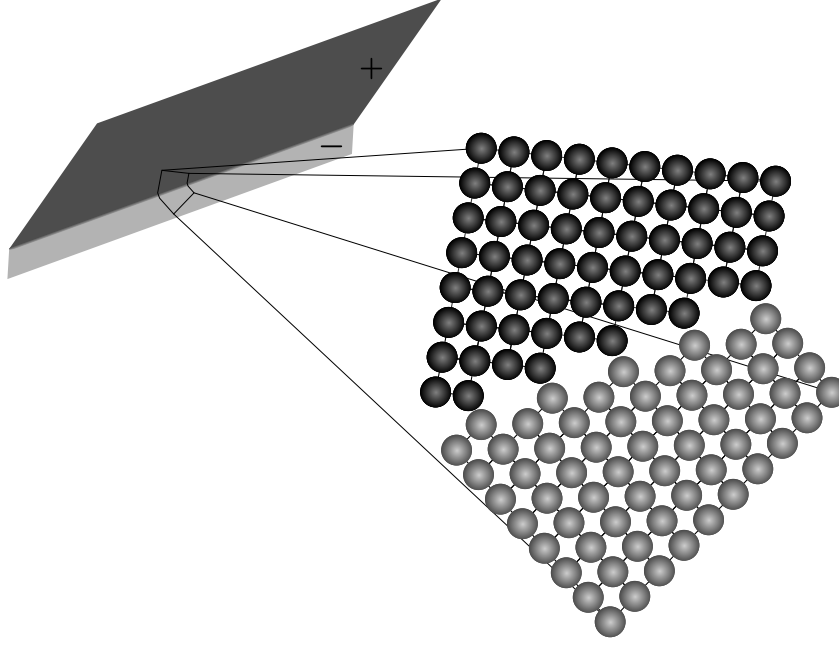


Figure 4.42: Incoherent large-angle grain boundary inclined at an angle of 20° for the SVK model with dissipation.

After having studied the SVK model in detail, what is of interest now is the behavior of the NH model, using the parameter values of $c_0 = 7.5 \times 10^{-2}$ and $c_1 = 1.0 \times 10^{-4}$, found before. The point of departure is the plane-strain version of (4.92), along with (4.57). Then, the solution vectors of (4.95) and (4.97) are given by

$$\bar{\mathbf{x}}^{NH} = \begin{bmatrix} -9.3305 \times 10^{-1} \\ -1.8930 \times 10^{-2} \\ -9.7087 \times 10^{-1} \\ 1.1530 \times 10^{-2} \\ 9.3307 \times 10^{-1} \\ 3.3851 \times 10^{-1} \\ 3.2462 \times 10^{-1} \\ 7.5 \times 10^{-2} \\ 1.0 \times 10^{-4} \end{bmatrix} \quad \text{and} \quad \bar{\mathbf{y}}^{NH} = \begin{bmatrix} 7.2105 \times 10^{-2} \\ 2.0778 \\ 7.5052 \times 10^{-2} \end{bmatrix}. \quad (4.102)$$

Comparison with the SVK model reveals that the results for both models are in very good agreement, where the differences between (4.99) and (4.102) are negligibly small. The condensed energy plot of the NH model, shown in Figure 4.43, exhibits the same qualitative behavior as the graph associated with the SVK model, where the minima virtually coincide with the ones depicted in Figure 4.27 and the maximum value is of lower magnitude here. This kind of behavior is also in agreement with the findings of Subsection 4.1.4. In addition to that, the shear stress plot, shown in the below Figure 4.44, reflects the behavior of the energy function discussed before. Eventually, Maxwell's rule of equal area provides the lower convex hull $(e^{NH})^{\text{co}}(\gamma)$, illustrated in Figure 4.45, following the same procedure as outlined before.

The corresponding 1st-order laminate virtually agrees with the laminate structure found for the SVK model. As the differences in the deformations resulting from the slight deviations in the solutions are very tiny, the resulting visualization of the deformed laminate layers and

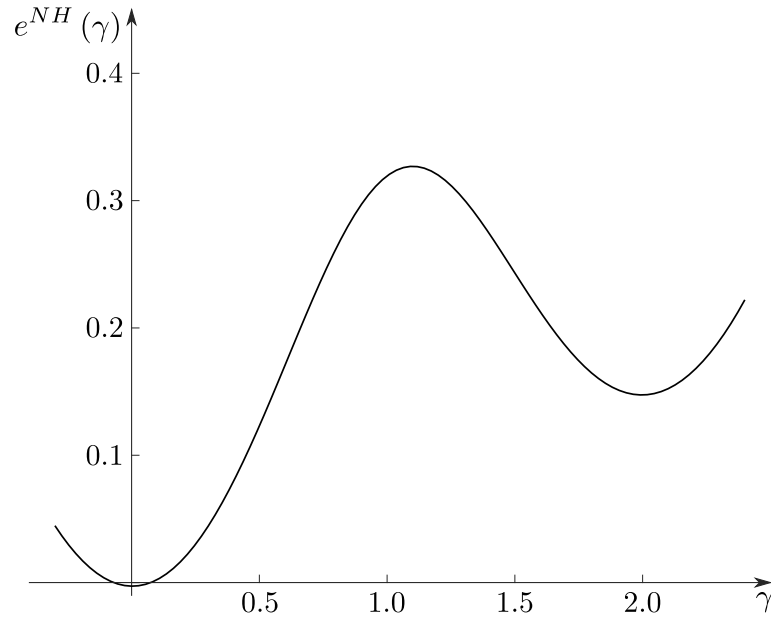


Figure 4.43: Nonconvex condensed energy plot for the NH model with dissipation.

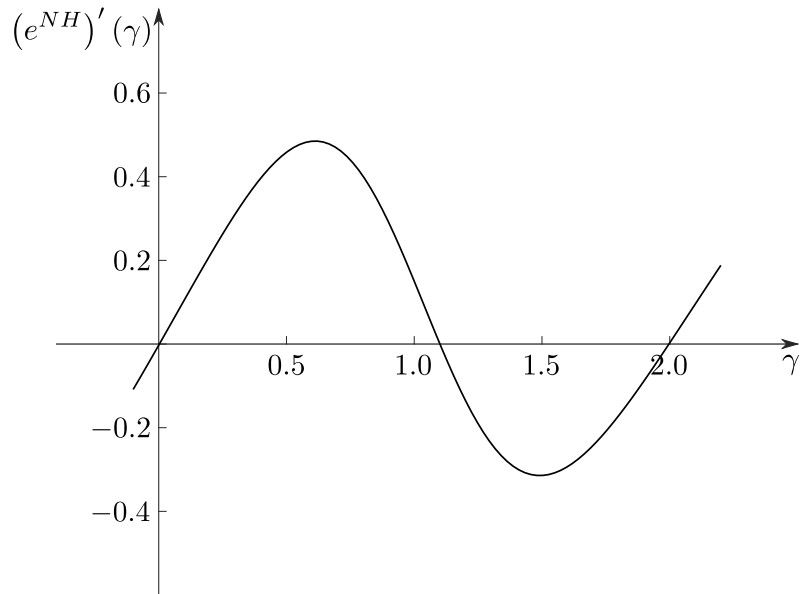


Figure 4.44: Shear stress plot for the NH model with dissipation.

unit cells for the NH model does not reveal any deviation from what is shown in Figures 4.30 through 4.42. Hence, the parameter values c_0 and c_1 identified for the SVK model equally work for the NH model and (4.90) can be interpreted as a Stage *I* hardening behavior, as introduced in the theory of hardening of FCC single crystals, discussed in Subsection 2.3. This also agrees with the assumption of a single active slip system, since easy glide is typically attributed to dislocation glide on just one slip system. What is more, the results obtained underpin the observations made for the models without dissipation in Subsection 4.1.4, where it turned out that the states $\gamma_{A,B}$, found from Maxwell's rule of equal area, are identical for the SVK and NH models.

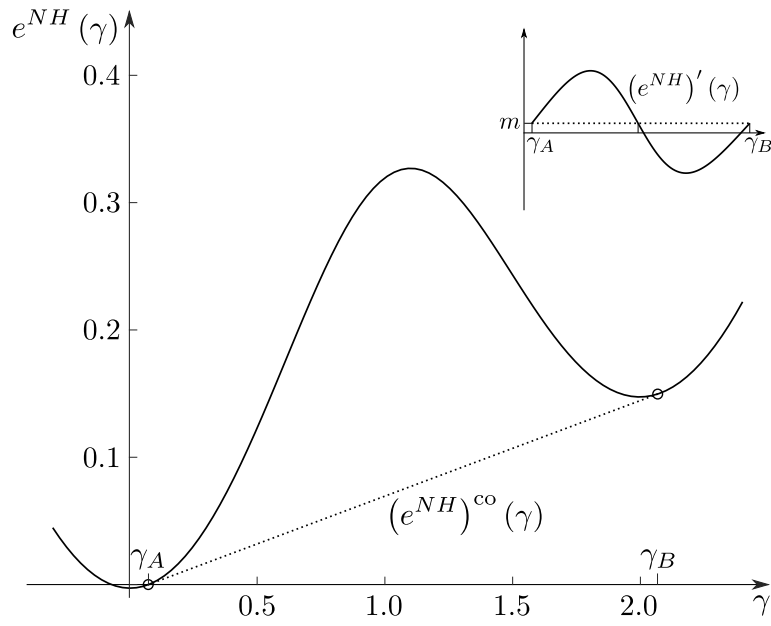


Figure 4.45: Maxwell's construction providing the lower convex hull of the nonconvex energy function for the NH model with dissipation.

5 Numerical Investigation

In this Chapter the numerical treatment of problems from nonlinear CDT is outlined in the framework of the finite element method. Up to now, the construction of laminate structures and the computation of finite-sized grain boundaries have been performed using analytical and semi-analytical procedures. To compare these results with numerical solutions a standard finite element approach is applied. Again, the investigations to be performed are based on both, the SVK and the NH material model, assuming a simple shear deformation of a single crystal containing a single active slip system. What is more, three different slip system orientations are considered. Opposed to standard computational models of finite-deformation single crystal plasticity, see e.g. de Souza Neto et al. (2008); Simo and Hughes (1998), the formulation used in what follows does not involve the explicit introduction of yield functions, evolution equations or loading and unloading criteria. Instead, the kinematics associated with the multiplicative decomposition of the deformation gradient (4.1), introduced in Subsection 4.1.1, in addition to the hyperelastic constitutive laws, defined in their general form in Subsection 4.1.2, serve as a basis for the numerical solution procedure.

5.1 Variational Formulation and Linearization

The finite element method is a means to find approximate solutions to partial differential equations (PDEs). The basic idea of the procedure is to provide a discretized version of the PDEs under investigation, transferring the continuous equations into a system of linear equations. These equations have to be solved for the degrees of freedom, defined at discrete points. Depending on the mathematical structure of the problem at hand, different strategies have to be employed to derive and eventually solve the discretized equations.

For the PDEs under investigation an iterative method of Newton-type is used, accounting for the nonlinearity of the theory. Thus, the linearization of the variational form of the nonlinear CDT model is needed, see e.g. Bonet and Wood (2008); Holzapfel (2000). A suitable point of departure for the derivation of the corresponding finite element formulation is the variational equation (4.25), where the left-hand side corresponds to the first variation of the energy functional (4.12), assuming there act no external loads at the boundary of the crystal. The actual energy density functions used are given by

$$\Psi^{SVK}(\mathbf{E}^e, \rho) = \frac{\lambda}{2} (\text{tr } \mathbf{E}^e)^2 + \mu \text{tr } (\mathbf{E}^e \mathbf{E}^e) - \mu \chi (\ln J^e)^3 + \frac{1}{2} \mu k \frac{\rho^2}{\rho_s^2} \quad (5.1)$$

and

$$\Psi^{NH}(\mathbf{C}^e, \rho) = \frac{\mu}{2} (\text{tr } \mathbf{C}^e - 3) + \frac{\lambda}{4} \left[J^{e2} - 2 \left(1 + 2 \frac{\mu}{\lambda} \right) \ln J^e - 1 \right] + \frac{1}{2} \mu k \frac{\rho^2}{\rho_s^2} \quad (5.2)$$

for the SVK and the NH model, respectively. In (5.1) and (5.2) the fields \mathbf{u} and β are the variables to be solved for. The procedure applied here is known as the total Lagrangian formulation,

where all quantities are derived with respect to the material description of the energy functional, see e.g. Reddy (2004). The first variation of the energy functional related to (5.1) and (5.2) with respect to the reference configuration yields

$$\delta I^{SVK,NH} = \int_{\Omega_0} [\mathbf{P}^{SVK,NH} : \delta \mathbf{F} - (\tau_r^{SVK,NH} + \varsigma) \delta \beta] dV = 0, \quad (5.3)$$

i.e. the variation is performed with respect to \mathbf{F} and β , according to (3.72) or (3.73). Since the variation of the second-order unit tensor \mathbf{I} equals zero and in virtue of (3.70) the variation of the total deformation $\delta \mathbf{F}$ can be replaced by the gradient of the variation of the displacement $\text{Grad } \delta \mathbf{u}$, see e.g. Holzapfel (2000). The expressions for the first Piola-Kirchhoff stress tensor in (5.3) are given as

$$\mathbf{P}^{SVK} = \mathbf{F}^e \left[\lambda (\text{tr} \mathbf{E}^e) \mathbf{I} + 2\mu \mathbf{E}^e - 3\mu\chi (\ln J^e)^2 \mathbf{C}^{e-1} \right] \mathbf{F}^{p-T} \quad (5.4)$$

and

$$\mathbf{P}^{NH} = \mathbf{F}^e \left\{ \mu \mathbf{I} + \frac{\lambda}{2} \left[J^{e2} - \left(1 + 2\frac{\mu}{\lambda} \right) \right] \mathbf{C}^{e-1} \right\} \mathbf{F}^{p-T}. \quad (5.5)$$

The resolved shear stress functions associated with the material models under investigation read

$$\tau_r^{SVK} = -\mathbf{s} \cdot \mathbf{C}^e \left[\lambda (\text{tr} \mathbf{E}^e) \mathbf{I} + 2\mu \mathbf{E}^e - 3\mu\chi (\ln J^e)^2 \mathbf{C}^{e-1} \right] \mathbf{F}^{p-T} \mathbf{m} \quad (5.6)$$

and

$$\tau_r^{NH} = -\mathbf{s} \cdot \mathbf{C}^e \left\{ \mu \mathbf{I} + \frac{\lambda}{2} \left[J^{e2} - \left(1 + 2\frac{\mu}{\lambda} \right) \right] \mathbf{C}^{e-1} \right\} \mathbf{F}^{p-T} \mathbf{m}. \quad (5.7)$$

It can be seen immediately that (5.4) through (5.7) must agree with the expressions found in Subsection 4.1.3. Obviously, the back stress obtained from the energy contribution of the dislocation network is identical for both models, yielding

$$\varsigma = \frac{\mu k}{(b\rho_s)^2} \nabla \cdot [(\nabla \beta \cdot \mathbf{s}) \mathbf{s}].$$

Introducing a time-like parameter that controls the deformation of the single crystal sample, the solution is obtained in a quasi-static setting. For the problem at hand equally-sized increments $\Delta(\bullet) = (\bullet)_n - (\bullet)_{n-1}$ are used, where the state of the system at $(\bullet)_{n-1}$ is assumed to be known. At each time step the solution is obtained in an iterative manner. The value of a variable at the i th iteration at step $(\bullet)_n$ is denoted $(\bullet)_n^i$ with the increment in the iterations $d(\bullet) = (\bullet)^{i+1} - (\bullet)^i$. Assuming the state of the system is known for some iteration i , then the solution can be found from solving the linearized system

$$\mathbf{R}(\Xi_{i+1}) = \mathbf{R}(\Xi_i) + D_{d\Xi, \delta\Xi}^2 \mathbf{I}(\Xi_i) d\Xi = 0. \quad (5.8)$$

In (5.8) $\mathbf{R} \equiv \delta I$ is the residual, obtained as the variation of the energy functional, Ξ is a vector containing the variables of the problem and $D_{d\Xi, \delta\Xi}^2 \mathbf{I}$ denotes the tangent matrix. Hence, the tangent can be defined in terms of the second variation of the energy functional or, equivalently, as the first variation of the residual, according to

$$D_{d\Xi, \delta\Xi}^2 \mathbf{I}(\Xi_i) = D_{d\Xi} \mathbf{R}(\Xi_i; \delta\Xi) =: \mathbf{K}(\Xi_i; d\Xi, \delta\Xi).$$

As the analytical derivation of the linearization in (5.8) is lengthy, an explicit expression is given here for the SVK material model, exclusively. The two contributions to the tangent matrix

$$\mathbf{K}(\Xi_i; d\Xi, \delta\Xi) = D_{d\mathbf{u}}\mathbf{R}(\Xi_i; \delta\Xi) d\mathbf{u} + D_{d\beta}\mathbf{R}(\Xi_i; \delta\Xi) d\beta,$$

arising from the linearization with respect to \mathbf{u} and β , respectively, are given by

$$\begin{aligned} D_{d\mathbf{u}}\mathbf{R}(\Xi_i; \delta\Xi) = & \int_{\Omega_0} \left[\text{Grad } \delta\mathbf{u} : \text{Grad } d\mathbf{u} \mathbf{S}^{SVK} + \mathbf{F}^T \text{Grad } \delta\mathbf{u} : \mathbb{C}^{SVK} : \mathbf{F}^T \text{Grad } d\mathbf{u} \right. \\ & + 3\mu\chi (\ln J^e)^2 \text{Grad } \delta\mathbf{u} : \text{Grad } d\mathbf{u} \mathbf{C}^{-1} + 3\mu\chi (\ln J^e)^2 \text{Grad}^T \delta\mathbf{u} \mathbf{F}^{-T} : \mathbf{F}^{-1} \text{Grad } d\mathbf{u} \\ & \left. - 6\mu\chi \ln J^e \text{Grad } \delta\mathbf{u} : \mathbf{F}^{-T} \mathbf{F}^{-T} : \text{Grad } d\mathbf{u} \right] dV \\ & + \int_{\Omega_0} \left[\delta\beta \mathbf{F}\mathbf{s} \otimes \mathbf{S}^{SVK} \mathbf{m} : \text{Grad } d\mathbf{u} + \delta\beta \mathbf{C}\mathbf{s} \otimes \mathbf{m} : \mathbb{C}^{SVK} : \mathbf{F}^T \text{Grad } d\mathbf{u} \right. \\ & + 3\mu\chi (\ln J^e)^2 \delta\beta \mathbf{F}\mathbf{s} \otimes \mathbf{C}^{-1} \mathbf{m} : \text{Grad } d\mathbf{u} + 3\mu\chi (\ln J^e)^2 \delta\beta \mathbf{F}^{-T} \mathbf{m} \otimes \mathbf{s} : \text{Grad } d\mathbf{u} \\ & \left. + \delta\beta \mathbf{P}^{SVK} \mathbf{m} \otimes \mathbf{s} : \text{Grad } d\mathbf{u} \right] dV \quad (5.9) \end{aligned}$$

and

$$\begin{aligned} D_{d\beta}\mathbf{R}(\Xi_i; \delta\Xi) = & - \int_{\Omega_0} \left[\text{Grad } \delta\mathbf{u} : \mathbf{F}\mathbf{s} \otimes \mathbf{S}^{SVK} \mathbf{m} d\beta + \mathbf{F}^T \text{Grad } \delta\mathbf{u} : \mathbb{C}^{SVK} : \mathbf{C}\mathbf{s} \otimes \mathbf{m} d\beta \right. \\ & + 3\mu\chi (\ln J^e)^2 \text{Grad } \delta\mathbf{u} : \mathbf{F}\mathbf{s} \otimes \mathbf{C}^{-1} \mathbf{m} d\beta + 3\mu\chi (\ln J^e)^2 \text{Grad } \delta\mathbf{u} : \mathbf{F}^{-T} \mathbf{m} \otimes \mathbf{s} d\beta \\ & \left. + \text{Grad } \delta\mathbf{u} : \mathbf{P}^{SVK} \mathbf{m} \otimes \mathbf{s} d\beta \right] dV \\ & - \int_{\Omega_0} \left[\delta\beta \mathbf{F}\mathbf{s} \cdot \mathbf{F}\mathbf{s} \mathbf{S}^{SVK} \mathbf{m} \cdot \mathbf{m} d\beta + \delta\beta \mathbf{C}\mathbf{s} \otimes \mathbf{m} : \mathbb{C}^{SVK} : \mathbf{C}\mathbf{s} \otimes \mathbf{m} d\beta \right. \\ & \left. + 3\mu\chi (\ln J^e)^2 \delta\beta \mathbf{F}\mathbf{s} \cdot \mathbf{F}\mathbf{s} \mathbf{C}^{-1} \mathbf{m} \cdot \mathbf{m} d\beta \right] dV + \frac{\mu k}{(b\rho_s)^2} \int_{\Omega_0} \text{Grad } \delta\beta \cdot \mathbf{s} \mathbf{s} \cdot \text{Grad } d\beta dV. \quad (5.10) \end{aligned}$$

Neglecting the variations with respect to β , the result for the hyperelastic model can be recovered, comprised of the first two terms in (5.9), corresponding to the geometrical and material contributions, respectively. The expression for the second Piola-Kirchhoff stress tensor \mathbf{S}^{SVK} in (5.9) and (5.10) is given as

$$\mathbf{S}^{SVK} = \mathbf{F}^{-1} \mathbf{P}^{SVK}.$$

What is more, the fourth-order material tensor \mathbb{C}^{SVK} is defined as

$$\mathbb{C}_{rqit}^{SVK} = \lambda F_{rd}^{p-1} F_{qd}^{p-1} F_{in}^{p-1} F_{tn}^{p-1} + \mu (F_{rj}^{p-1} F_{ij}^{p-1} F_{qn}^{p-1} F_{tn}^{p-1} + F_{rj}^{p-1} F_{tj}^{p-1} F_{qk}^{p-1} F_{ik}^{p-1}).$$

5.2 Finite Element Solution Procedure

To perform the numerical solution based on the finite element method the goal is to define a linear system of equations, where (5.8) can be rewritten as

$$\mathbf{K}(\Xi_i) d\Xi = -\mathbf{R}(\Xi_i),$$

which can be expressed in terms of the submatrices of \mathbf{K} , giving

$$\underbrace{\begin{bmatrix} \mathbf{K}_{uu} & \mathbf{K}_{u\beta} \\ \mathbf{K}_{\beta u} & \mathbf{K}_{\beta\beta} \end{bmatrix}}_{\mathbf{K}(\Xi_i)} \underbrace{\begin{bmatrix} d\mathbf{u} \\ d\beta \end{bmatrix}}_{d\Xi} = \underbrace{\begin{bmatrix} -\mathbf{R}_u(\mathbf{u}_i) \\ -\mathbf{R}_\beta(\beta_i) \end{bmatrix}}_{-\mathbf{R}(\Xi_i)}. \quad (5.11)$$

It has to be noted that the resulting system (5.11) is linear with respect to the incremental changes $d\mathbf{u}$ and $d\beta$. Applying the Galerkin finite element method, isoparametric shape functions of standard type are introduced to approximate the initial geometry and the unknown fields, see e.g. Bonet and Wood (2008). This provides interpolations of the form

$$\text{Grad } \mathbf{u} \approx \sum_I \text{Grad } \Phi^I \mathbf{u}^I, \quad \beta \approx \sum_I \Phi^I \beta^I, \quad \text{Grad } \beta \approx \sum_I \text{Grad } \Phi^I \beta^I, \quad (5.12)$$

where Φ and Φ denote vector-valued and scalar basis functions, respectively. The summation in (5.12) is performed over the number of degrees of freedom. The contributions of (5.11) are given by

$$\begin{aligned} {}^e\mathbf{K}_{uu}^{IJ} = & \int_{\Omega_{e,0}} \left[\text{Grad } \Phi^I : \text{Grad } \Phi^J \mathbf{S}^{SVK} + \mathbf{F}^T \text{Grad } \Phi^I : \mathbb{C}^{SVK} : \mathbf{F}^T \text{Grad } \Phi^J \right. \\ & + 3\mu\chi (\ln J^e)^2 \text{Grad } \Phi^I : \text{Grad } \Phi^J \mathbf{C}^{-1} + 3\mu\chi (\ln J^e)^2 \text{Grad}^T \Phi^I \mathbf{F}^{-T} : \mathbf{F}^{-1} \text{Grad } \Phi^J \\ & \left. - 6\mu\chi \ln J^e \text{Grad } \Phi^I : \mathbf{F}^{-T} \mathbf{F}^{-T} : \text{Grad } \Phi^J \right] dV, \quad (5.13) \end{aligned}$$

$$\begin{aligned} {}^e\mathbf{K}_{u\beta}^{IJ} = & - \int_{\Omega_{e,0}} \left[\text{Grad } \Phi^I : \mathbf{F} \mathbf{s} \otimes \mathbf{S}^{SVK} \mathbf{m} \Phi^J + \mathbf{F}^T \text{Grad } \Phi^I : \mathbb{C}^{SVK} : \mathbf{C} \mathbf{s} \otimes \mathbf{m} \Phi^J \right. \\ & + 3\mu\chi (\ln J^e)^2 \text{Grad } \Phi^I : \mathbf{F} \mathbf{s} \otimes \mathbf{C}^{-1} \mathbf{m} \Phi^J + 3\mu\chi (\ln J^e)^2 \text{Grad } \Phi^I : \mathbf{F}^{-T} \mathbf{m} \otimes \mathbf{s} \Phi^J \\ & \left. + \text{Grad } \Phi^I : \mathbf{P}^{SVK} \mathbf{m} \otimes \mathbf{s} \Phi^J \right] dV, \quad (5.14) \end{aligned}$$

$$\begin{aligned} {}^e\mathbf{K}_{\beta\beta}^{IJ} = & \int_{\Omega_{e,0}} \left[\Phi^I \mathbf{F} \mathbf{s} \otimes \mathbf{S}^{SVK} \mathbf{m} : \text{Grad } \Phi^J + \Phi^I \mathbf{C} \mathbf{s} \otimes \mathbf{m} : \mathbb{C}^{SVK} : \mathbf{F}^T \text{Grad } \Phi^J \right. \\ & + 3\mu\chi (\ln J^e)^2 \Phi^I \mathbf{F} \mathbf{s} \otimes \mathbf{C}^{-1} \mathbf{m} : \text{Grad } \Phi^J + 3\mu\chi (\ln J^e)^2 \Phi^I \mathbf{F}^{-T} \mathbf{m} \otimes \mathbf{s} : \text{Grad } \Phi^J \\ & \left. + \Phi^I \mathbf{P}^{SVK} \mathbf{m} \otimes \mathbf{s} : \text{Grad } \Phi^J \right] dV \quad (5.15) \end{aligned}$$

and

$$\begin{aligned} {}^e\mathbf{K}_{\beta\beta}^{IJ} = & - \int_{\Omega_{e,0}} \left[\Phi^I \mathbf{F} \mathbf{s} \cdot \mathbf{F} \mathbf{s} \mathbf{S}^{SVK} \mathbf{m} \cdot \mathbf{m} \Phi^J + \Phi^I \mathbf{C} \mathbf{s} \otimes \mathbf{m} : \mathbb{C}^{SVK} : \mathbf{C} \mathbf{s} \otimes \mathbf{m} \Phi^J \right. \\ & \left. + 3\mu\chi (\ln J^e)^2 \Phi^I \mathbf{F} \mathbf{s} \cdot \mathbf{F} \mathbf{s} \mathbf{C}^{-1} \mathbf{m} \cdot \mathbf{m} \Phi^J \right] dV + \frac{\mu k}{(b\rho_s)^2} \int_{\Omega_{e,0}} \text{Grad } \Phi^I \cdot \mathbf{s} \mathbf{s} \cdot \text{Grad } \Phi^J dV. \quad (5.16) \end{aligned}$$

The right-hand side of (5.11) is comprised of

$${}^e\mathbf{R}_u^I = \int_{\Omega_{e,0}} \text{Grad } \Phi^I : \mathbf{P}^{SVK} dV \quad (5.17)$$

and

$${}^e\mathbf{R}_\beta^I = - \int_{\Omega_{e,0}} \Phi^I (\tau_r^{SVK} + \varsigma) dV. \quad (5.18)$$

The integration of (5.13) to (5.18) is performed numerically on the reference element. Thus, a mapping relating the material and natural coordinates has to be established, introducing the Jacobian matrix of the transformation \mathbf{J}_e . Integration of the generic function $g(\mathbf{X})$ is performed as

$$\int_{\Omega_{e,0}} g(\mathbf{X}) dA = \int_{\Omega_{\square}} g(\boldsymbol{\xi}) \det \mathbf{J}_e(\boldsymbol{\xi}) d\boldsymbol{\xi} \approx \sum_{p=1}^{n_p} g(\boldsymbol{\xi}_p, \eta_p) \det \mathbf{J}_e(\boldsymbol{\xi}_p, \eta_p) W_p,$$

where the actual integration in the plane is approximated by a quadrature procedure with quadrature points $\boldsymbol{\xi}_p$ and weights W_p , see e.g. Wriggers (2001). To obtain a solution on the whole problem domain the contributions to the tangent matrix and residual must be assembled in an appropriate way, formally expressed as

$$\begin{aligned} \mathbf{K}_{uu}^i &= \mathbf{A}_e \sum_I \sum_J {}^e\mathbf{K}_{uu}^{IJ}, & \mathbf{K}_{u\beta}^i &= \mathbf{A}_e \sum_I \sum_J {}^e\mathbf{K}_{u\beta}^{IJ}, \\ \mathbf{K}_{\beta u}^i &= \mathbf{A}_e \sum_I \sum_J {}^e\mathbf{K}_{\beta u}^{IJ}, & \mathbf{K}_{\beta\beta}^i &= \mathbf{A}_e \sum_I \sum_J {}^e\mathbf{K}_{\beta\beta}^{IJ} \end{aligned}$$

and

$$\mathbf{R}_u^i = \mathbf{A}_e \sum_I {}^e\mathbf{R}_u^I, \quad \mathbf{R}_\beta^i = \mathbf{A}_e \sum_I {}^e\mathbf{R}_\beta^I.$$

5.3 Simple Shear Deformation

For the numerical computation a simple shear deformation of $\gamma = 0.2$ is applied to a single crystal sample of $1 \text{ mm} \times 1 \text{ mm}$ square shape, prescribed in terms of displacement boundary conditions. Plastic slip at the left and right boundaries of the sample are assumed to be equal to zero. The parameters are chosen according to what was defined in Subsection 4.2.2 and $\chi = 7.0 \times 10^{-3}$. The investigation performed in the current Section is meant as a basic study to give more insight into the behavior of the SVK and NH models in a simple numerical setting. It turns out that for slip system orientations $\varphi \in (-\pi/2, 0)$ the Newton procedure seems not to achieve convergence, which agrees with the findings of Subsection 4.1.4, stating that in this range of slip system orientations the energy turns nonconvex, probably leading to problems in the numerical solution process. Therefore, the slip system orientation is chosen from the range $\varphi \in (0, \pi/2)$, where the results for the plastic slip variable β for the SVK model are shown in Figures 5.1 to 5.3 for slip system orientations of $\varphi = 25^\circ$, $\varphi = 65^\circ$ and $\varphi = 85^\circ$, respectively, plotted on the undeformed geometry. It can be found from a qualitative point of view that the patterns of the plastic slip distribution are quite different for distinct slip system orientations. When inspecting the Figures it has to be noted that the color scales chosen are different.

For a slip system orientation of $\varphi = 25^\circ$ there forms an area, where the plastic slip attains its maximum magnitude, approximately inclined at the angle φ , corresponding to the red strip in Figure 5.1. What is more, there seems to exist some symmetry in plastic slip, inspecting the regions above and below the red portion of the plot. In the case of $\varphi = 65^\circ$, illustrated in Figure 5.2, the parts of the domain of the plot having the highest magnitude of plastic slip again can be found inclined at an angle approximately corresponding to the slip system orientation. At the orientation investigated here, actually two separate regions form. Again the plastic slip

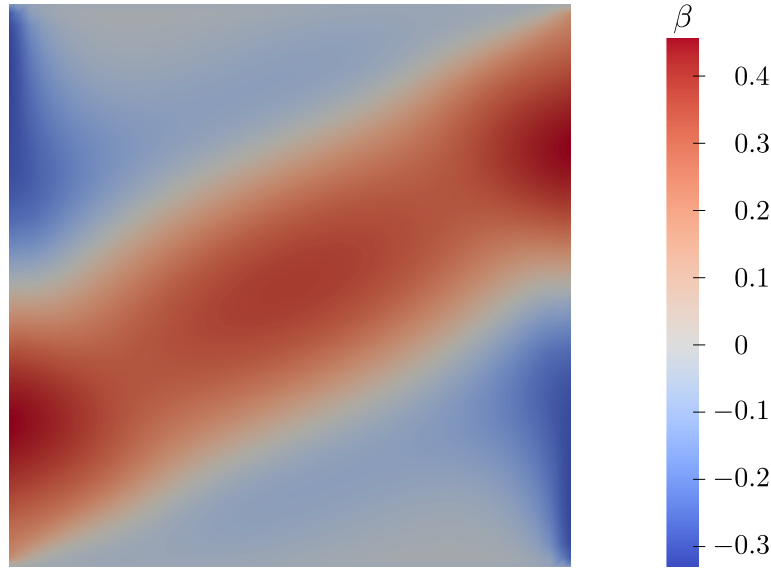


Figure 5.1: Plastic slip distribution for a slip system orientation of $\varphi = 25^\circ$ using the SVK model.

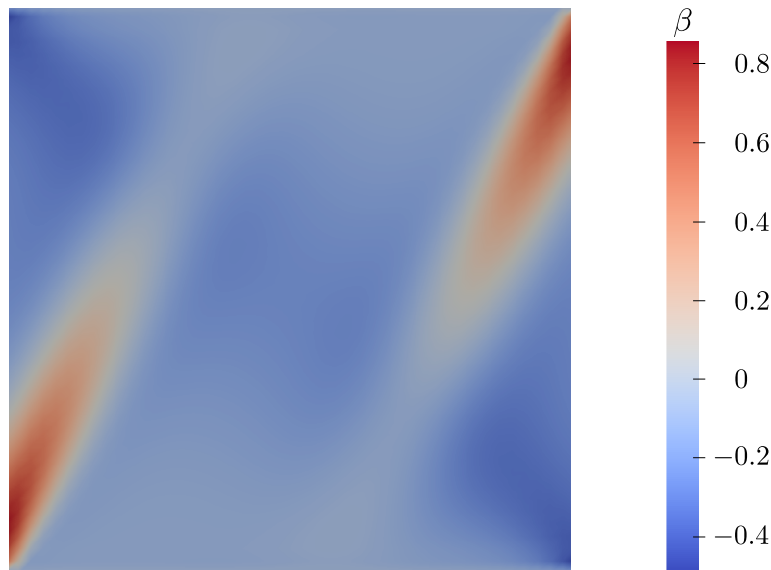


Figure 5.2: Plastic slip distribution for a slip system orientation of $\varphi = 65^\circ$ using the SVK model.

evolves in a symmetric way. Eventually, Figure 5.3 again reveals symmetry in the distribution of plastic slip, where in this case the largest magnitude of plastic slip can be observed in the top left and bottom right corners of the specimen. Here, the areas inclined at an angle of approximately φ exhibit the lowest magnitude of plastic slip.

Hence, it can be found that for the situation of simple shear analyzed in this Section a clear relation between the choice of slip system and the resulting distribution of plastic slip in the final state of equilibrium may be established. The analytical derivation of the linearization, given in (5.13) through (5.18) can be verified using an automatic linearization algorithm, exhibiting the same convergence characteristics and results as shown in the above Figures.

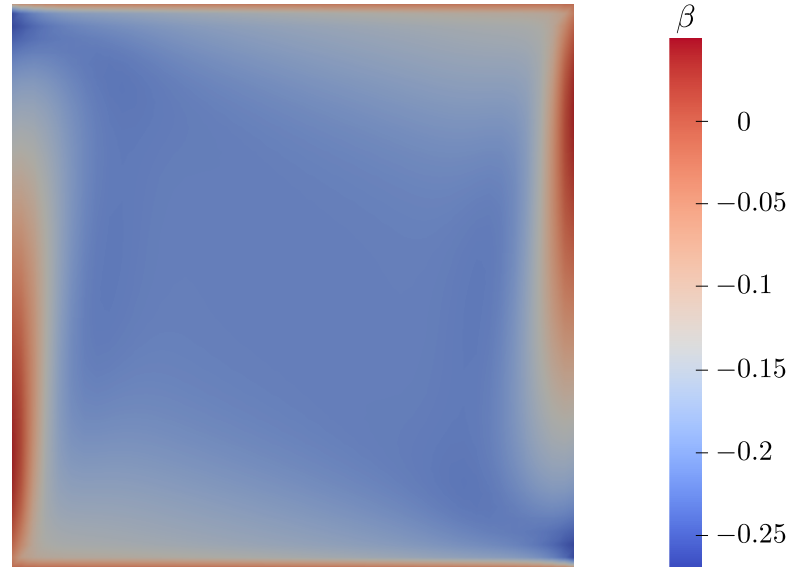


Figure 5.3: Plastic slip distribution for a slip system orientation of $\varphi = 85^\circ$ using the SVK model.

As stated before, the analytical expression of the linearization is given just for the SVK model. The implementation of the NH version was performed under the same conditions as chosen before, using automatic differentiation. The corresponding results are shown in the below Figures 5.4 to 5.6. It can be seen immediately that there are no discrepancies in the results obtained compared with the plots shown before. The qualitative behavior is exactly as observed for the SVK model and differences in the numerical values of plastic slip are negligibly small.

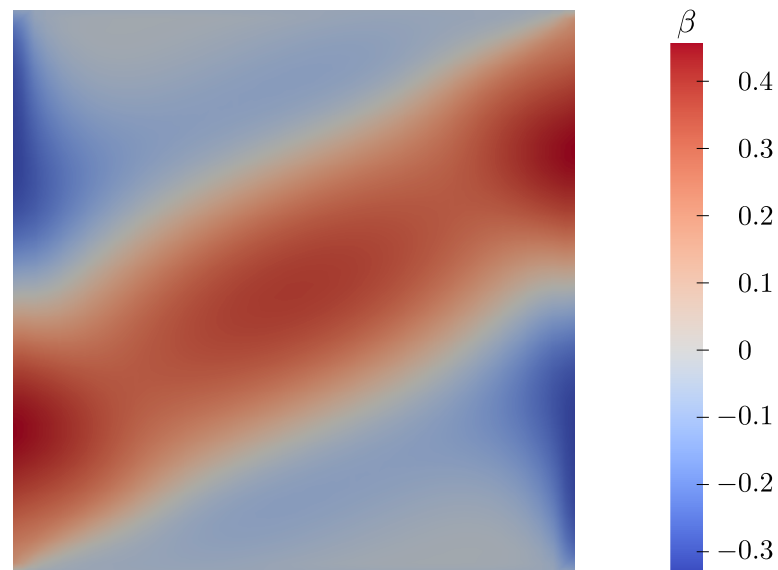


Figure 5.4: Plastic slip distribution for a slip system orientation of $\varphi = 25^\circ$ using the NH model.

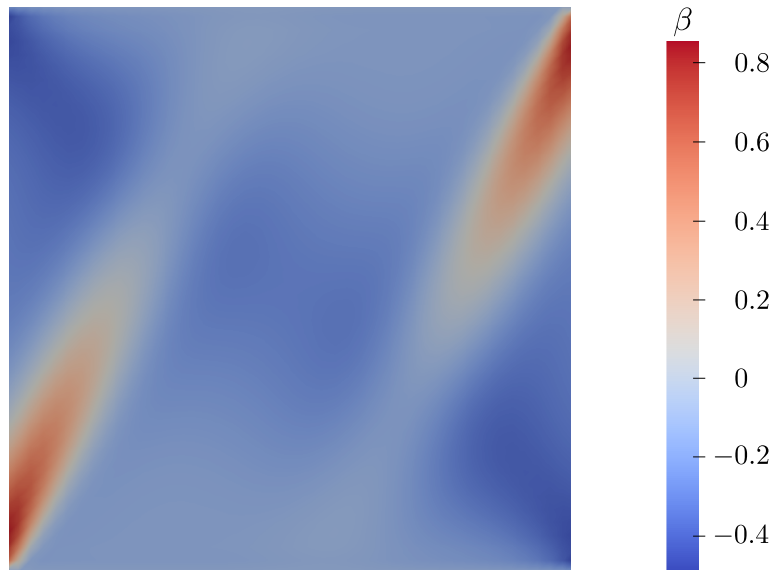


Figure 5.5: Plastic slip distribution for a slip system orientation of $\varphi = 65^\circ$ using the NH model.

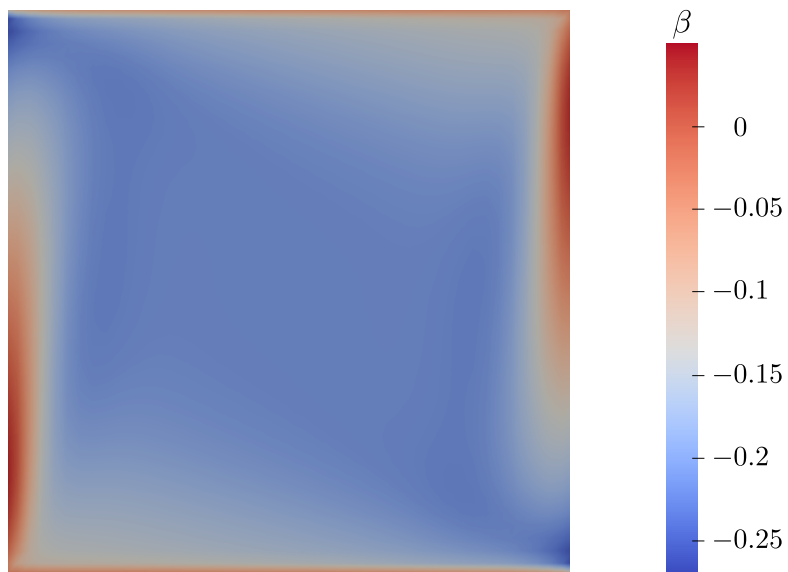


Figure 5.6: Plastic slip distribution for a slip system orientation of $\varphi = 85^\circ$ using the NH model.

6 Final Remarks and Outlook

The goal of this thesis was to investigate different approaches to mimicking the formation of grain boundaries in single crystals, based on nonlinear CDT. It was shown that the theory is capable to model the formation of horizontally aligned grain boundaries as sharp interfaces. It turned out that different energy formulations equally qualify as candidates in nonlinear CDT, where from the physical interpretation the SVK model is the more appropriate choice for the investigation of metals, exhibiting large deformations and small strains. From a mathematical point of view the NH energy in general performs better in computations than the SVK version. When considering the enhanced model with grain boundaries of small but finite thickness, the results obtained for both energy formulations were similar, but did not coincide, as in the construction of 1st-order laminates. In the investigation of inclined laminate layers again both models worked equally well with regard to the solutions obtained. From the computational point of view it became apparent that the energy minimization process for the NH model was much faster than in the SVK case.

The numerical approach using the finite element method, obtained from the hyperelastic energy formulation and taking into account the energy of the dislocation network, provides a different view on things. In this case the formulation takes into account the gradient of the plastic slip, as opposed to the description used for 1st-order laminate structures. What is more, the variables evolve freely in the bulk of the crystal sample in a quasi-static sense, not being subject to kinematical constraints. Here, no difference was found in the results obtained for both material models.

Thus, various ways to model microstructure formation in ductile single crystals deforming in single slip were investigated and gave insight into the various perspectives offered by nonlinear CDT.

An idea for the extension of the analyses performed in this thesis is the combination of two of the above mentioned approaches. Solving the model with dissipation as a time-dependent problem in a numerical setting, e.g. using the framework of the finite element method, results in a phase field formulation. Then, the numerical solution allows to trace the evolution of the variables over time. This may be a step towards a realistic simulation of the evolution and formation of grain boundaries, allowing for a more detailed comparison with experimental studies.

References

- Antman, S. S., 1979. The eversion of thick spherical shells. *Arch. Ration. Mech. Anal.* 70, 113-123.
- Argon, A. S., 2008. *Strengthening Mechanisms in Crystal Plasticity*. Oxford University Press, Oxford.
- Ball, J. M., 1977. Convexity conditions and existence theorems in nonlinear elasticity. *Arch. Ration. Mech. Anal.* 63, 337-403.
- Berdichevsky, V. L., 2006a. On thermodynamics of crystal plasticity. *Scr. Mater.* 54, 711-716.
- Berdichevsky, V. L., 2006b. Continuum theory of dislocations revisited. *Continuum Mech. Therm.* 18, 195-222.
- Berdichevsky, V. L., Le, K. C., 2002. Theory of charge nucleation in two dimensions. *Phys. Rev. E* 66 (2), 026129.
- Berdichevsky, V. L., Le, K. C., 2007. Dislocation nucleation and work hardening in anti-plane constrained shear. *Continuum Mech. Therm.* 18, 455-467.
- Bhattacharya, K., 2003. *Microstructure of Martensite. Why it Forms and How it Gives Rise to the Shape-Memory Effect*. Oxford University Press, Oxford.
- Bilby, B. A., Gardner, L. R. T., Stroh, A. N., 1957. Continuous distributions of dislocations and the theory of plasticity. In: *Extrait des actes du IX^e congrès international de mécanique appliquée*, 35-44.
- Bonet, J., Wood, R. D., 2008. *Nonlinear Continuum Mechanics for Finite Element Analysis*. Cambridge University Press, New York, 2nd edition.
- Borja, R. I., 2013. *Plasticity. Modeling & Computation*. Springer, New York.
- Brünig, M., 1999. Numerical simulation of the large elastic-plastic deformation behavior of hydrostatic stress-sensitive solids. *Int. J. Plasticity* 15 (11), 1237-1264.
- Bulatov, V. V., Cai, W., 2006. *Computer Simulations of Dislocations*. Oxford University Press, Oxford.
- Cahn, J. W., Hilliard, J., 1958. Free energy of a nonuniform system. I. interfacial free energy. *J. Chem. Phys.* 28, 258-267.
- Carstensen, C., Hackl, K., Mielke, A., 2002. Non-convex potentials and microstructures in finite-strain plasticity. *Proc. Royal Soc. Lond. A* 458, 299-317.
- Chen, L. Q., 2002. Phase-field models for microstructure evolution. *Annu. Rev. Mater. Res.* 32, 113-140.

- Ciarlet, P. G., Geymonat, G., 1982. Sur les lois de comportement en élasticité non-linéaire compressible, C. R. Acad. Sci. Paris Sér. II 295, 423-426.
- Ciarlet, P. G., 1988. Mathematical Elasticity. Volume 1: Three Dimensional Elasticity. Elsevier B. V., Amsterdam.
- Christian, J. W., Mahajan, S., 1995. Deformation twinning. Prog. Mater. Sci. 39 (1), 1-157.
- Coleman, B. D., Noll, W., 1959. On the thermostatics of continuous media. Arch. Rat. Mech. Anal. 4, 97-128.
- Dacorogna, B., 2008. Direct Methods in the Calculus of Variations. Springer, New York, 2nd edition.
- de Souza Neto, E. A., Perić, D., Owen, D. R. J., 2008. Computational Methods for Plasticity. Theory and Applications. John Wiley & Sons Ltd., Chichester.
- Diehl, J., 1956. Zugverformung von Kupfer-Einkristallen. Z. Metallkd. 47, 331-343.
- Dmitrieva, O., Dondl, P., Müller, S., Raabe, D., 2009. Lamination microstructure in shear deformed copper single crystals. Acta Mater. 57, 3439-3449.
- Dolzmann, G., 2003. Variational Methods for Crystalline Microstructure – Analysis and Computation. Springer-Verlag, Berlin.
- Engels, P., Ma, A., Hartmaier, A., 2012. Continuum simulation of the evolution of dislocation densities during nanoindentation. Int. J. Plasticity 38, 159-169.
- Flanigan, F. J., Kazdan, J. L., 1990. Calculus Two. Linear and Nonlinear Functions. Springer, New York.
- Fleming, W., 1977. Functions of Several Variables. Springer, New York, 2nd edition.
- Fox, C., 1963. An Introduction to the Calculus of Variations. Dover Publications Inc., New York.
- Fukuda, Y., Oh-ishi, K., Furukawa, M., Horita, Z., Langdon, T. G., 2003. The application of equal-channel angular pressing to an aluminum single crystal. Acta Mater. 52, 1387-1395.
- Fukuda, Y., Oh-ishi, K., Furukawa, M., Horita, Z., Langdon, T. G., 2006. Influence of crystal orientation on ECAP of aluminum single crystals. Mater. Sci. Eng. A 420 (1), 79-86.
- Gelfand, I. M., Fomin, S. V., 1963. Calculus of Variations. Dover Publications Inc., New York.
- Gonzalez, O., Stuart, A. M., 2008. A First Course in Continuum Mechanics. Cambridge University Press, New York.
- Gurtin, M. E., 1981. An Introduction to Continuum Mechanics. Academic Press, New York.
- Gurtin, M. E., Fried, E., Anand, L., 2010. The Mechanics and Thermodynamics of Continua. Cambridge University Press, New York.
- Hansen, N., Kuhlmann-Wilsdorf, D., 1986. Low energy dislocation structures due to unidirectional deformation at low temperatures. Mater. Sci. Eng. 81, 141-161.
- Hansen, N., 2004. Hall–Petch relation and boundary strengthening. Scr. Mater. 51 (8), 801-806.

- Harren, S. V., Deve, H. E., Asaro, R. J., 1988. Shear band formation in plane strain compression. *Acta Metall.* 36 (9), 2435-2480.
- Hirth, J. P., Lothe, J., 1982. *Theory of Dislocations*. Krieger Publishing Company, Malabar, Florida, 2nd edition.
- Hirth, J. P., 1985. A brief history of dislocation theory. *Metall. Trans.* 16 A, 2085-2090.
- Holzappel, G. A., 2000. *Nonlinear Solid Mechanics. A Continuum Approach for Engineering*. John Wiley & Sons Inc., Chichester.
- Hughes, D. A., Hansen, N., 1997. High angle boundaries formed by grain subdivision mechanisms. *Acta Mater.* 45 (9), 3871-3886.
- Hull, D., Bacon, D. J., 2011. *Introduction to Dislocations*. Butterworth-Heinemann, Oxford, 5th edition.
- Ibrahimbegovic, A., 2009. *Nonlinear Solid Mechanics. Theoretical Formulations and Finite Element Solution Methods*. Springer, New York.
- Janssens, K. G. F., Raabe, D., Kozeschnik, E., Miodownik, M. A., Nestler, B., 2007. *Computational Materials Engineering. An Introduction to Microstructure Evolution*. Academic Press, Oxford.
- Jia, D., Ramesh, K. T., Ma, E., 2003. Effects of nanocrystalline and ultrafine grain sizes on constitutive behavior and shear bands in iron. *Acta Mater.* 51 (12), 3495-3509.
- Jiang, B., Weng, G. J., 2004. A generalized self-consistent polycrystal model for the yield strength of nanocrystalline materials. *J. Mech. Phys. Solids* 52 (5), 1125-1149.
- Kaluza, M., Le, K. C., 2011. On torsion of a single crystal rod. *Int. J. Plasticity* 27, 460-469.
- Khan, A. S., Huang, S., 1995. *Continuum Theory of Plasticity*. John Wiley & Sons Inc., New York.
- Kochmann, D. M., Le, K. C., 2008a. Plastic deformation of bicrystals within continuum dislocation theory. *J. Math. Mech. Solids* 14, 540-563.
- Kochmann, D. M., Le, K. C., 2008b. Dislocation pile-ups in bicrystals within continuum dislocation theory. *Int. J. Plasticity* 24, 2125-2147.
- Kochmann, D. M., Le, K. C., 2009. A continuum model for the initiation and evolution of deformation twins. *J. Mech. Phys. Solids* 57, 987-1002.
- Kochmann, D. M., Hackl, K., 2010. The evolution of laminates in finite crystal plasticity: A variational approach. *Continuum Mech. Therm.* 23 (1), 63-85.
- Koster, M., Le, K. C., Nguyen, B. D., 2015. Formation of grain boundaries in ductile single crystals at finite plastic deformations. *Int. J. Plasticity* 69, 134-151.
- Koster, M., Le, K. C., 2015. Formation of grains and dislocation structure of geometrically necessary boundaries. *Mater. Sci. Eng. A* 643, 12-16.
- Kröner, E., 1992. Mikrostrukturmechanik. *GAMM-Mitteilungen* 15, 104-119.

- Kubin, L. P., 2013. Dislocations, Mesoscale Simulations and Plastic Flow. Oxford University Press, Oxford.
- Kuhlmann-Wilsdorf, D., 1989. Theory of plastic deformation:-properties of low energy dislocation structures. *Mater. Sci. Eng. A* 113, 1-41.
- Kuhlmann-Wilsdorf, D., Hansen, N., 1991. Geometrically necessary, incidental and subgrain boundaries. *Scr. Metall. Mater.* 25, 1557-1562.
- Kysar, J. W, Saito, Y., Oztop, M. S., Lee, D., Huh, W. T., 2010. Experimental lower bounds on geometrically necessary dislocation density. *Int. J. Plasticity* 26, 1097-1123.
- Laird, C., Charsley, P., Mughrabi, H., 1986. Low energy dislocation structures produced by cyclic deformation. *Mater. Sci. Eng.* 81, 433-450.
- Lanczos, C., 1970. The Variational Principles of Mechanics. Dover Publications Inc., New York.
- Le, K. C., Sembiring, P., 2008a. Plane constrained shear of single crystals within continuum dislocation theory. *Arch. Appl. Mech.* 78, 587-597.
- Le, K. C., Sembiring, P., 2008b. Plane-constrained shear of a single crystal strip with two active slip-systems. *J. Mech. Phys. Solids* 56, 2541-2554.
- Le, K. C., Sembiring, P., 2009. Plane constrained uniaxial extension of a single crystal strip. *Int. J. Plasticity* 25, 1950-1969.
- Le, K. C., 2010. Introduction to Mircomechanics. Nova Science Publishers, Inc., New York.
- Le, K. C., Nguyen, B. D., 2012. Polygonization: Theory and comparison with experiments. *Int. J. Eng. Sci.* 59, 211-218.
- Le, K. C., Nguyen, B. D., 2013. On bending of single crystal beam with continuously distributed dislocations. *Int. J. Plasticity* 48, 152-167.
- Le, K. C., Günther, C., 2014. Nonlinear continuum dislocation theory revisited. *Int. J. Plasticity* 53, 164-178.
- Lee, E. H., Liu, D. T., 1967. Finite strain elastic-plastic theory with application to plane-wave analysis. *J. Appl. Phys.* 38, 19-27.
- Lee, E. H., 1969. Elastic-plastic deformation at finite strains. *J. Appl. Mech.* 36, 1-6.
- Lee, J. C., Seok, H. K., Suh, J. Y., 2002. Microstructural evolutions of the Al strip prepared by cold rolling and continuous equal channel angular pressing. *Acta Mater.* 50 (16), 4005-4019.
- Lim, H., Lee, M. G., Kim, J. H., Adams, B. L., Wagoner, R. H., 2011. Simulation of polycrystal deformation with grain and grain boundary effects. *Int. J. Plasticity* 27, 1328-1354.
- Lubliner, J., 2008. Plasticity Theory. Dover Publications Inc., New York.
- MacCluer, C. R., 2005. Calculus of Variations. Mechanics, Control & Other Applications. Dover Publications Inc., New York.
- Marsden, J. E., Hughes, T. J. R., 1994. Mathematical Foundations of Elasticity. Dover Publications Inc., New York.

- Mayeur, J. R., McDowell, D. L., 2014. A comparison of Gurtin type and micropolar theories of generalized single crystal plasticity. *Int. J. Plasticity* 57, 29-51.
- Nocedal, J., Wright, S. J., 2006. *Numerical Optimization*. Springer, New York, 2nd edition.
- Oden, J. T., 2011. *An Introduction to Mathematical Modeling. A Course in Mechanics*. John Wiley & Sons Inc., Hoboken.
- Öztop, M. S., Niordson, C. F., Kysar, J. W., 2013. Length-scale effect due to periodic variation of geometrically necessary dislocation densities. *Int. J. Plasticity* 41, 189-201.
- Ogden, R. W., 1972. Large deformation isotropic elasticity: On the correlation of theory and experiment for incompressible rubber-like solids. *Proc. Royal Soc. Lond. A* 328, 567-583.
- Ogden, R. W., 1997. *Non-Linear Elastic Deformations*. Dover Publications Inc., New York.
- Orowan, E., 1934. Zur Kristallplastizität. III. Über den Mechanismus des Gleitvorganges. *Z. Phys.* 89, 634-659.
- Ortiz, M., Repetto, E. A., 1999. Nonconvex energy minimization and dislocation structures in ductile single crystals. *J. Mech. Phys. Solids* 47, 397-462.
- Ortiz, M., Repetto, E. A., Stainier, L., 2000. A theory of subgrain dislocation structures. *J. Mech. Phys. Solids* 48, 2077-2114.
- Phillips, R., 2001. *Crystals, Defects and Microstructures. Modeling Across Scales*. Cambridge University Press, Cambridge.
- Polanyi, M., 1934. Über eine Art Gitterstörung, die einen Kristall plastisch machen könnte. *Z. Phys.* 89, 660-664.
- Raoult, A., 1986. Non-polyconvexity of the stored energy function of a Saint Venant-Kirchhoff material. *Aplikace matematiky* 6, 417-419.
- Read, W. T., Shockley, W., 1950. Dislocation models of crystal grain boundaries. *Phys. Rev.* 78, 275-289.
- Reddy, J. N., 2002. *Energy principles and variational methods in applied mechanics*. John Wiley & Sons Inc., Hoboken.
- Reddy, J. N., 2004. *An Introduction to Nonlinear Finite Element Analysis*. Oxford University Press, Oxford.
- Romano, A., Lancellotta, R., Marasco, A., 2006. *Continuum Mechanics using Mathematica. Fundamentals, Applications and Scientific Computing*. Birkhäuser, Boston.
- Sakai, G., Horita, Z., Langdon, T. G., 2005. Grain refinement and superplasticity in an aluminum alloy processed by high-pressure torsion. *Mater. Sci. Eng. A* 393 (1), 344-351.
- Sedov, L. I., 1965. Mathematical methods of constructing models of continuum media. *Uspekhi Matematicheskikh Nauk* 20, 123-182.
- Segal, V. M., 1995. Material processing by simple shear. *Mater. Sci. Eng. A* 197, 157-164.

- Shima, H., Nakayama, T., 2010. Higher Mathematics for Physics and Engineering. Springer, Berlin.
- Šilhavý, M., 1997. The Mechanics and Thermodynamics of Continuous Media. Springer, Berlin.
- Simo, J. C., Hughes, T. J. R., 1998. Computational Inelasticity. Springer, New York.
- Spencer, A. J. M., 1980. Continuum Mechanics. Dover Publications Inc., New York.
- Strang, G., 2007. Computational Science and Engineering. Wellesley-Cambridge Press, Wellesley.
- Strang, G., 2009. Introduction to Linear Algebra. Wellesley-Cambridge Press, Wellesley, 4th edition.
- Tadmor, E. B., Miller, R. E., 2011. Modeling Materials. Continuum, Atomistic and Multiscale Techniques. Cambridge University Press, New York.
- Tadmor, E. B., Miller, R. E., Elliot, R. S., 2012. Continuum Mechanics and Thermodynamics. From Fundamental Concepts to Governing Equations. Cambridge University Press, New York.
- Takeuchi, T., 1975. Work hardening of copper single crystals with multiple glide orientations. Mater. Trans. 16, 629-640.
- Taylor, G. I., 1934. The mechanism of plastic deformation of crystals. Part I. Theoretical. Proc. Royal Soc. Lond. A 145, 362-387.
- Thompson, R. C., Freede, L. J., 1971. On the eigenvalues of sums of Hermitian matrices. Linear Algebra Its Appl. 4, 369-376.
- Tome, C. N., Lebensohn, R. A., Kocks, U. F., 1991. A model for texture development dominated by deformation twinning: application to zirconium alloys. Acta Metall. Mater. 39 (11), 2667-2680.
- Truesdell, C., 1978. Some challenges offered to analysis by rational thermomechanics. In: de La Penha, G. M., Medeiros, L. A. J. (eds.), Contemporary Developments in Continuum Mechanics and Partial Differential Equations, pp. 495-603, North-Holland, Amsterdam.
- Truesdell, C., Noll, W., 2004. The Non-Linear Field Theories of Mechanics. Encyclopedia of Physics, Vol. III/3, Springer, Berlin, 3rd edition.
- Uchic, M. D., Shade, P. A., Dimiduk, D. M., 2009. Plasticity of Micrometer-Scale Single Crystals in Compression. Annu. Rev. Mater. Res. 39, 361-386.
- Valiev, R. Z., Islamgaliev, R. K., Alexandrov, I. V., 2000. Bulk nanostructured materials from severe plastic deformation. Prog. Mater. Sci. 45 (2), 103-189.
- Valiev, R. Z., Langdon, T. G., 2006. Principles of equal-channel angular pressing as a processing tool for grain refinement. Prog. Mater. Sci. 51 (7), 881-981.
- van Brunt, B., 2004. The Calculus of Variations. Springer, New York.

- Vorhauer, A., Pippan, R., 2004. On the homogeneity of deformation by high pressure torsion. *Scr. Mater.* 51 (9), 921-925.
- Weertman, J., Weertman, J. R., 1992. *Elementary Dislocation Theory*. Oxford University Press, Oxford.
- Weinstock, R., 1974. *Calculus of Variations. With Applications to Physics & Engineering*. Dover Publications Inc., New York.
- Wriggers, P., 2001. *Nichtlineare Finite-Element-Methoden*. Springer-Verlag, Berlin.
- Xiao, H., Bruhns, I. O., Meyers, I. A., 1997. Logarithmic strain, logarithmic spin and logarithmic rate. *Acta Mech.* 124, 89-105.
- Zhu, X., Dai, S., Xiang, Y., 2013. Numerical simulation of dynamics of dislocation arrays and long-range stress fields of nonplanar dislocation arrays. *Int. J. Plasticity* 43, 85-100.
- Zhu, X., Xiang, Y., 2014. Continuum framework for dislocation structure, energy and dynamics of dislocation arrays and low angle grain boundaries. *J. Mech. Phys. Solids* 69, 175-194.

Curriculum Vitae**Personal Data**

Name	Michael Koster
Date of Birth	December 12, 1979
Place of Birth	Iserlohn
Nationality	German
Marital Status	single

School Education

08/1990-06/1999	Märkisches Gymnasium Iserlohn, Abitur in June 1999
08/1986-06/1990	Grundschule Lichte Kammer, Iserlohn

University Education

10/2006-12/2011	Mechanical Engineering, Ruhr-Universität Bochum, Germany, Dipl.-Ing. Degree in December 2011
09/2001-08/2005	Industrial Engineering, Fachhochschule Südwestfalen, Hagen, Germany, Dipl.-Wirt.Ing. (FH) Degree in August 2005

Professional Occupation

01/2014-12/2017	Research associate, Lehrstuhl für Mechanik - Materialtheorie Ruhr-Universität Bochum, Germany
01/2012-12/2013	Research associate, Lehrstuhl für Statik und Dynamik Ruhr-Universität Bochum, Germany

**Mitteilungen aus dem Institut für Mechanik
RUHR-UNIVERSITÄT BOCHUM
Nr. 178**

ISBN 978-3-935892-56-8